An Experimental Study of Foam Flow in Water Saturated Porous Media

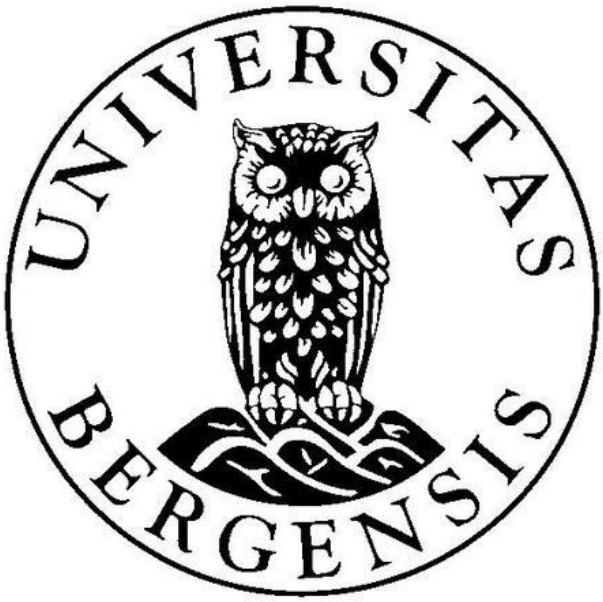

Master Thesis in Petroleum Technology – Reservoir Physics

Christina Berge

Department of Physics and Technology

University of Bergen

June 2017

ABSTRACT

The amount of greenhouse gases in the atmosphere has increased significantly the last 250 years, causing a global temperature rise. CO_2 emissions from fossil fuel combustion is a major contributor to greenhouse gas emissions, and carbon capture and sequestration (CCS) has been suggested and to some extent implemented as a mitigation method. This experimental work presents a study of the use of foam in a CO_2 storage context. The investigation is part of an on-going project with field pilots in Texas, where the objective is to implement mobility control with CO_2 foam for storage and enhanced oil recovery on the Norwegian Continental Shelf (NCS). Foam experiments were conducted in 100% brine saturated sandstone core samples and fractured marble core samples, through co-injection of gas and surfactant solution at low pressure. Foam was pre-generated in a foam generator upon entering the core samples.

Quantitative analyses of endpoint water saturations and pressure gradients were conducted, to evaluate the foam flow behavior and displacement improvement compared to pure gas injections. Generated fractures in impermeable marble cores provided a permeability ranging from 1.47 D to 8.03 D. The fractured core samples appeared to be of such a small scale that there was little or no improvement in water production during foam injections compared to pure gas injections. Magnetic resonance imaging (MRI) was conducted for qualitative studies of water saturations, and indicated good sweep efficiency during co-injection of gas and surfactant solution in a marble core with a multi-fracture system.

Calculated mobility reduction factors for foam experiments in unfractured Bentheimer sandstone cores indicated an average gas mobility reduction of 3.94, compared to pure gas injections. Resistivity measurements conducted during pure CO_2 injections and co-injections of CO_2 gas and surfactant solution in sandstone cores were used to calculate water saturations using Archie's law. Archie's law is developed for use in an oil-water system, and does not consider the conductivity of the liquid phase in foam displacements. A modification is therefore needed for Archie's law to be applicable in foam-water systems.

ACKNOWLEDGEMENTS

First of all, I would like to thank my supervisor Associate Professor Geir Ersland, at the Department of Physics and Technology, University of Bergen. Thank you for good advice and encouragement through your positive attitude. I would also like to thank Associate Professor Martin Fernø and Professor Arne Graue. I appreciate the opportunity to work on interesting research subjects.

Thanks to Dr. Marianne Steinsbø and PhD candidate Stian Almenningen for excellent guidance on experimental work. I really appreciate your help and good patience. I would also like to thank fellow master student Andreas G. Polden for lab assistance and advice – you always have an optimistic mind and clever solutions. Thanks to the staff at the mechanical workshop for providing equipment for the experimental work.

A special thanks to my lab partner and good friend, Solveig Carlsen. It has meant a lot to have someone to share long hours at the lab with. Thank you for inspiration, motivation and support, and your good sense of humor! It has been a pleasure working with you. Thanks also to all other fellow students at the University of Bergen for good times and encouragement, and especially Ida Vikingstad for a lot of fun and adventures during the last five years.

Finally, I would like to give a huge thanks to my family and friends, for your endless support.

Bergen, June 2017

Christina Berge

TABLE OF CONTENTS

Abstract iii
Acknowledgements iv
Introduction ix
Part I – Theory 1
1 Fundamentals in Carbon Capture Sequestration 3
1.1 Physical Properties of CO_2 3
1.2 CO_2 Capture 3
1.3 CO_2 Transport 4
1.4 CO_2 Storage 5
1.4.1 CO_2 migration 5
1.4.2 CO_2 trapping mechanisms 6
1.5 CO_2 Storage Capacity and Efficiency in Saline Aquifers 7
1.6 Displacement Instability 8
2 Foam 11
2.1 Definition of Foam 11
2.2 Mechanisms of Foam Generation 12
2.3 Foam Flow Behavior 14
2.4 Foam Stability and Decay 15
2.5 Surfactant as Foaming Agent 16
3 Reservoir Physics in CO_2 Storage Schemes 17
3.1 Fractured Reservoirs 17
3.2 CO_2 Propagation in Fractured Geological Media 18
3.3 Displacement Efficiency 19
4 Literature Survey 21
4.1 Foam Behavior in Porous Media 21
4.2 Foam Behavior in Fractures 22
Part II – Experimental Procedures 25
5 Experimental Objective 27

6 Fluids and Core Materials 29
6.1 Fluids 29
6.2 Core Material 30
6.3 Core Preparations 30
6.3.1 Fractured marble cores 30
6.3.2 Sandstone cores 33
7 Experimental Set-up and Procedures 35
7.1 Routine Core Analysis 35
7.1.1 Porosity and permeability measurements in fractured marble cores 35
7.1.2 Porosity and permeability measurements in sandstone cores 36
7.2 Experimental Procedures in Fractured Marble Cores 38
7.2.1 N_2 gas injection in fractured marble cores at low pressure 39
7.2.2 N_2 foam injections in fractured marble cores at low pressure 40
7.3 Experimental Procedures in Bentheimer Sandstone Cores 44
7.3.1 CO_2 gas injection in sandstone cores at low pressure 44
7.3.2 CO_2 foam injection in sandstone cores at low pressure 46
7.3.3 Resistivity measurements 47
7.4 Magnetic Resonance Imaging 48
7.4.1 Principles of Magnetic Resonance Imaging 48
7.4.2 Imaging foam propagation in fractured networks 50
Part III – Results and Discussion 53
8 Fractured Marble Cores 55
8.1 N_2 Gas Injection in Fractured Marble Cores 56
8.2 Foam Injections in Fractured Marble Cores 59
8.2.1 Multi-Fracture System in Core M2i-1 60
8.2.2 Simple Multi-Fracture System in Core M2i-2 61
8.2.3 Single-Fracture System in Core M2i-3 63
8.2.4 The Effect of Foam on Displacement Efficiency in Fractured Marble Cores ... 64

8.3 Magnetic Resonance Imaging of Foam Flow in Fractures 66
8.3.1 MRI of Fractured Marble Cores 66
8.4 Dynamic MRI of Fractured Marble Core M2i-1 68
9 Bentheimer Sandstone Cores 69
9.1 CO_2 Gas Injections in Bentheimer Sandstone Cores 69
9.2 Foam Flow Behavior in Bentheimer Sandstone Cores 71
9.3 The Effect of Foam on Mobility Reduction 74
9.4 Validity of Archie's Law in Foam-Water Systems 75
10 Experimental Uncertainties 78
Part IV – Conclusions and Future Work 81
11 Conclusions 83
12 Future Work 84
Nomenclature 85
Abbreviations 87
Appendix A – Fundamental Properties in Reservoir Engineering 88
Appendix B – Uncertainty Estimations 90
Appendix C – The Effect of NaCl brine on Marble Rocks 92
Appendix D – Estimation of Dead Volumes 93
Appendix E – Calculations of Offset between ESI Pressure Transducers 96
Appendix F – An Overview of Experiments 97
References 99

INTRODUCTION

Since the industrial revolution in 1750, there has been a significant temperature increase on the planet (Bachu, 2015). Between 1880 and 2012 the average land and ocean surface temperature increased with 0.85°C (IPCC, 2014). The warming is most probably linked to an increased amount of greenhouse gases in the atmosphere, including carbon dioxide, methane, and nitrous oxide. Burning of fossil fuels, industrial processes and transportation are main contributors to emissions of CO_2 (Bachu, 2015, Huaman and Jun, 2014). According to the IPCC (2014), CO_2 emissions from fossil fuels and industrial processes amounted 78% of greenhouse gas emissions between 1970 and 2010. Since 1990 there have been a rapid growth in the world population and in the amount of industrialized countries, which have led to a higher global energy demand, and in turn resulted in higher CO_2 emissions (Yang et al., 2008).

Greenhouse gas mitigation is regarded as necessary to stabilize emissions and prevent serious damage to the world's ecosystems. One method to reduce emissions of CO_2 is underground storage. Carbon capture sequestration (CCS) refers to the capturing of CO_2 produced from large point sources before entering the atmosphere, transporting the CO_2 to a storage site, and storing it underground in geologic formations (Bachu, 2015). This can be significant in keeping the amount of CO_2 emissions at a sustainable level, while simultaneously meeting the increasing global energy demand. A pioneer in CCS is Statoil, which in 1996 started the first commercial storage project in geological media, at the Sleipner field in the North Sea, where 1 million tons CO_2 is stored annually (Torp and Gale, 2004). In 2016, the Global CCS Institute (2016) identified 15 large-scale CCS projects in operation, and 23 more in development around the world.

In most storage projects, CO_2 is stored in the supercritical phase, and is far more mobile than water and oil (Benson and Cole, 2008, IPCC, 2005). This leads to displacement instabilities and low sweep when CO_2 is injected in the storage formations. In the petroleum industry, a well-known mobility control technique is the injection of foam (Sheng, 2013). There is good reason to believe that this could be adapted to a CO_2 storage scheme, to increase the sweep and displacement efficiency during CO_2 injection and thus increase the amount of stored CO_2. Foam is especially functional in fractured media, where displacements are often unstable due to high transferability in fractures (Haugen et al., 2014).

Part I – Theory

1 FUNDAMENTALS IN CARBON CAPTURE SEQUESTRATION

1.1 PHYSICAL PROPERTIES OF CO_2

For sequestration of CO_2 it is important to know how CO_2 behaves under different conditions. The phase diagram of pure CO_2 is presented in Figure 1. At standard conditions CO_2 is in gas phase, but an isothermal increase of pressure to above the saturation pressure causes a phase transition into the liquid state. If temperature and pressure exceed the critical conditions at 31°C and 73.8 bar, the CO_2 exists in a supercritical phase. In the supercritical state, it is not possible to distinguish between gas and liquid properties, and the CO_2 behaves like a gas with the density of a liquid. The triple point of CO_2, where gas, liquid and solid phase meet, is at -56.6°C and 5.1 bar.

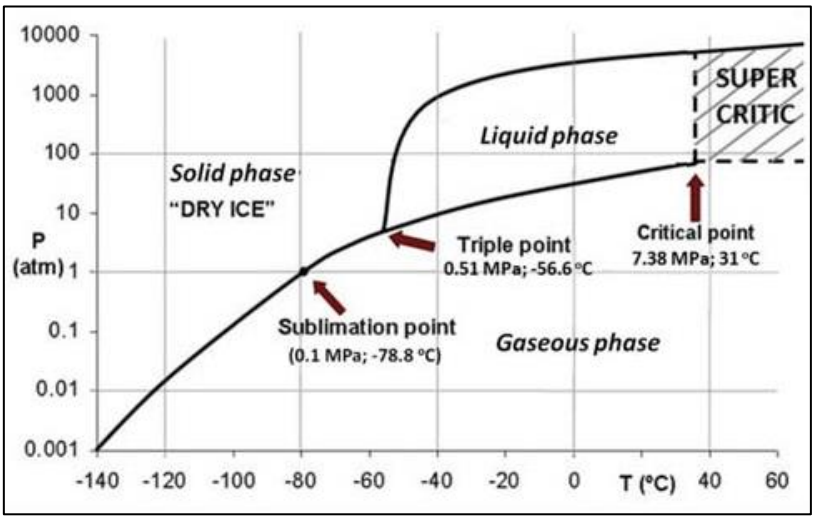

Figure 1 – Phase envelope for CO2, with critical point at 31°C and 73.8 bar. (Mazzoldi et al., 2013)

1.2 CO_2 CAPTURE

Combustion of fossil fuels produces gas streams containing various amounts of CO_2. There are three main processes used to capture the CO_2: pre-combustion capture, post-combustion capture and oxy-combustion capture (Figueroa et al., 2008, Yang et al., 2008). All methods are illustrated in Figure 2. In pre-combustion capture the CO_2 is captured before combustion. The fossil fuel is reacted with oxygen in a gasification process, forming a synthesis gas consisting of hydrogen, carbon monoxide and CO_2. Steam is added to the synthesis gas in a reactor and a water gas shift reaction converts the carbon monoxide and water into a mixture of CO_2 and

hydrogen. The resulting gas mixture typically contains 15-60% CO_2, which can be removed through separation techniques (IPCC, 2005).

Post- and oxy-combustion capture requires burning of the fossil fuels. In post-combustion capture, fossil fuels are combusted in air, producing steam and a flue gas consisting of nitrogen, water vapor and typically less than 15% CO_2 (Figueroa et al., 2008). The same procedure follows for oxy-fuel-combustion, but in this case the fuel is burnt in nearly pure oxygen instead of air. This creates a flue gas of mainly CO_2 and water vapor, with CO_2 concentrations greater than 80% (IPCC, 2005). Condensation removes the water and the CO_2 is purified before storage.

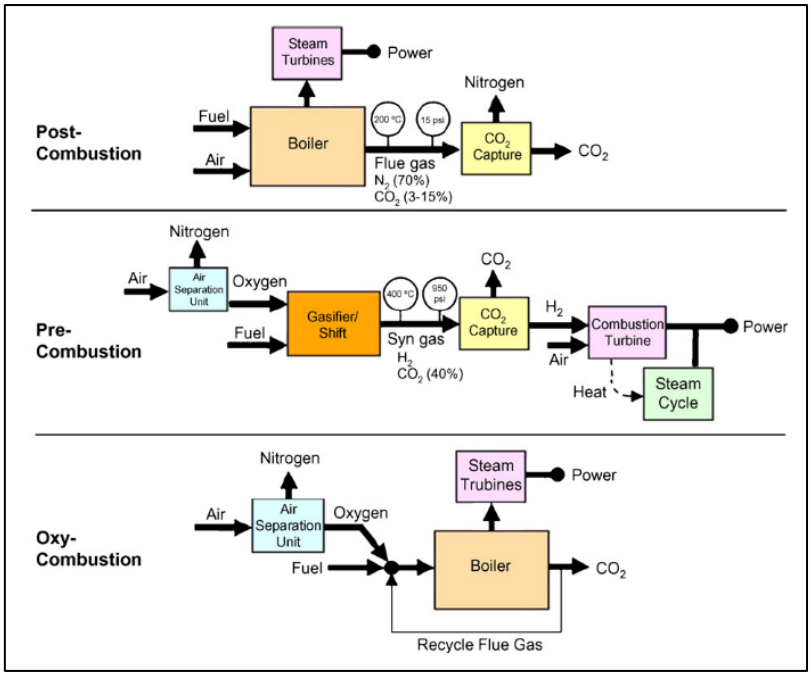

Figure 2 – Illustration of the three main processes of CO2 capture (Figueroa et al., 2008)

After a capturing method has been applied, the CO_2 can be removed from the resulting gas streams with different separation techniques. Common techniques are the use of amine absorbents, adsorbents, membranes, or cryogenic distillation (Kheshgi et al., 2006, Yang et al., 2008, IPCC, 2005).

1.3 CO_2 TRANSPORT

Captured CO_2 is compressed and dehydrated before it can be transported to an appropriate storage site. Pipelines are the preferred transportation method, and can transport large amounts

of CO_2 both onshore and offshore (IPCC, 2005). CO_2 can be transported in solid, liquid, gas, or supercritical phase. In pipelines, CO_2 is normally transported in gas or supercritical phase and is compressed to a pressure above 80 bar to increase density and secure single-phase flow (IPCC, 2005). It is common to have a compressor at the pipeline entrance that drives the flow, but some pipelines have transitional compressor stations to boost the flow.

For smaller amounts of CO_2, or larger offshore distances of typically 1000 km or more, transportation by ships may be preferred. CO_2 in liquid state, at a pressure of typically 7 bar, is most convenient when transporting CO_2 by ship (Seevam et al., 2007). It is also possible to transport CO_2 by railroad or road tankers, but this is only relevant on a small-scale.

1.4 CO_2 STORAGE

When the CO_2 has been transported to a selected storage site, the fluid is injected underground into geological formations. Different geological media has been considered appropriate for CO_2 storage: primarily oil and gas reservoirs, saline aquifers and coal beds, but also basalt, organic-rich shale and salt caverns (IPCC, 2005). Only oil and gas reservoirs and saline aquifers have successfully been used for storage so far (Bachu, 2015). Suitable formations are large and deep accumulations of porous and permeable sediments, with simple formation structures and thick, impermeable rock layers acting as seals (IPCC, 2005, Benson and Cole, 2008). CO_2 is preferably stored at depths of at least 800 m, where the density is high and the CO_2 exists in a supercritical phase (Benson and Cole, 2008, Bentham and Kirby, 2005).

1.4.1 CO_2 migration

When CO_2 is injected into a formation it displaces the fluids initially present in the pore space or fractures of the formation. Saline aquifers are initially saturated with brine, whereas oil and gas reservoirs are usually filled with both hydrocarbons and brine. Fluid flow depends on the present fluid phases and their miscibility, as it affects the relative permeabilities and flow rates. CO_2 is immiscible with formation water, and the fluids exist in separate phases. The miscibility of oil and CO_2 depends on the composition of the oil and the pressure and temperature conditions in the reservoir. CO_2 and natural gas are miscible fluids (IPCC, 2005, Benson and Cole, 2008). In miscible displacement processes the CO_2 displaces most of the initial fluids in the formation. If the fluids are immiscible, the storage capacity is limited by flow dynamics and capillary pressure between the fluid phases. The resulting CO_2 saturation is often lower than 30% (Benson and Cole, 2008).

During injection, the flow of CO_2 is affected by the pressure gradient that forms due to pressure buildup near the injection well. The pressure gradient depends on injection rate, formation characteristics, and the geometry of the groundwater system. After injection has stopped, or far from the well, the CO_2 flow is mainly driven by buoyancy forces due to density differences, causing migration upwards (Oldenburg, 2007). Distribution of CO_2 is also controlled by formation heterogeneity, mobility differences between the fluids, natural hydraulic gradients, and natural processes of diffusion, mineralization, adsorption and dissolution (IPCC, 2005).

1.4.2 CO_2 trapping mechanisms

Different mechanisms can trap CO_2 underground. Physical trapping mechanisms include structural and stratigraphic trapping below an impermeable cap rock. Folds and fractures can form structural traps, while stratigraphic traps are created by changes in lithology. When CO_2 migrate upwards because of buoyancy forces, it continues to flow until encountering a sealing formation where structural or stratigraphic traps prevent the CO_2 from flowing further (IPCC, 2005).

CO_2 can also be trapped by capillary forces as residual saturation. This happens after injection has stopped, because formation water, as the wetting fluid, imbibes back to the pore space occupied by CO_2, and immobilizes and traps the CO_2 (Zhang and Song, 2014).

Other trapping mechanisms occur when CO_2 interacts chemically with the formation water or rock. CO_2 dissolving in formation water is called solubility trapping (Zhang and Song, 2014). When CO_2 has been dissolved, buoyancy forces do not drive the CO_2 upwards, since it is no longer a separate phase. The dissolved CO_2 will continue to flow with the groundwater which has a velocity of 1-10 cm/year, and may not reach the surface in a million years (Bachu et al., 1994).

Dissolved CO_2 reduces the pH of the formation water, allowing yet another trapping mechanism to occur. In the longer term the reduced pH enables reactions between the CO_2 and the minerals in the rock matrix, forming carbonate minerals (Han et al., 2010). This is called mineral trapping. An overview of CO_2 trapping mechanisms is shown in Figure 3.

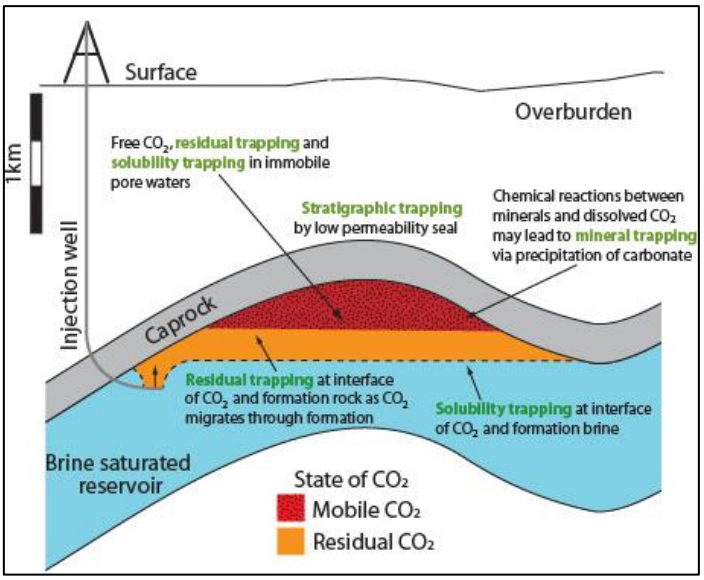

Figure 3 – Illustration of CO2 trapping mechanisms in a saline aquifer. (UK CCS Research Centre, 2012)

1.5 CO_2 Storage Capacity and Efficiency in Saline Aquifers

CO_2 storage capacity of a saline aquifer describes the amount of CO_2 that can be stored in the aquifer, while storage efficiency relates the amount of stored CO_2 to the size of the aquifer. The concept of CO_2 storage efficiency, E, was first introduced in 2007, and is defined as the volume of injected CO_2 in a saline aquifer, V_{CO2} [ml], relative to the pore volume of the aquifer, V_p [ml] (Bachu, 2015). On pore scale the storage efficiency can be expressed in terms of water saturation, S_w:

$$E = \frac{V_{CO_2}}{V_p} = 1 - S_w \quad (1)$$

Irreducible water saturation represents the highest storage efficiency.

Storage efficiency depends on several factors, including characteristics of the storage aquifer, characteristics of the confining formation rocks, characteristics of the CO_2 injection procedure, and regulatory constraints (Bachu, 2015). The capillary entry pressure of the confining aquitards is especially important, because these can either allow flow of CO_2, or have a capillary entry pressure that is too high for CO_2 flow. A closed or semi-closed aquifer does not allow CO_2 flow, but may allow pressure dissipation and brine leakage, and in turn increase the storage capacity and efficiency. An open aquifer is vertically confined, but not horizontally, and the

CO_2 can be distributed across a large area (Bentham and Kirby, 2005). This is illustrated in Figure 4.

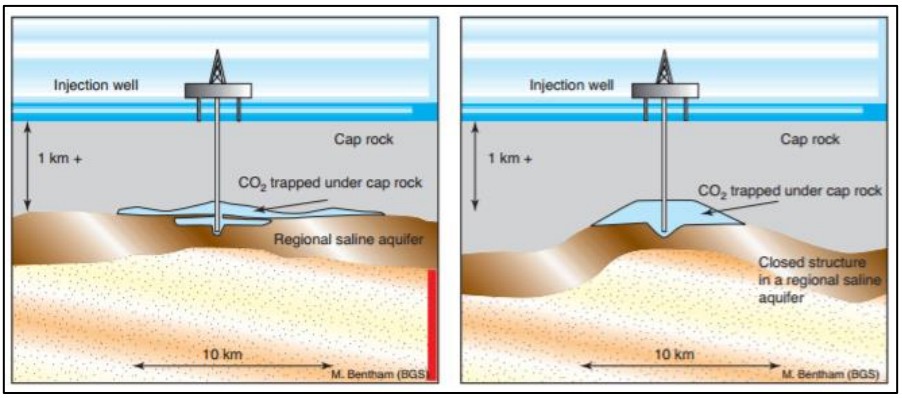

Figure 4 Illustration of an open aquifer to the left and a closed aquifer to the right. (Bentham and Kirby, 2005)

Storage capacity of the Utsira formation in the North Sea has been investigated in a study performed by Lindeberg et al. (2009). The formation is one of the major aquifers with potential of long-term CO_2 sequestration, and is already used for storage in the Sleipner field. The investigations included both static volume estimates and reservoir simulation, and indicated a cost-effective CO_2 storage capacity between 20 to 60 Gt. It was also found that the CO_2 could most likely be stored safely from a depth of approximately 500 m.

1.6 DISPLACEMENT INSTABILITY

CO_2 is normally stored in the supercritical phase, which has a lower viscosity and density than water and oil (Benson and Cole, 2008, IPCC, 2005). This affects the mobility ratio between the fluids. The mobility of a fluid, λ [m^2/Pa·s], is defined as the ratio between the effective permeability of the rock, K_e [m^2], and the viscosity of the fluid, μ [Pa·s] (Lien, 2004):

$$\lambda = \frac{K_e}{\mu} = \frac{Kk_r}{\mu} \tag{2}$$

where K [m^2] is the absolute permeability of the rock and k_r is the relative permeability of the fluid. The mobility ratio, M, between two fluids is an important parameter in fluid displacements, and is defined as the mobility of the displacing fluid (in this case CO_2), λ_{CO2} [m^2/Pa·s], divided by the mobility of the displaced fluid (in this case water, oil or gas), λ_x [m^2/Pa·s], (Lien, 2004):

$$M = \frac{\lambda_{CO2}}{\lambda_x} \tag{3}$$

An unfavorable mobility ratio leads to poor sweep and displacement efficiency. When the mobility of CO_2 is higher than the mobility of the displaced fluid because of the low CO_2 viscosity, the CO_2 will flow in high-permeable zones, leaving low-permeable zones unswept (Enick et al., 2012, Espinoza et al., 2010). This is called viscous fingering. The displacement will be unstable, causing early CO_2 breakthrough and poor water or oil displacement. Because of the high permeability in fractured reservoirs compared to unfractured reservoirs, the effect is especially prominent in these (Kovscek et al., 1995). The high CO_2 mobility also enhances the risk of leakage, as the CO_2 can migrate upwards through the cap rock or in the formation close to the injection well (Batôt et al., 2016).

A more favorable mobility ratio will allow storage of more CO_2 in the formation, and can be achieved by implementing mobility control to reduce the mobility ratio. Mobility control is achieved by reducing the mobility of the displacing fluid by changing the relative permeability or viscosity of the fluid (Enick et al., 2012). One mobility control technique is to inject CO_2 as a *foam*. This will increase the mobility of the CO_2 and thus lower the mobility ratio. A more detailed description of foam is presented in section 2. If CO_2 is injected into a natural gas reservoir the CO_2 is more viscous than the gas, causing a more stable displacement than in a brine- or oil filled formation (Oldenburg et al., 2001).

Density differences between CO_2 and the displaced fluid also causes instable displacements, in the form of gravity override. Buoyancy forces drive CO_2 upwards, prohibiting storage in the lower parts of the formations. This phenomenon is especially present in saline aquifers, where the density differences between the formation water and CO_2 are large, up to 50% (IPCC, 2005). In oil reservoirs, the gravity segregation effect depends on the miscibility of the CO_2 and oil. Natural gas is less dense than CO_2, causing CO_2 migration below the gas in the reservoir (Oldenburg et al., 2001). The density of CO_2 is a function of temperature and pressure, which are difficult factors to control. Hence, gravity segregation is also reduced through mobility control, for example by lowering the mobility of the displacing fluid through CO_2 foam injection (Enick et al., 2012). It is also possible to use gels for conformance control, as gels can block high-permeable zones and divert the fluid flow to zones with lower permeability (Enick et al., 2012).

Variations of CO_2 density and viscosity with depth are shown in Figure 5, for temperature gradients of 15°C/km and 30°C/km.

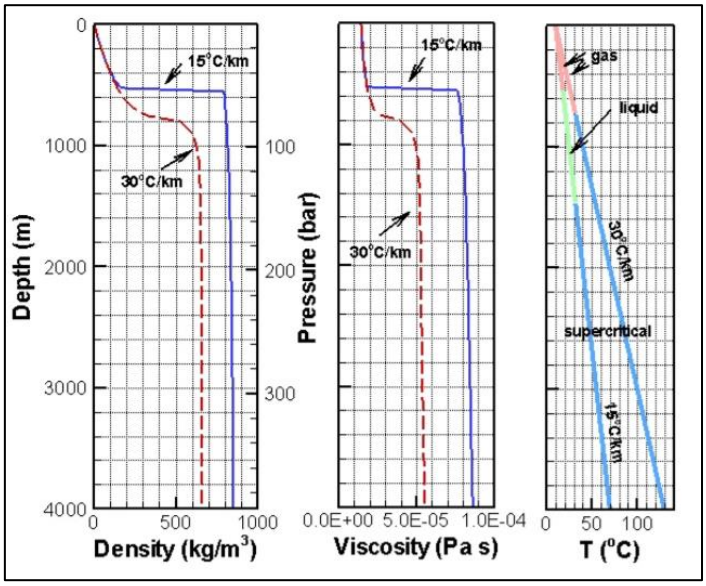

Figure 5 – Density, viscosity and temperature variations with depth and pressure for CO_2. Two different geothermal gradients are presented, 15°C/km and 30°C/km. At the temperature profile to the right, phase changes are indicated, where red represents gas, green represents liquid and blue represents supercritical phase. (Oldenburg, 2007)

2 FOAM

Injection of CO_2 into an oil- or brine filled formation gives an unfavorable mobility ratio due to viscosity and density differences, possibly leading to viscous fingering and gravity override. Increased mobility control can be achieved by injection of foam, which has a lower mobility than pure CO_2 (Kam and Rossen, 2003, Ransohoff and Radke, 1988).

2.1 DEFINITION OF FOAM

According to Schramm (2006) "a foam is a colloidal dispersion in which a gas is dispersed in a continuous liquid phase". The gas can be either continuous or discontinuous. Figure 6 shows a foam system, where thin liquid films separate polyhedral bubbles of gas. The liquid film and the interfaces between the liquid and the gas constitute a lamella. The region where three lamellae connect is called a Plateau border (Schramm, 2006, Sheng, 2013).

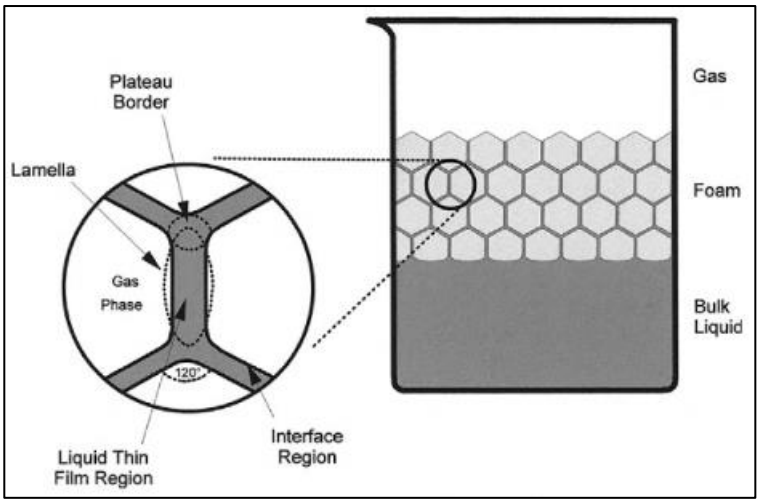

Figure 6 – A two-dimensional foam system, in which a foam structure is surrounded by gas on the top and liquid on the bottom. (Schramm, 2006)

In general, the liquid phase in a foam system is water. However, in some foams the liquid phase could be composed of acids or hydrocarbon fluids (Sheng, 2013). In addition to the gas and liquid dispersion, foams can also contain oil droplets or solid particles. In order to create a stable foam that does not break after a short while, a foaming agent, such as surfactants, must be present at the interface between the liquid and the gas (Sheng, 2013). The foaming agent reduces interfacial tension and stabilizes the liquid films, preventing coalescence of gas bubbles.

Foams are characterized by bubble size and foam quality. If the bubble diameters are much smaller than the diameter of the confining pore space or fracture, the foam is referred to as a

bulk foam (Kovscek et al., 1995). A foam with bubble diameters equal to or larger than the diameter of the pore space or fracture, is classified as a confined foam (Wassmuth et al., 2001). Foams that contain thick liquid layers separating spherical gas bubbles are called wet foams, or kugelschaum (Sheng, 2013). In persistent foams the gas bubbles have become polyhedral and are separated by thin liquid films. These are called dry foams, or polyederschaum (Schramm, 2006). The foam quality is defined as the gas fractional flow, which is the ratio between the gas flow rate and the total flow rate (Batôt et al., 2016). High foam quality results in a dry foam, while low foam quality results in more spherical gas bubbles and thicker liquid films.

2.2 MECHANISMS OF FOAM GENERATION

Foam can be generated if a liquid containing a foaming agent is mixed with a gas phase (Sheng, 2013). Foam generation during injection is achieved by surfactant-alternating-gas injection or co-injection of gas and surfactant solution (or another foaming agent). The main mechanisms for foam generation in presumably all types of porous media are gas bubble snap-off, lamella leave-behind and lamella division (Ransohoff and Radke, 1988).

Snap-off occurs when gas bubbles flow from a low-permeability zone into a high-permeability zone, which happens when gas displaces liquid from a pore throat. The capillary pressure decreases as the non-wetting gas phase expands after the narrow throat. This creates a pressure gradient in the wetting liquid phase, which enables the liquid to flow back from the surrounding pore space into the constriction in the pore throat. If the capillary pressure decreases below a certain value, a gas bubble will be snapped off by the liquid, as illustrated to the right in Figure 7 (Ransohoff and Radke, 1988).

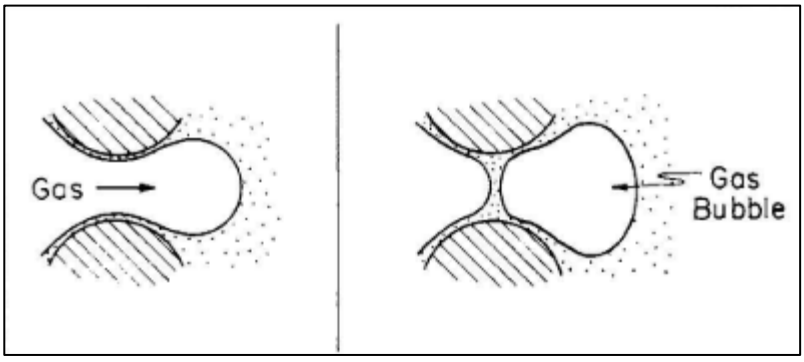

Figure 7 – Foam generation by the gas bubble snap-off mechanism. (Ransohoff and Radke, 1988)

Snap-off can occur several times at the same location in the pore space. It also increases discontinuity in the gas phase by generating separate gas bubbles. The resistance to flow of

discontinuous gas is larger than the resistance to flow of continuous gas. The separate gas bubbles may also hinder gas flow by blocking pathways. Foam generated by the snap-off mechanism is considered a strong foam (Ransohoff and Radke, 1988).

Below a certain fluid velocity, lamella leave-behind is the most common foam generation mechanism (Sheng, 2013). Leave-behind happens when a pore space filled with liquid is invaded by gas from different sides, not necessarily at the same time. The gas creates pressure on the liquid and creates a lamella, that is trapped and left behind as the flow continues. The lamella may be stable if the liquid contains enough surfactant. If lamella leave-behind happens frequently the lamellae will block gas flow paths and form dead-end channels, hence reducing the gas relative permeability. Foam generated by the leave-behind mechanism is considered weak (Enick et al., 2012, Ransohoff and Radke, 1988). The leave-behind mechanism is illustrated in Figure 8.

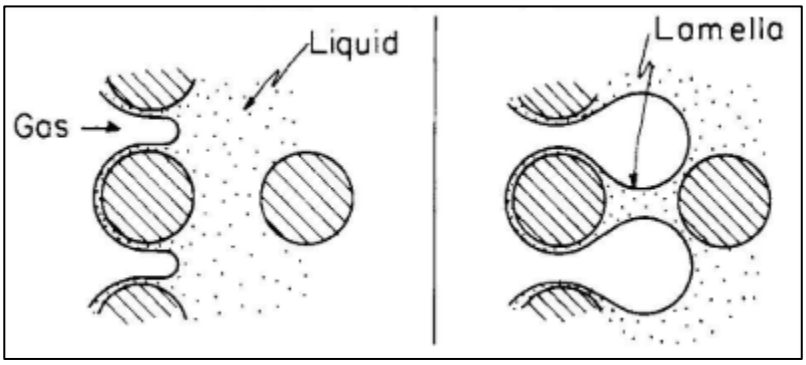

Figure 8 – Foam generation by the lamella leave-behind mechanism. (Ransohoff and Radke, 1988)

Unlike the snap-off mechanism, leave-behind does not disturb a continuous gas phase by creating separate gas bubbles. If the generated lamella start to flow out of the pore space or if the lamella breaks, it is not possible to create a new lamella by leave-behind in the same location, unless the pore-space is filled with new liquid (Ransohoff and Radke, 1988).

Lamella division can only occur if a flowing lamella already exists in the porous media. When foam approaches a branch point, as illustrated in Figure 9, the flow can either enter only one of the pore channels without generating more foam, or the flow can divide into different channels and thereby creating new lamellae. This mechanism forms a separate gas bubble, which can either flow or block certain pathways. Lamella division can happen several times in the same location (Sheng, 2013). As for the snap-off mechanism, the generated foam by lamella division is a strong foam (Ransohoff and Radke, 1988).

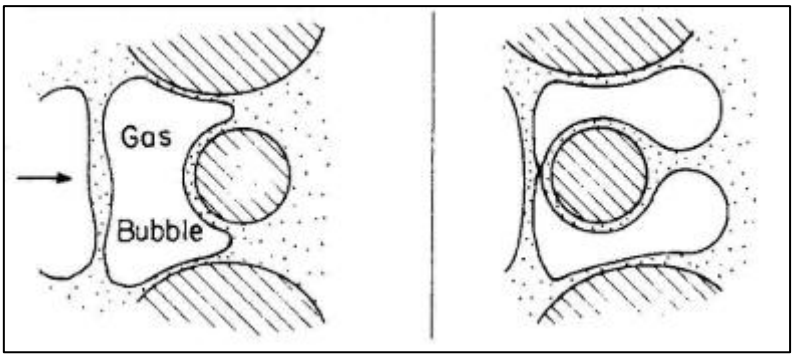

Figure 9 – Foam generation by the lamella division mechanism. (Ransohoff and Radke, 1988)

Ransohoff and Radke (1988) investigated foam generation in homogeneous glass bead packs and found that snap-off and lamella division are the dominant foam generation mechanisms above a critical capillary number. An experimental study performed by Fernø et al. (2016) showed that in a fracture network foam is consistently generated by snap-off.

2.3 FOAM FLOW BEHAVIOR

Formation of lamellae increase the apparent viscosity of foam, which results in reduced mobility (Blaker et al., 1999). The apparent viscosity depends on surfactant type and concentration, foam quality, flow rate and rock permeability. Higher permeability results in higher apparent viscosity (Lee et al., 1991). As a result, foam reduces the gas mobility more in regions with high permeability than in regions with low permeability (Skarestad and Skauge, 2013).

In foam injections with constant injection rates and a specific gas volume fraction, one can usually observe a severe pressure increase once foam is generated, due to the sudden decrease in gas mobility (Kam and Rossen, 2003). In a porous medium or a fracture, the ratio between the differential pressure during injection of foam and the differential pressure during injection of a single gas phase, constitutes the mobility reduction factor, MRF (Buchgraber et al., 2012, Kovscek et al., 1995).

$$MRF = \frac{\Delta P_f}{\Delta P_g} \tag{4}$$

where ΔP_f is the differential pressure across the porous medium or fracture during foam injection, and ΔP_g is the differential pressure during pure gas injection.

2.4 Foam Stability and Decay

All foams will eventually break as foam is not thermodynamically stable (Sheng, 2013). In an effective foam the rate of lamella destruction should not exceed the rate of lamella generation. Lamella generation is affected by pore geometry, wettability, and injection rate, while lamella decay also depends on the foaming agent (Enick et al., 2012). The stability of a foam is influenced by the volume of surfactant solution relative to gas, and the type and concentration of surfactant in the solution. The latter influences both the liquid drainage rate and liquid film strength in a foam. Low surfactant concentration gives a high liquid drainage rate and early coalescence of gas bubbles.

Foam stability also depends on pressure and temperature conditions. Increased pressure stabilizes foam, while increased temperature destabilizes foam (Sheng, 2013). Increased pressure leads to smaller bubbles and larger and thinner lamellae, and this slows down the liquid drainage rate. On the other hand, the bubbles may rupture if the pressure is too high. Temperature affects the solubility of surfactants. If the temperature increases, the solubility of surfactants in the liquid increases, and this reduces the amount of surfactant stabilizing the interface between liquid and gas. Higher temperature may also increase the liquid drainage rate.

The size of foam bubbles varies between diameters of 10-1000 μm or more (Schramm, 2006). A foam with relatively uniform bubble size distribution is more stable than a foam with less uniform bubble size distribution. The pressure in large gas bubbles are lower than the pressure in small gas bubbles, and because of this, gas diffuses through the liquid from smaller to larger bubbles, causing bubble coalescence (Sheng, 2013).

There are other factors influencing foam stability as well, including gravity and dispersed particles. Gravity effects cause liquid drainage, and in turn coalescence of gas bubbles. Dissolved species, solids or another liquid phase can influence the stability of the foam both negatively and positively (Sheng, 2013).

Lamellae can be destroyed by different mechanisms: capillary suction coalescence of gas bubbles, gas diffusion, influence of additional phases, and evaporation of liquid or condensation of gas (Nguyen et al., 2000). The most common mechanism is capillary suction coalescence (Kovscek and Radke, 1993, Nguyen et al., 2000). If the capillary pressure increases above a critical value the foam becomes unstable and will eventually rupture (Sheng, 2013).

2.5 SURFACTANT AS FOAMING AGENT

Foaming agents are necessary both to generate and stabilize foams. Surfactants are the most commonly used foaming agents, and have also been used in the experiments presented in this thesis. When a surfactant solution comes in contact with a gas phase, the surfactants are adsorbed at the interface between the fluids, and reduce the interfacial tension between the fluid phases. The adsorption of surfactant stabilizes the lamella by preventing gas bubble coalescence (Walstra, 1989).

According to Sheng (2013), several factors should be considered when selecting surfactants as foaming agents. The ability of foaming and maintaining a stable foam are important, in addition to reducing the interfacial tension between the liquid and gas. The surfactant must also be stable at high temperatures, be compatible with the fluids in the formation, and should not be highly affected by salinity changes, ions and dispersed oil particles.

Surfactant retention causes a significant decrease in the surfactant concentration in a solution. It occurs by four different mechanisms: adsorption, precipitation, ion exchange and phase trapping (Skarestad and Skauge, 2013). Surfactant retention is higher in water with high salinity and hardness.

3 RESERVOIR PHYSICS IN CO_2 STORAGE SCHEMES

The comprehensive experience from petroleum production have shown that smart use of reservoir characterization and monitoring technology, together with progressive well solutions, enhance oil recovery. This can be applied in CO_2 storage as well, where detailed characterization, monitoring and advanced well solutions can increase storage capacity (Eiken et al., 2011). Storage site characterization is important in both fractured and conventional reservoirs, but fracture systems are more complex and difficult to evaluate. Most carbonate reservoirs are fractured, and carbonate reservoirs constitute approximately 60% of the world's remaining oil reserves (Al-Maqbali et al., 2015). Understanding of fractured reservoirs is therefore significant in oil production, but also highly important in a CO_2 storage context.

3.1 FRACTURED RESERVOIRS

A reservoir fracture is a planar, macroscopic discontinuity in a rock, which separates two rock surfaces. Fractures occur naturally due to physical processes of deformation or diagenesis (Nelson, 2001). Fractures can also be caused by disturbance from drilling or injection of fluids (Iding and Ringrose, 2010). These processes lead to a loss of cohesion along the rock surface. Fractures can occur with or without relative displacement (van Golf-Racht, 1982). If displacement does occur the fracture is defined as a fault, and in the case of no displacement the fracture is defined as a joint. Fractures vary significantly in size from a few micrometers to hundreds of kilometers (Berkowitz, 2002).

A reservoir where fractures are predicted to have a pronounced effect on the flow of fluids is called a fractured reservoir (Nelson, 2001). The fractures can contribute to increased permeability and fluid volume in the reservoir, but can also have a negative impact and act as fluid flow barriers. Four different types of fractured reservoirs can be defined (Allan and Sun, 2003):

- Type I: Matrix has minimal or no porosity and permeability. Fluids are stored in fractures and these provide pathways for fluid flow.
- Type II: Matrix has low porosity and permeability. Fluids are stored both in the matrix and in fractures but are transmitted through fractures.
- Type III: Matrix has high porosity and low permeability. Fluids are mainly stored in the matrix while fractures provide increased fluid flow.

- Type IV: Matrix has high porosity and high permeability. Fractures provide little or no additional fluid flow pathways, and might even work as barriers against fluid flow (Nelson, 2001).

Hydrocarbon reservoirs of type I, II and III are producible only due to reservoir fractures, because of the low matrix permeability.

3.2 CO_2 PROPAGATION IN FRACTURED GEOLOGICAL MEDIA

Characterization of CO_2 flow in fractures is complex, and rely on information gathered by different evaluation methods (Iding and Ringrose, 2010). Characterizing fractured media includes defining the location, length, width, orientation, and nature of a fracture, and also the spatial distribution, intensity, density and connectivity if there are several fractures present (van Golf-Racht, 1982). Fractures are detected and evaluated either directly by examination of outcrops or core samples, or indirectly by imaging techniques and logging while drilling, for instance. Information about fractures also rely on extrapolation of available data (Berkowitz, 2002).

Fractures affect fluid flow in a different manner than conventional porous media. In type I, II and III reservoirs the system of fractures with low porosity and high permeability within a matrix with higher porosity and lower permeability is complicated. High permeabilities in fractures compared to the rock matrix lead to more prominent displacement instabilities, as the injected CO_2 tends to flow in the high permeable areas (Haugen et al., 2014). This is illustrated in Figure 10. The usage of foam instead of pure CO_2 is highly applicable in fractures, because foam decreases the mobility of CO_2 more in high permeable regions (Skarestad and Skauge, 2013). This characteristic is useful in reducing the leakage risk in a CCS context, where high permeable zones are regarded as important leakage pathways (Damen et al., 2006).

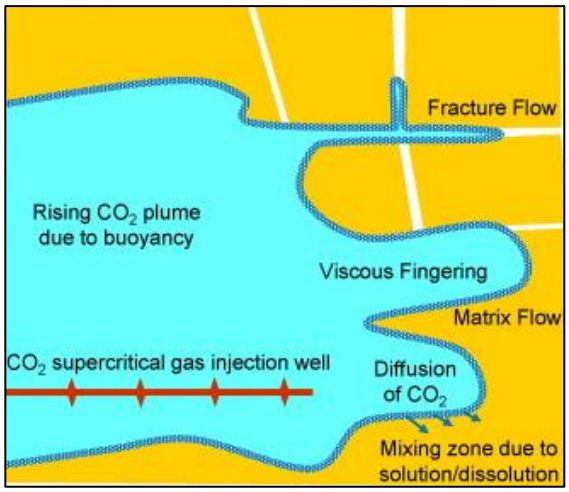

Figure 10 – Illustration of processes that affect the flow of supercritical CO_2 injected in a fractured media saturated with brine. (Iding and Ringrose, 2010)

An example of a CO_2 storage site where fractures impact storage performance is the In Salah site in Algeria (Iding and Ringrose, 2010). This is one of the world's leading onshore CCS projects, where more than 3.8 Mt CO_2 have been stored since injection started in 2004 (Ringrose et al., 2013). At In Salah supercritical CO_2 is stored in a heterogeneous saline sandstone aquifer with varying permeability of 1-100 mD (Iding and Ringrose, 2010). Fractures of higher permeability have been detected, which influences the CO_2 migration in the aquifer. The fractures have been generated both naturally and during drilling and injection, and have also propagated into the lower parts of the cap rock. This could possibly lead to CO_2 leakage to the surface, but no indications of leakage through the sealing formation have been found (Ringrose et al., 2013).

3.3 Displacement Efficiency

In an oil recovery, the total displacement efficiency, or recovery factor, E_R, is defined as the ratio between the volume of oil produced and the volume of oil originally in place in a reservoir (Skarestad and Skauge, 2013). This can be adapted to a CO_2-brine displacement, where the displacement efficiency is presented by the ratio between the volume of brine produced, $V_{w,prod}$ [ml], and the volume of brine initially in place, V_w [ml]. The total displacement efficiency is expressed as a product of the microscopic sweep efficiency, E_D, and the volumetric sweep efficiency, E_{vol}:

$$E_R = \frac{V_{w,prod}}{V_w} = E_D E_{vol} \tag{5}$$

where E_D is the volume of displaced brine relative to the volume of contacted brine, and E_{vol} is the volume of contacted brine relative to the volume of brine originally in place (Skarestad and Skauge, 2013).

4 LITERATURE SURVEY

4.1 FOAM BEHAVIOR IN POROUS MEDIA

Mobility control through alternate injection of gas and surfactant solution was first suggested in 1980, by Lawson and Reisberg (1980). Injections were performed in both sandstone and carbonate cores, and foam was found to reduce the occurrence of gravity segregation and improve stability to viscous forces. The mechanisms of foam flow were not well understood at the time, but has since been investigated through several laboratory tests and field tests, which has resulted in great progress in understanding foam mobility control (Li et al., 2010).

One of the most successful field tests on foam mobility control has been performed at the Snorre field on the Norwegian continental shelf in the North Sea (Blaker et al., 1999, Skauge et al., 2002). The main oil recovery method in the Snorre field was water-alternating-gas (WAG) injection, but early gas breakthrough resulted in limited oil production. A foam assisted WAG injection strategy was applied for gas mobility control in the western fault block on the field. The application of foam reduced the gas-oil-ratio and delayed gas breakthrough, which in turn increased oil recovery (Skauge et al., 2002). Improvement in oil recovery rate is shown in Figure 11.

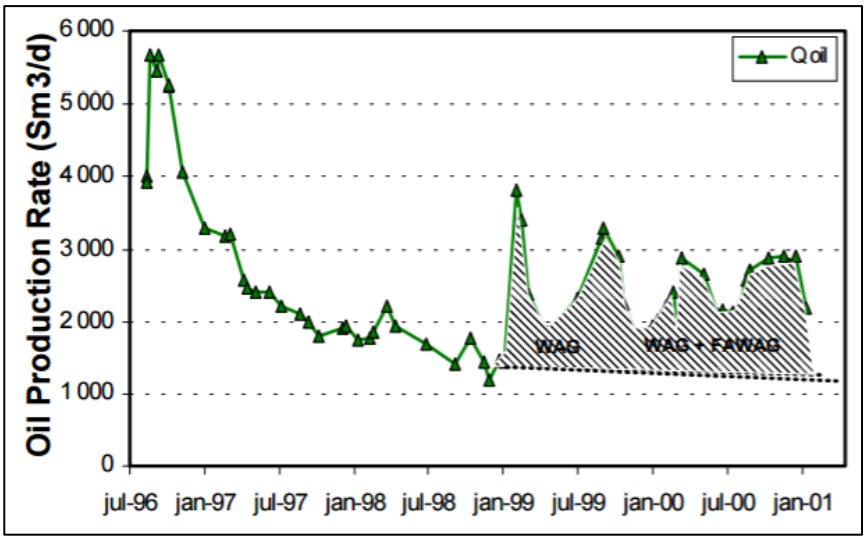

Figure 11 – Oil production rate in a production well (P39) in the western fault block of the Snorre field, where foam assisted water-alternating-gas injection was applied to improve sweep and increase oil recovery. (Skauge et al., 2002)

The difference in foam transport in a sandstone core filled with brine and a sandstone core pre-flushed with surfactant solution has been investigated by Kovscek et al. (1993). Co-injection of gas and surfactant solution in a core plug initially saturated with surfactant solution resulted in

a rapid pressure build-up and resistance to flow. In a brine saturated core, the pressure response was significantly slower. Undispersed gas in a core plug saturated with brine displaces the brine rapidly, but when the core is saturated with surfactant solution, a second foam front forms instead. Pre-injection of surfactant solution satisfies the rock adsorption of surfactant and prevent surfactant retention (Kovscek et al., 1993).

Laboratory experiments using CO_2 foam in a CCS context have been performed by Batôt et al. (2016) as part of a project on storage remediation technologies, where the use of foam can prevent leakage and secure the storage operation. Experiments were done on Clashach sandstones with porosity of 10-20% and permeability of 225-1550 mD. CO_2 and surfactant solution were co-injected with a gas fractional flow of 0.7. Saturation profiles were measured with MRI in a low pressure system and X-ray attenuation in a high pressure system. At low pressure, a strong pressure drop and thus reduction of gas mobility was only observed at water saturations below 15%. The efficiency of foam was evaluated through the apparent viscosity of the foam compared to the viscosity of brine during a single-phase brine injection. Foam reduced the gas mobility and proved efficient for a wide range of flow rates from 1 cc/h-100cc/h, at both low and high pressure.

4.2 Foam Behavior in Fractures

Investigation of foam behavior in fractures is limited compared to foam in unfractured, porous media. Studies of foam flow in a rough-walled rock fracture was performed by Kovscek et al. (1995), where nitrogen gas and surfactant solution were co-injected with different foam qualities. Foam was both pre-generated in a Berea sandstone, and generated directly in the fracture. During pre-generation of foam in a Berea sandstone, it was observed that bubble size increased with increasing flow rate of gas. Increased liquid flow rate resulted in smaller bubbles. It was possible to observe the foam flow in the fracture, and a transition from polyederschaum to kugelschaum was observed at a foam quality of approximately 0.91. Below this foam quality the bubbles were spherical. Mobility reduction factors were calculated to 100-540, depending on foam quality. Pre-generated foam reduced the mobility more than foam generated in-situ in the fracture.

Foam flow in fractures with different foam quality was also studied by Buchgraber et al. (2012). Both smooth and rough-walled fractures were studied. Lower mobility reduction was seen in smooth fractures, where the mobility reduction factor varied between 10-300 compared to 400-500 in rough fractures, where friction caused a higher differential pressure. Mobility reduction

factors were shown to increase linearly with foam quality up to 90%. Foam coalescence was prominent for foam quality above 90%. The difference between foam flow in smooth and rough-walled fractures, and in fractures with different aperture show the importance of fracture characterization.

A study performed on fractured carbonate core plugs by Fernø et al. (2015) investigated the effects of foam for mobility control for enhanced oil recovery in fractured media. After injection of 2 pore volumes of pure CO_2, an average of 39% oil originally in place (OOIP) was produced in fractured cores, compared to an average of 87% OOIP in unfractured carbonate cores. Pure CO_2 injection in fractured cores was described by rapid CO_2 breakthrough, low oil recovery rate, long tail production after CO_2 breakthrough, and no differential pressure across the core plugs, pointing at oil production driven by diffusion, and negligible drive from viscous forces. By injecting CO_2 foam in the fractured cores, the oil recovery rate improved by an average of 30%, as seen in Figure 12. Final oil recovery was not increased, because the microscopic displacement efficiency remained unchanged in systems of this size. The increased oil recovery rate was due to reduced conductivity in fractures, that increased the differential pressure and added a contribution from viscous forces to drive the recovery.

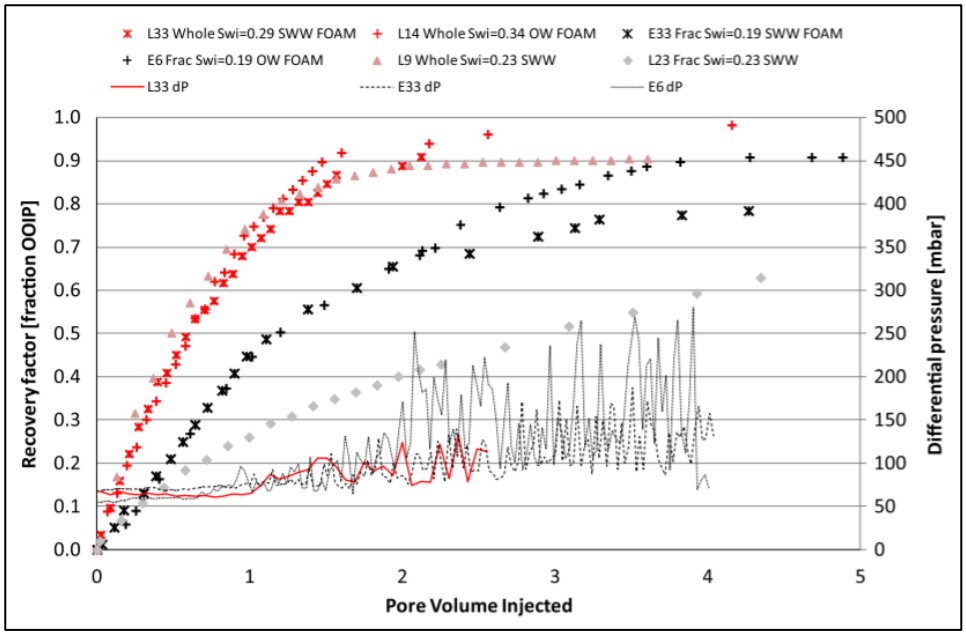

Figure 12 – Oil recovery factor and differential pressure during pure CO2 injections and CO2 foam injections in fractured and whole carbonate core plugs. Strongly water wet (SWW) and oil wet (OW) systems are represented. (Fernø et al., 2015)

Improved oil recovery through foam mobility control was also confirmed in a study by Fernø et al. (2016), where foam generation, flow and sweep efficiency during co-injection and alternating gas and surfactant injection in heterogeneous carbonate fracture networks were

investigated. Comparing foam with pure gas injection by studying local sweep efficiency demonstrated delayed gas breakthrough and increased areal sweep. Gas mobility was reduced with a factor between 200 to more than 1000. Considering foam generation, it was found that foam was generated exclusively by the snap-off mechanism in the studied fracture networks.

Part II – Experimental Procedures

5 EXPERIMENTAL OBJECTIVE

In this study, the objective was to investigate foam flow behavior in 100% brine saturated media, to resemblance CO_2 sequestration in saline aquifers. Investigations were performed on core scale, which is illustrated in Figure 13. Two different types of core material were used, to investigate the difference between foam flow in porous media versus fractured, non-porous media. Quantitative analysis of differential pressure and fluid saturations were performed to study the fluid behaviors during injections. Water saturation development was monitored through resistivity measurements and the principle of material balance. Finally, certain core plugs were imaged with NMR technology to monitor fluid flow and fluid distribution. The MR imaging was performed at Statoil's laboratories at Sandsli, Bergen. The rest of the experiments presented in this thesis were performed at the Department of Physics and Technology (IFT), at the University of Bergen (UoB). An overview of all experiments conducted is presented in Table 1. Most experiments were performed in collaboration with fellow master student Solveig Carlsen (see detailed lists of experiments in Appendix F).

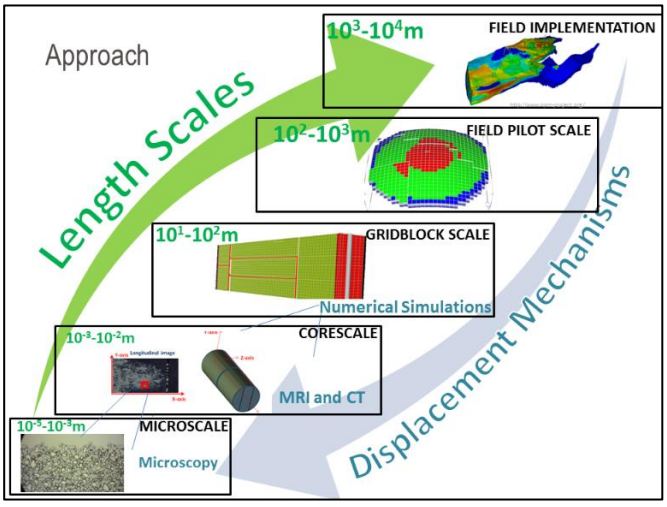

Figure 13 – Illustration of different scales used in evaluation of reservoir and fluid properties, from microscale to implementation in the field. Experiments in this study were performed on core scale. (Fernø, 2015)

Table 1 – Overview of experiments performed in investigations for this thesis. Most experiments (except 4 foam injections in marble cores and 1 baseline injection in sandstone cores) were performed in collaboration with fellow master student Solveig Carlsen.

Core material	Experiment	Conditions	Number of experiments
Fractured marble	Baseline injection	21° / 1 bar	23
Fractured marble	Foam injection	21° / 2 bar	9
Fractured marble	Dynamic MRI	21° / 2 bar	1
Bentheimer sandstone	Baseline injection	21° / 70 bar	2
Bentheimer sandstone	Baseline injection	21° / 10 bar	2
Bentheimer sandstone	Foam injection	21° / 70 bar	2
Bentheimer sandstone	Foam injection	21° / 1 bar	2
Bentheimer sandstone	Foam injection	21° / 10 bar	6

Some of the conducted experiments are for various reasons not included in the discussion in this thesis. Different experimental conditions were tested to optimize the procedures, and some experiments were not successful because of experimental errors or defects in equipment. Still, all experiments have given valuable experience that has been used to improve experimental setups and procedures.

6 FLUIDS AND CORE MATERIALS

6.1 FLUIDS

A list of fluids used in experiments, and fluid properties, are given in Table 2. Prior to most experiments the core plugs were 100% saturated with 1 wt% NaCl brine. Baseline injections were performed in both types of core material. In fractured marble cores, baseline experiments were performed with N_2 gas, while baseline experiments in sandstone cores were performed with CO_2 gas.

To generate foam and perform foam injections, gas and surfactant solution were co-injected into the core material. Once again, injections in fractured marble cores were performed with N_2 gas, while CO_2 gas was injected in sandstone cores. The surfactant solution consisted of 1 wt% Huntsman Surfonic® L24-22 dispersed in 1 wt% NaCl brine. A gas fractional flow of 0.7 relative to surfactant solution was used for all co-injections. Higher gas fractions were tested, but were not equally successful in generating foam. Previous master student Sigbjørn A. Johansen tested foam stability with various gas fractions and found that the best foam quality was obtained with high gas fractional flow between 0.7-0.9 (Johansen, 2016).

NaCl brine is most suitable for use in sandstone cores, as it may react with minerals in marble rocks and dissolve the rock. For marble cores, $CaCl_2$ brine would have been a better alternative, but former studies by Haugen et al. (2012) have shown that Calcium ions interact with certain types of surfactant and cause surfactant precipitation, which again causes unstable foam. The effect of NaCl brine on marble cores is discussed in Appendix C.

Table 2 – Fluids used in experiments in this study.

Fluid	Composition	P-T conditions	Fluid phase
Brine	1 wt% NaCl	21° / 1 bar	Liquid
	Distilled water	21° / 2 bar	Liquid
		21° / 70 bar	Liquid
Surfactant solution	1 wt% Huntsman Surfonic® L24-22	21° / 1 bar	Liquid
	1 wt% NaCl	21° / 2 bar	Liquid
	Distilled water	21° / 70 bar	Liquid
Nitrogen	>99.999% N2	21° / 1 bar	Gas
		21° / 2 bar	Gas
Carbon dioxide	>99.999% CO2	21° / 1 bar	Gas
		21° / 2 bar	Gas
		21° / 70 bar	Liquid

6.2 CORE MATERIAL

Two different core materials were used in this study, for the purpose of investigating foam behavior in both unfractured porous media and fractures. 2" Bentheimer sandstone cores and 2" marble cores were available at the Department of Physics and Technology at the University of Bergen. Fracture networks were created in the marble cores. All core material was assumed to be strongly water-wet.

6.3 CORE PREPARATIONS

6.3.1 Fractured marble cores

2" cylindrical marble cores with no porosity and permeability were used to create fracture systems. The fractured cores can be defined as a type I reservoir system, as described in section 3.1. The cores were cut to the desired length with a Steinadler saw.

Fractures were created with a modified version of a fracturing method developed by previous master students Sigbjørn A. Johansen and Snorre S. Vasshus (Johansen, 2016, Vasshus, 2016). These students used a fracturing device to generate rough-walled fractures in the cores. Each core was placed horizontally between two metal blocks with a curved immersion in the center. Two metal rods attached to the blocks were placed on top and bottom of the core to provide a concentrated area of stress. Modification to the method was done by sharpening the edges of the metal rods, to obtain cleaner fracturing with limited amount of debris.

The core was held in place between the metal blocks, while slowly lowering an extension arm driven by a hydraulic press. Once the core was properly adjusted between the blocks, overburden pressure was applied by manually regulating a handle. To create one, single fracture the stress was applied in intervals of short duration until the core fractured. Figure 14 shows the fracturing procedure step by step. To generate various fracture systems, some cores were cut in several pieces that could be fractured one by one. When fractured, the core pieces were puzzled back together and wrapped in plastic foil.

Figure 14 – Fracturing procedure for marble cores. a) Overburden pressure was applied with a hydraulic press. b) Sharp metal rods concentrated the contact area where stress was applied. c) Clean, rough-walled fractures were generated. d) Two core pieces put back together again after fracturing.

Two core plugs, entitled OMS_1 and OMS_2, were first prepared and tested for experiments, but were discovered to be inapplicable for NMR imaging. Core OMS_1 was fractured with a single fracture across the whole length of the core. The core pieces were wrapped in aluminum foil and a 0.05 cm thick shrink sleeve, which was shrunk with a heating gun to hold the core pieces tight together. Specially designed end pieces made of polyoxymethylene (POM) material were attached to each end of the core, using one layer of blue epoxy, as shown in Figure 15. Porosity and permeability measurements and three N_2 gas injections were performed on the core. Aluminum foil is not applicable in NMR imaging, as the aluminum may interact with the magnetic field in the MR scanner. Because of this the core plug was not used for further experiments.

Figure 15 – Core plug OMS_1, prepared with aluminum foil, shrink sleeve, epoxy and end pieces.

In core OMS_2, one fracture was first generated in the core plug, before the core was cut in three pieces of approximately similar length, which were put back together again with different fracture orientations. New POM end pieces with an outer diameter similar to the diameter of the core plug were designed, and were placed inside the sleeves during shrinking, to attach them to the core pieces. Each end piece had three connection holes that allowed flow through the core plugs, which is shown in Figure 16. The core sample was 100% saturated with brine and brought to Sandsli for NMR imaging. It was discovered that the core was too long (approximately 15 cm) to image the whole core at once, and the core was not applied for any experiments.

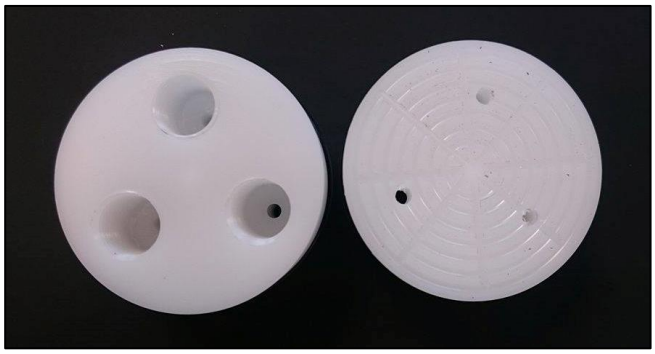

Figure 16 – End pieces designed for fractured marble cores.

Three new, approximately 10 cm long, marble cores with different fracture systems were prepared and used for further experiments. The cores were entitled M2i-1, M2i-2 and M2i-3, where “M2i” was short for “Marble 2 inches”. Fracture systems are illustrated in Figure 17. Core M2i-1 had the most complicated fracture system: the core was first fractured with the hydraulic press, resulting in one fracture across the length of the core. The core pieces were put back together with duct tape, before the saw was used to cut the core into four pieces of approximately equal length. The pieces were put together again so that the original fractures were aligned almost perpendicular to each other. Core M2i-2 was fractured twice with the hydraulic press. The core pieces were put back together so that two fractures along the core

length were oriented perpendicular to each other. In core M2i-3, one fracture was generated across the whole core length.

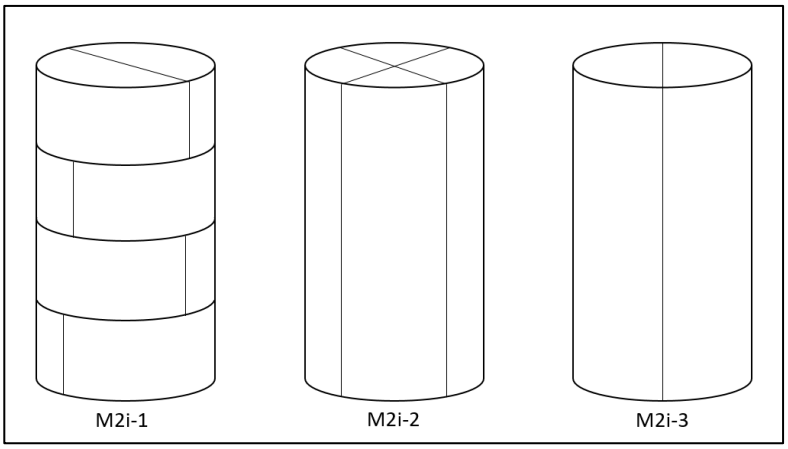

Figure 17 – Illustration of fracture systems in marble cores M2i-1, M2i-2 and M2i-3.

After fracturing, the cores were prepared in a similar manner as core plug OMS_2, with similar, approximately 2" diameter end pieces and shrink sleeves, as shown in Figure 18. Swagelok fittings were mounted to the end pieces.

Figure 18 – Fractured marble core M2i-3 with end pieces, Swagelok fittings and shrink sleeve, before shrinking.

6.3.2 Sandstone cores

A total of 13 outcrop Bentheimer sandstone cores were prepared for experiments. All cores were cut to a length of approximately 10 cm. The cores were washed and dried in a heating cabinet at 80°C for at least 24 hours, before routine core analyses and experiments were performed. A sandstone core is shown in Figure 19.

Figure 19 – A Bentheimer sandstone core, used for experiments in this thesis.

7 EXPERIMENTAL SET-UP AND PROCEDURES

7.1 ROUTINE CORE ANALYSIS

Routine core analysis (porosity and permeability measurements) was performed on each core plug. Porosity describes the ratio between the pore volume and the bulk volume of a rock. Bulk volume of each core plug was found by measuring lengths and diameters with a caliper. Pore volumes were calculated based on the principle of mass balance and the definition of density, which were applied by measuring dry mass and mass of core plugs 100% saturated with brine.

Permeability is the measure of a rock's ability to transmit fluids. Absolute permeability is the permeability of a rock where only one fluid phase is present. Absolute permeability in each core plug was calculated with Darcy's law, by injecting brine with different flow rates in 100% brine saturated cores, while measuring the differential pressure across the core plugs. The differential pressure was measured with an ESI pressure transducer at the core inlet, while the outlet pressure was assumed to be atmospheric. Differential pressure was plotted against injection rate, and a linear trendline was added. Offset in the ESI pressure transducer was corrected for by adjusting the differential pressure to form a plot that fits a linear trendline crossing the origin. The corrected values for differential pressure were used to calculate the absolute permeability with Darcy's law.

7.1.1 Porosity and permeability measurements in fractured marble cores

In the fractured marble rocks, the fracture volume constitutes the pore volume. Dead volumes in end pieces and Swagelok fittings of the marble cores were measured in advance, and taken into account when calculating the porosity. Before brine saturation, the cores were vacuumed with a vacuum pump for approximately one hour, to ensure 100% brine saturation. The cores were connected to the vacuuming pump system with 1/8" nylon tubing, and saturated with brine from a beaker, as shown in Figure 20. After approximately one hour, the cores were fully saturated, and were weighed for porosity calculations.

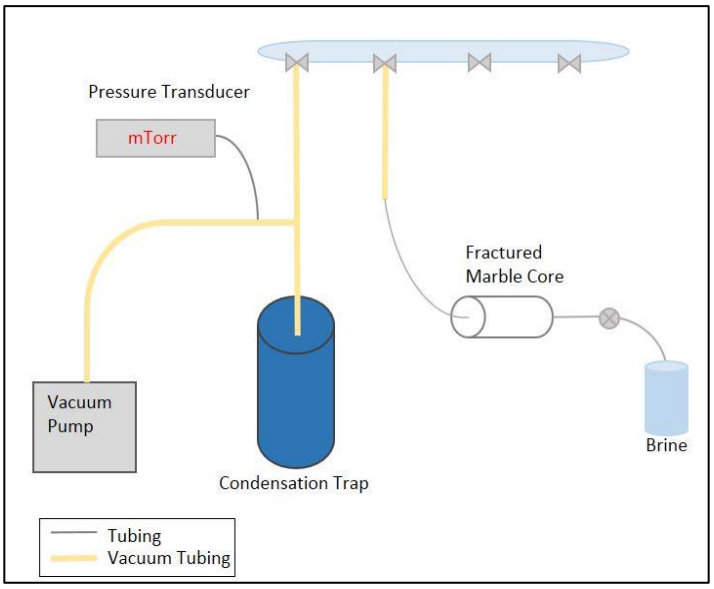

Figure 20 – Experimental setup for porosity measurements in fractured marble cores. (Illustration by collaboration partner Solveig Carlsen)

Experimental setup for permeability measurements in the fractured marble cores is illustrated in Figure 21. Fluids were assumed to flow only in the fractures. Tubing filled with brine was connected to the inlet and outlet of the core end pieces. Brine was injected with a Quizix pump at four different flow rates: 500 cc/h, 600 cc/h, 700 cc/h, and 800 cc/h.

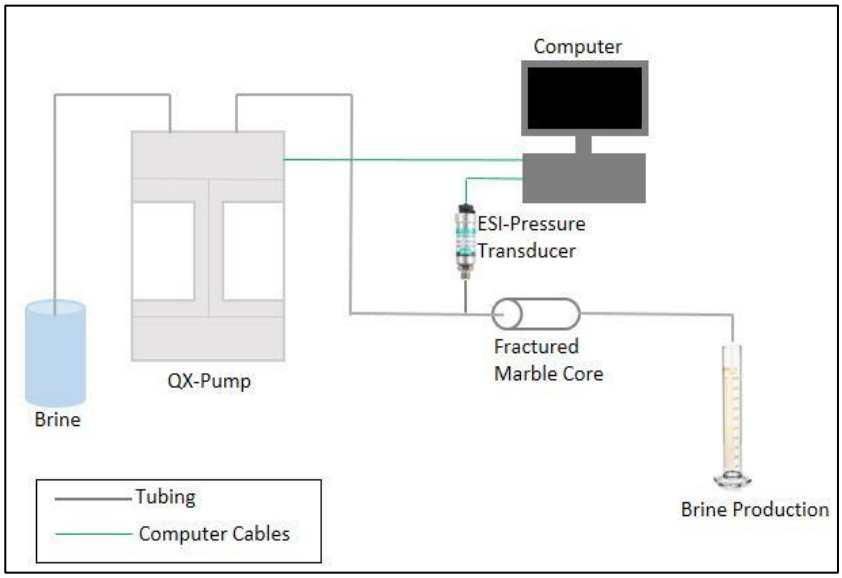

Figure 21 – Experimental setup for permeability measurements in fractured marble cores. (Illustration by collaboration partner Solveig Carlsen)

7.1.2 Porosity and permeability measurements in sandstone cores

For porosity measurements, the sandstone cores were placed in a glass container beneath a separate container with brine, inside a vacuum chamber. The cores were vacuumed for

approximately one hour, and the brine was vacuumed for 10 minutes, before a valve separating the sandstone and brine container was opened, allowing brine to cover the core plug. The cores were submerged in brine for 24 hours to ensure 100% saturation. Experimental setup is shown in Figure 22. When the core plugs were 100% saturated with brine, the cores were weighed as soon as possible, to avoid brine evaporation. The brine-saturated sandstone cores were stored in plastic containers filled with brine.

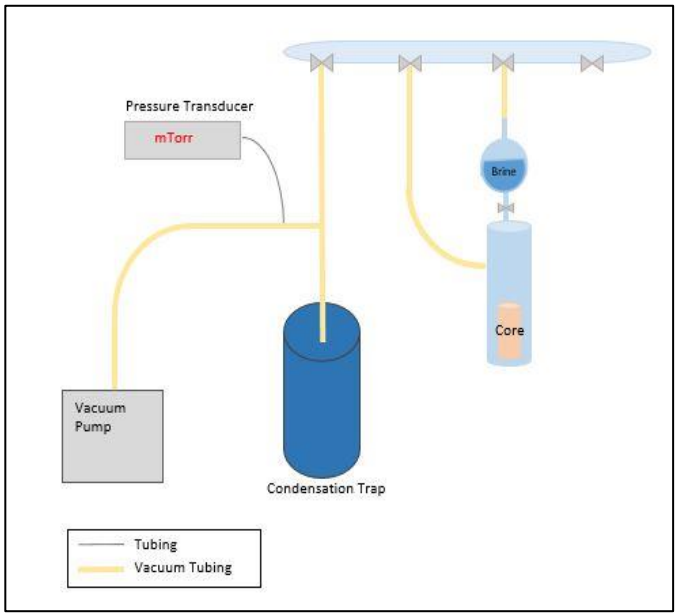

Figure 22 – Experimental setup for porosity measurements in sandstone cores. (Illustration by collaboration partner Solveig Carlsen)

For permeability measurements, sandstone cores were placed in a Hassler core holder, and applied a confinement pressure of 10 bar to ensure fluid flow through the core plugs. A Pharmacia pump was used for injections, and brine was injected with injection rates of 499 cc/h, 450 cc/h, and 400 cc/h. The experimental setup is shown in Figure 23.

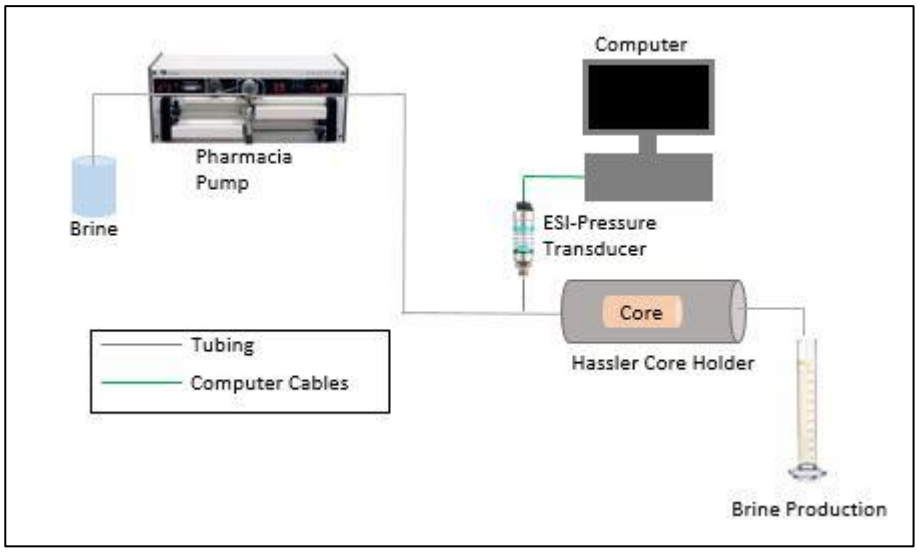

Figure 23 – Experimental setup for permeability measurements in sandstone cores. (Illustration by collaboration partner Solveig Carlsen)

7.2 Experimental Procedures in Fractured Marble Cores

A list of experiments performed on fractured marble cores is found in Table 3. Only experiments discussed in part III are included. A complete overview of experiments conducted can be found in Appendix F. The core plugs were initially 100% saturated with brine or surfactant solution before all experiments, and were re-saturated using the same setup as for porosity measurements, explained in section 7.1.1. The cores were weighed to ensure that 100% brine saturation was achieved after re-saturation. Dead volumes in the experimental systems were measured in advance, by injecting brine and monitor the injected volumes with the injection pump.

Table 3 – An overview of successful experiments conducted with fractured marble cores.

Core ID	Experiment	Date	T/P conditions	Collaboration partner
M2i-1	N_2 injection (baseline)	21.03.2017	21 °C / 1 bar	Solveig Carlsen
M2i-1	N_2 foam injection	24.03.2017	21 °C / 2 bar	Solveig Carlsen
M2i-1	N_2 foam injection	27.03.2017	21 °C / 2 bar	
M2i-1	MRI of N_2 foam injection	06.04.2017	21 °C / 2 bar	Solveig Carlsen
M2i-2	N_2 injection (baseline)	21.03.2017	21 °C / 1 bar	Solveig Carlsen
M2i-2	N_2 foam injection	24.03.2017	21 °C / 2 bar	Solveig Carlsen
M2i-2	N_2 foam injection	27.03.2017	21 °C / 2 bar	
M2i-3	N_2 injection (baseline)	21.03.2017	21 °C / 1 bar	Solveig Carlsen
M2i-3	N_2 injection (baseline)	21.03.2017	21 °C / 1 bar	Solveig Carlsen
M2i-3	N_2 foam injection	27.03.2017	21 °C / 2 bar	
M2i-3	N_2 foam injection	27.03.2017	21 °C / 2 bar	

7.2.1 N_2 gas injection in fractured marble cores at low pressure

N_2 gas injections were performed as baseline experiments in 100% brine-saturated fractured marble cores. The experiments were carried out in ambient temperature and pressure conditions, of approximately 21°C and atmospheric pressure. A schematic overview of the experimental setup is shown in Figure 24.

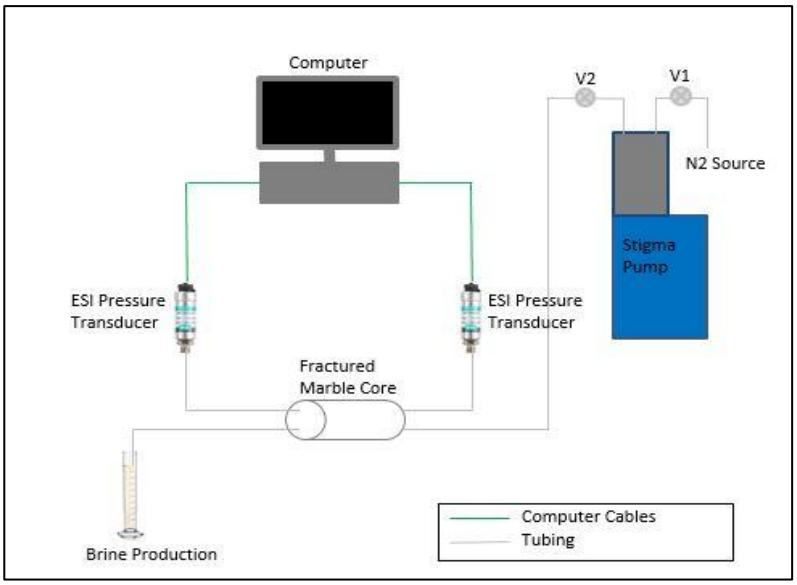

Figure 24 – Schematic of experimental setup for pure N_2 gas injections in fractured marble cores. A N_2 tank was used as gas source. Inlet and outlet pressures were measured with ESI pressure transducers of range 0-6.0 bar and 0-2.5 bar, respectively. 1/8" nylon tubing, 1/8" stainless steel tubing and Swagelok fittings and valves were used to connect the experimental system. The Stigma pump and ESI pressure transducers were managed with a computer. (Illustration by collaboration partner Solveig Carlsen)

The core plugs were horizontally oriented and taped to the table to hold a certain orientation. Differential pressure over the core plug was measured with ESI pressure transducers directly connected to the end pieces at one of the inlet and outlet connections. The ESI pressure transducers were controlled with a computer program. Tubing for injection and production was connected to the lowest core inlet and core outlet connections, while the last inlet and outlet connections were closed throughout the experiments. N_2 gas was supplied from a nitrogen tank used to fill the injection pump. One to two pore volumes of N_2 gas was injected in each core, with injection rate 50 cc/h. Water production was measured in a measuring cylinder.

7.2.2 N_2 foam injections in fractured marble cores at low pressure

For foam generation in fractured marble cores, N_2 gas and surfactant solution was co-injected. The injections were performed with a backpressure of 2 bar, to create stable foam. The experiments were conducted at ambient temperature, of approximately 21°C. Two foam injections were conducted in each core. The core plugs were initially 100% saturated with brine before the first set of foam injections, but were re-saturated with surfactant solution before the second set of foam injections. An illustration of the experimental setup is presented in Figure 25.

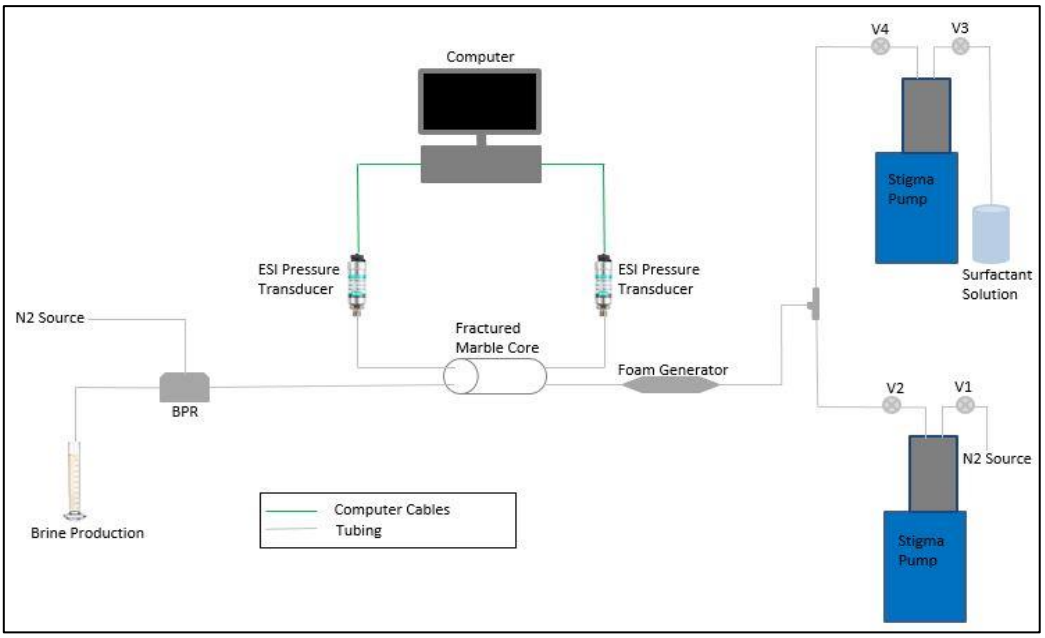

Figure 25 – Experimental setup during co-injection of N_2 gas and surfactant solution in fractured marble cores. A nitrogen tank was used as gas source for injection and to maintain the backpressure in the Backpressure Regulator (BPR). Water production was measured in an inverted imbibition cell. ESI pressure transducers were used to measure the inlet and outlet pressures, with range 0-6.0 bar and 0-2.5 bar, respectively. Foam was pre-generated in a foam generator placed close to the core inlet. 1/8" nylon tubing, 1/8" and 1/16" stainless steel tubing and Swagelok fittings and valves were used to connect the experimental system. The Stigma pumps and ESI pressure transducers were managed with a computer. (Illustration by collaboration partner Solveig Carlsen)

A foam generator, shown in Figure 26, was placed in front of the core plugs to pre-generate foam before entering the cores. The foam generator was made by a design tested by fellow master student Connie Wergeland. It consisted of a 1/4" steel tubing, filled with sand of grain size 125-250 µm. The sand was held in place with glass wool and a steel filter in each end of the tubing. The glass wool was carefully handled, using gloves, a mask and safety glasses. Swagelok fittings were mounted to each end of the tubing, to enable transition between 1/4" tubing and 1/8" tubing. The foam generator was 13.80 cm (±0.05 cm) long.

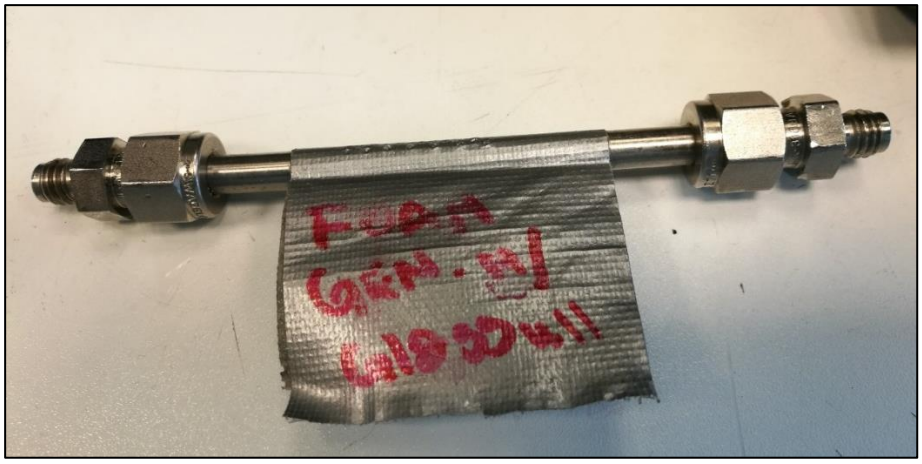

Figure 26 – Foam generator used in experiments in both fractured marble cores and sandstone cores.

The shrink sleeves did not hold the core pieces and end pieces together at a pressure higher than approximately 1.4 bar, hence three different methods were tested to be able to increase the system pressure further. In the first method, duct tape was wrapped around the core plugs, as shown in Figure 27. Two experiments were performed on duct taped core plugs. The method allowed a system pressure of at least 2 bar, but the duct tape inhibited visual observations of the fracture network.

Figure 27 – Fractured marble core with duct tape holding the core pieces and end pieces together at sufficiently high pressure for foam generation.

A second method was tested, using transparent Casco strong, rapid epoxy. The epoxy was applied to each end of the core plug. Foam injection was tested when the epoxy had dried overnight, but the epoxy did not withstand higher pressures than 1.4 bar before the end pieces sled apart from the core pieces.

Finally, a combination of duct tape and transparent epoxy was tested, where duct tape was fastened over a layer of epoxy, and a second layer of epoxy was applied on top of the duct tape. The combination of duct tape and epoxy did withstand a system pressure high enough to generate stable foam. A core plug fixed with duct tape and epoxy is shown in Figure 28.

Figure 28 – Fractured marble core M2i-3 with two layers of epoxy, separated with duct tape, to hold end pieces and core pieces together during foam injection at 2 bar.

During foam injections, differential pressure was measured with ESI pressure transducers attached to the end pieces at inlet and outlet. Volume of injected surfactant was logged with the pump program at the computer. Tubing for injection and production was filled with brine before it was connected to the core plug, at the lower inlet and outlet connections. The cores were flushed with approximately two pore volumes of surfactant solution at a rate of 50 cc/h before co-injection, to exchange the saturation fluid and stabilize surfactant adsorption. When two pore volumes of surfactant solution had been injected, the system pressure had adjusted to the pressure in the BPR. The N_2 pump was adjusted to a pressure approximately 0.1 bar over the system pressure, to prevent backflow into the N_2 pump.

A total rate of 50 cc/h was used for foam injection, with a gas fraction of 0.7 relative to surfactant solution. This resulted in a surfactant injection rate of 15 cc/h and a gas injection rate of 35 cc/h. N_2 gas injection was started simultaneously as the surfactant injection rate was changed from 50 cc/h to 15 cc/h, by opening a valve between the system and the N_2 pump (the N_2 pump was started 30 s in advance, which did not create significant pressure increase). This was done without interrupting the flow of surfactant between pure surfactant injection and foam injection. Production was measured in an inverted imbibition cell at certain time intervals throughout the entire co-injection. Nylon tubing made it possible to monitor the fluid flow in

the system, except inside the core plugs and attached end pieces. Two pore volumes of foam were injected in each core plug, dead volumes considered, before injection of N_2 gas and surfactant solution was stopped simultaneously. The system was depressurized by opening to atmospheric pressure.

7.3 Experimental Procedures in Bentheimer Sandstone Cores

A detailed list of successful experiments performed on sandstone cores are presented in Table 4. Only experiments discussed in Part III are included in the table, but a complete overview of experiments is found in Appendix F. Different pressure regimes were tested before it was concluded that a backpressure of 10 bar seemed to give relatively stable foam. The core plugs were initially 100% saturated with brine before all experiments, and were re-saturated using the same setup as for porosity measurements, explained in section 7.1.2. The cores were weighed after being re-saturated, to ensure 100% brine saturation. Dead volumes in the experimental systems were measured prior to the experiments, by injecting brine and monitor the injected volumes with the injection pump.

Table 4 – An overview of successful experiments conducted with Bentheimer sandstone cores.

Core ID	Experiment	Date	T/P conditions	Collaboration partner
S2i-7	CO_2 foam injection	13.03.2017	21 °C / 10 bar	Solveig Carlsen
S2i-9	CO_2 foam injection	15.03.2017	21 °C / 10 bar	Solveig Carlsen
S2i-10	CO_2 injection (baseline)	23.04.2017	21 °C / 10 bar	Solveig Carlsen (alone)
S2i-11	CO_2 injection (baseline)	24.04.2017	21 °C / 10 bar	Solveig Carlsen
S2i-12	CO_2 foam injection	24.04.2017	21 °C / 10 bar	Solveig Carlsen
S2i-13	CO_2 foam injection	25.04.2017	21 °C / 10 bar	Solveig Carlsen

7.3.1 CO_2 gas injection in sandstone cores at low pressure

CO_2 gas injections were performed as baseline studies in sandstone cores. Experiments were done at a system pressure of 10 bar and ambient temperature conditions of approximately 21°C. Baseline injections were performed in two different core plugs, S2i-10 and S2i-11. The experimental setup is illustrated in Figure 29.

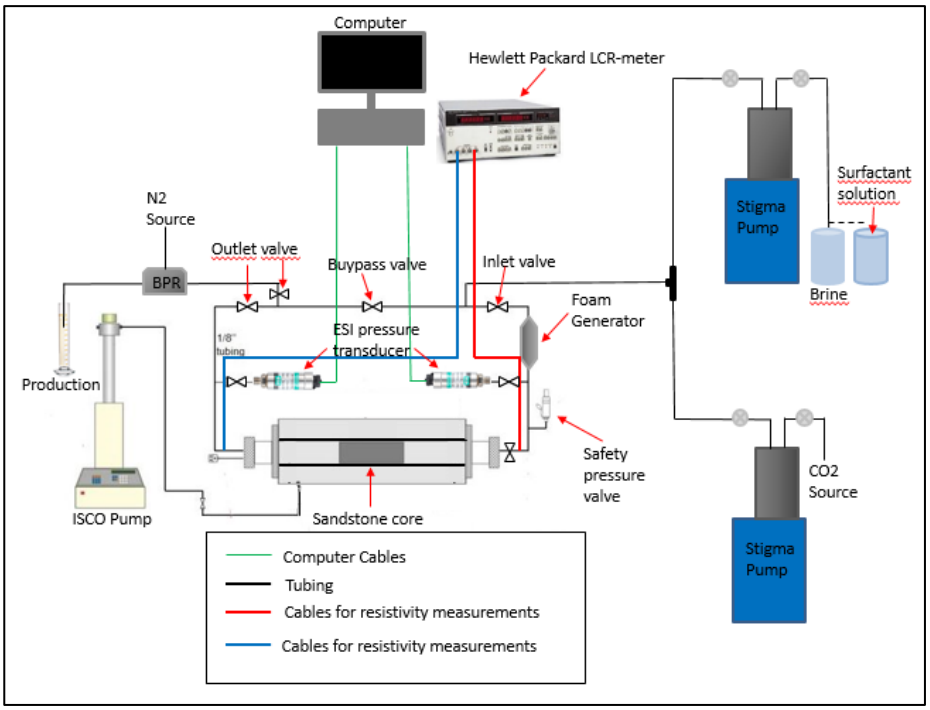

Figure 29 – Experimental setup during pure CO_2 gas injections and co-injections of CO_2 gas and surfactant solution in Bentheimer sandstone cores. CO_2 was provided from a CO_2 tank. Inlet and outlet pressures were measured with ESI pressure transducers, with range 0-40 bar and 0-25 bar, respectively. Electrical resistance in the core plug was measured with an LCR-meter. Confinement pressure was applied by injecting oil with an ISCO pump. A N_2 tank was used as gas source to control the BPR. Foam was pre-generated in a foam generator, placed close to the core inlet. The foam generator was removed during pure CO_2 gas injections. 1/8" and 1/16" stainless steel tubing and Swagelok fittings and valves were used to connect the experimental system. The Stigma pumps and ESI pressure transducers were managed with a computer. (The schematic is modified from Hågenvik (2013), by collaboration partner Solveig Carlsen)

The system was filled with brine and the BPR was adjusted to approximately 10 bar, before placing the core in the core holder. ESI pressure transducers were connected for pressure measurements at the core inlet and outlet. The core was placed in a rubber sleeve to protect against leakage of confinement oil, and to allow resistivity measurements. The sleeve and core plug was placed on the outlet core holder end piece before it was pushed horizontally into the core holder, and then connected to the inlet end piece. Confinement pressure of 30 bar was applied by injecting lamp oil into the core holder with an ISCO pump. The system pressure was increased to 10 bar by injecting brine from both sides of the core holder with the bypass valve open, until brine was let through the BPR. The confinement pressure was adjusted to 40 bar, to maintain a pressure of 30 bar over the system pressure. Electric cables were attached to the tubing at inlet and outlet and connected to a LCR-meter, to measure electrical resistance and calculate the resistivity in the core plug. Measurements of electrical resistance was possible because of the floating rubber sleeve and floating core holder end pieces. The principle of resistivity is explained in section 7.3.3.

The bypass valve and the valve between the brine pump and the system were closed before CO_2 injection started. Inlet and outlet pressure, water production and electrical resistance were measured through the entire injection. Two pore volumes of CO_2 were injected, at a flow rate of 50 cc/h. The system pressure was decreased to atmospheric pressure before the core was taken out of the core holder.

7.3.2 CO_2 foam injection in sandstone cores at low pressure

Co-injection of CO_2 and surfactant solution was performed to generate CO_2 foam in sandstone cores. The system pressure during injections was 10 bar and the experiments were done in ambient temperature of approximately 21°C. Successful foam injections were performed in four sandstone cores: S2i-7, S2i-9, S2i-12 and S2i-13. The experimental setup is illustrated in Figure 29, section 7.3.1.

The same experimental setup as the one used for baseline injections was used for foam injections, except for a foam generator located close to the core holder inlet. Foam was pre-generated in the same foam generator that was used for marble cores, but the sand and glass wool were replaced with certain intervals, because the sand became tightly packed after some experiments. ESI pressure transducers were attached to the inlet and outlet of the core holder. The system was filled with brine before the core was placed in the rubber sleeve, and setup in the core holder. A confinement pressure of 30 bar over system pressure was applied, similarly as in the baseline injections. Brine was injected in the system to increase the pressure until the BPR let through production at approximately 10 bar. Electric cables were attached at inlet and outlet for resistivity measurements. When the system pressure was stable at approximately 10 bar, the bypass valve and the valve between the brine pump and the system was closed. Brine in the pump was exchanged with surfactant solution, and the pump pressure was raised to the same pressure as in the system, before the pump valve was reopened to inject surfactant solution. Approximately two pore volumes of surfactant solution were injected before foam injection. Surfactant solution was injected at a flow rate of 50 cc/h.

When two pore volumes of surfactant solution were injected the CO_2 pump pressure was adjusted to approximately 0.6 bar over system pressure, to prevent backflow into the CO_2 pump. CO_2 injection was started simultaneously as the injection rate of surfactant solution was decreased to 15 cc/h. CO_2 was injected with injection rate 35 cc/h, which gave a gas fraction of 0.7. Water production, resistance and differential pressure was monitored during the entire foam injection, and surfactant volume injected was logged with the computer. When two pore

volumes of foam had been injected, dead volumes considered, the pumps were stopped simultaneously. The system pressure was slowly decreased to atmospheric pressure.

7.3.3 Resistivity measurements

Electrical resistance is defined as a material's resistance against the flow of an electric current through the material (Lien, 2004). Resistivity, R [Ωm], is the specific resistance of a material, and is defined by the following equation:

$$R = r\frac{A}{l} \tag{6}$$

where r [Ω] is the material's electrical resistance, A [m^2] is the cross-sectional area of the material, and l [m] is the length of the material.

In the petroleum industry, a resistivity tool is used to find fluid and rock properties in a formation. The resistivity tool sends an electric current into the formation to see how well it is conducted. Changes in resistivity indicates different geology and formation fluids. Water and clay conduct electricity and will have low resistivity towards the current. Hydrocarbons and most sedimentary rocks that do not contain significant amounts of water have high resistivity, as they do not transfer electricity easily.

Formation resistivity can be linked to porosity and water saturation (Archie, 1942). Archie defined a formation factor, F, for constant porosity:

$$F = \frac{R_o}{R_w} = \frac{a}{\phi^m} \tag{7}$$

where R_o [Ωm] is the resistivity of the formation 100 % saturated with formation water, R_w [Ωm] is the resistivity of the formation water, a is a parameter describing the tortuosity and pore size distribution of the media, and m is an empirical parameter describing the relation between pores and pore throats, and the number of closed channels, and is called the cementation exponent (Lien, 2004). Archie also defined a resistivity index, I:

$$I = \frac{R_t}{R_o} = bS_w{}^{-n} \tag{8}$$

where R_t [Ωm] is the true resistivity of the formation possibly filled with fluids, which is measured with the resistivity tool. The parameters b and n depend on the formation, and are normally based on empirical evidence and assumptions. b is a parameter describing the

tortuosity in the formation, and *n* is called the saturation exponent and depends on wettability. Equation (8) is known as Archie's second law.

Combining equation (7) and equation (8) gives a relation between water saturation, porosity and resistivity:

$$S_w^n = \frac{a}{\phi^m}\frac{R_w}{R_t} \tag{9}$$

This equation is important for determining the amount of water and hydrocarbons in a formation. The water saturation increases if the water resistivity increases and decreases if the true formation resistivity or the porosity increases.

The LCR-meter used in experiments for this thesis measures the electrical resistance in the sandstone core plugs. Equations (6) and (8) are used to calculate water saturation during fluid injections. R_o is found by measuring the resistivity before injections, when the core plugs are 100% brine saturated. *b* and *n* are assumed to equal 1 and 2, respectively, for experiments conducted in this thesis.

7.4 MAGNETIC RESONANCE IMAGING

7.4.1 Principles of Magnetic Resonance Imaging

Magnetic Resonance Imaging (MRI) or Nuclear Magnetic Resonance Imaging (NMRI) is widely used for different purposes, including petrophysical investigations. Basic principles of NMRI are explained in the following and are illustrated in Figure 30. NMR responds to the presence of protons in an atom with spin, most commonly the isotope ^{1}H of the Hydrogen atom (Elmaoğlu and Çelik, 2011). Hydrogen atoms are present in both water and hydrocarbons. All nuclei which contain even numbers of both neutrons and protons have spin, and possess a magnetic dipole moment.

When a material containing hydrogen or another atom with spin is placed in a static magnetic field, B_o, the protons in the atom will start to rotate around the axis of the direction of the magnetic field, creating magnetic resonance. Magnetic vectors in the rotating protons align either parallel or antiparallel to the larger magnetic field, depending on the energy level of the proton. The sum of all the magnetic vectors constitutes the total magnetization, M_o. The protons

rotate with a certain frequency, called the Larmor frequency, ω_o [MHz] (Elmaoğlu and Çelik, 2011):

$$\omega_o = \gamma B_o \tag{10}$$

where γ [MHz/T] is a constant called the gyromagnetic ratio, that is specific to each proton, and B_o [T] is the strength of the static magnetic field.

To produce an MR-signal, a dynamic magnetic field, B_1, is introduced. B_1 is applied as a pulse that can tilt the M_o magnetization from the Z-axis to the XY-plane. The B_1 pulse, also called *rf* pulse, must be rotating with the Larmor frequency, be perpendicular to B_o and endure long enough to tilt the magnetization to the correct angle. When the rotating spins of the M_o field are tilted, they continue to rotate with the same frequency, but their potential energy is increased.

After the 90° *rf* pulse is applied to the protons in the XY-plane, the protons will eventually return to the Z-plane and their original energy state, a process called relaxation. T_1 relaxation time is defined as the time it takes for the spins to return to 63% of its original state (Elmaoğlu and Çelik, 2011). T_1 depends on the interactions between the spins and their environment, and is also called spin-lattice relaxation time.

After a while the spins start to rotate at slightly different speeds, due to the environment around each spin. T_2 relaxation time, also called spin-spin relaxation time, is defined as the time it takes for the tilted M_o-magnetization to reduce to 37% of its original strength (Elmaoğlu and Çelik, 2011). One method of measuring T_2 is by a CPMG sequence, also called spin-echo sequence, where several 180° pulses follow a 90° pulse. The 180° pulses are separated by a certain time interval 2τ, where τ is called the echo time. T_1 and T_2 relaxation times can be used to find different petrophysical properties like porosity, permeability, and fluid saturations (Lien, 2004).

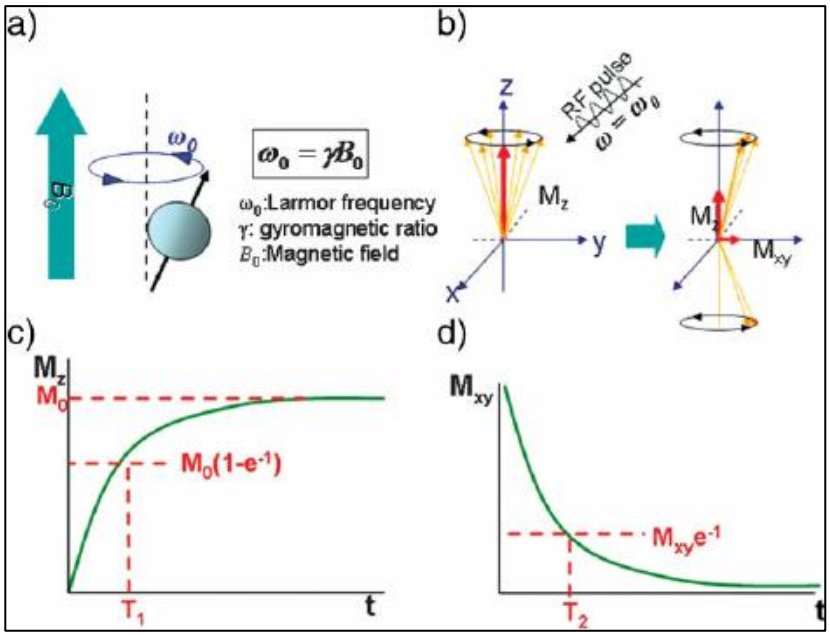

Figure 30 – Principles of NMR imaging. a) Spins rotating around the axis of the magnetic field direction with the Larmor frequency. b) An rf pulse tilt the magnetization from the Z-plane to the XY-plane. c) T_1 relaxation. d) T_2 relaxation. (Na et al., 2009)

This is a review of MRI technology. More information can be found in the literature by Elmaoğlu and Çelik (2011) and Lien (2004). In the investigations performed in this thesis the MRI was used for qualitative analyses of fluid saturations, fluid distribution and foam flow in fractured networks.

7.4.2 Imaging foam propagation in fractured networks

MRI experiments were performed at Statoil's laboratories at Sandsli, Bergen. The MR scanner had a magnetic field strength of 4.7 Tesla, and a frequency of 150 MHz.

Dynamic MRI of fractured marble core M2i-1

A dynamic MRI was performed, where gas (air) and surfactant solution were co-injected for foam generation in core plug M2i-1. Figure 31 presents a schematic of the experimental setup.

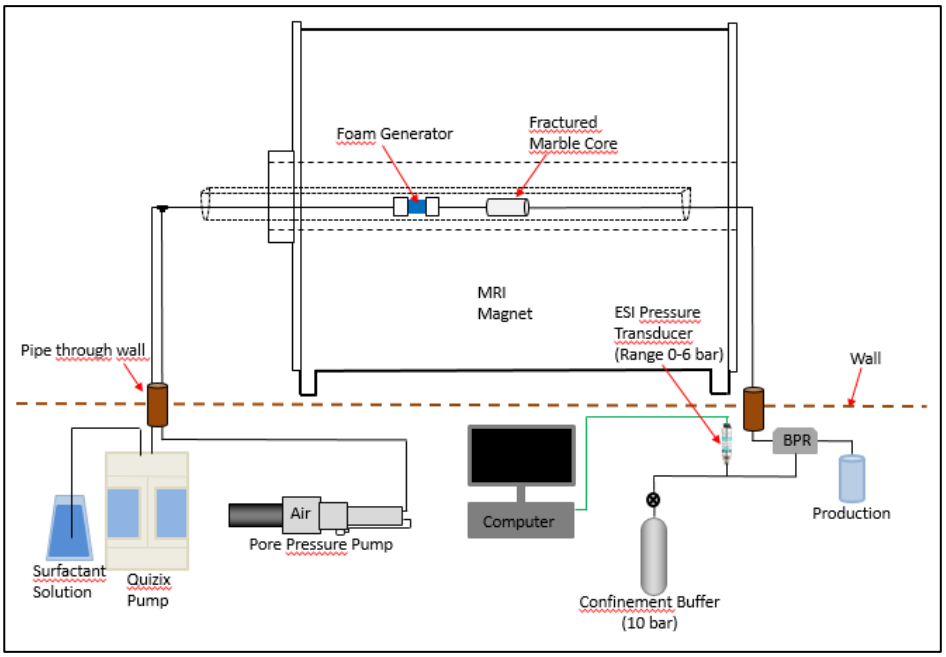

Figure 31 – Experimental setup for dynamic MRI of core M2i-1, at Statoil's laboratories at Sandsli, Bergen. The core was placed in the MR scanner, with a foam generator in front. The rest of the equipment was placed in another room to avoid interaction with the magnetic field, and was connected to the core and foam generator with nylon tubing lined up through two holes in the wall. A backpressure of 2 bar was applied with a backpressure regulator, adjusted with N_2 from a small N_2 buffer, and monitored with an ESI pressure transducer. (Illustration by collaboration partner Solveig Carlsen)

Foam was pre-generated in a foam generator that consisted of a 1.5" sandstone core of approximately 10 cm length. Two layers of epoxy was used to seal the core and mount it to end pieces, as shown in Figure 32. The foam generator was placed inside the MR scanner in front of the core plug, and could not contain any metal that would interact with the magnetic field.

Figure 32 – Foam generator used during dynamic MRI of foam injection in core M2i-1.

The injection pumps, the BPR and the ESI pressure transducer were placed in a room next to the MRI laboratory, and tubing was connected through holes in the wall between the two rooms. This was to avoid interaction between the metal equipment and the magnetic field of the MR scanner. Nylon tubing allowed direct observation of fluid flow, except inside the MR scanner. Backpressure was adjusted with a small N_2 tank with a pressure of approximately 10 bar. The

ESI pressure transducer was used to monitor the backpressure in case of leakage. The core plug was 100% saturated with brine before the experiment. Two pore volumes of surfactant solution were injected with rate 50 cc/h before the co-injection was started, to increase the system pressure to 2 bar. During co-injection, gas was injected with rate 35 cc/h, while surfactant solution was injected with rate 15 cc/h, to obtain a gas fraction of 0.7. The MR scanner was programmed to take images every minute throughout the foam injection.

Static MRI of fractured marble cores

Static MRI was performed on the fractured marble cores before and after baseline injections. The core plugs were placed in the MR scanner, and adjusted to suitable positions. Both 2D and 3D images were obtained. The MR scanner was controlled with a computer placed outside of the MR laboratory.

Part III – Results and Discussion

The following sections will provide a presentation and discussion of obtained results during investigations for this thesis. A total of 47 experiments were performed: 33 experiments with 2" fractured marble cores and 14 experiments with 2" Bentheimer sandstone cores (see Table 1 in section 5). Several experiments were conducted to optimize the conditions for foam stability. Pure gas injections were performed as baseline experiments to compare and evaluate the efficiency of foaming agents in brine displacement. Ultimately, 16 experiments of foam injections and pure gas injections were performed in optimized conditions, and these will be discussed here.

8 FRACTURED MARBLE CORES

Three fractured marble cores with different fracture systems were prepared for experiments. The cores were denoted M2i-1, M2i-2 and M2i-3, and the fracture systems are described in section 6.3.1. Routine core analysis was performed to determine fracture volume, porosity and permeability in each core plug, and the calculated parameters are listed in Table 5.

Table 5 – Measured and calculated properties for fractured marble cores. Uncertainties are calculated using uncertainty equations A6, A7 and A8, presented in Appendix B.

Core ID	**Length [cm] ± 0.01**	**Diameter [cm] ± 0.01**	**Pore Volume [cm^3] ± 0.01**	**Porosity [%] ± 0.04**	**Permeability [D]**
M2i-1	9.77	4.92	10.88	5.87	2.89 ± 0.03
M2i-2	9.67	4.96	8.68	4.66	8.03 ± 0.06
M2i-3	9.77	4.95	9.40	5.00	1.472 ± 0.001

Pure N_2 gas injections were performed as baseline experiments, for comparison with co-injection of N_2 gas and surfactant solution. MRI was conducted for qualitative analysis of the water saturations before and after pure gas injections, and during a co-injection of gas and surfactant solution. Fracture orientations during all experiments are illustrated in Figure 33.

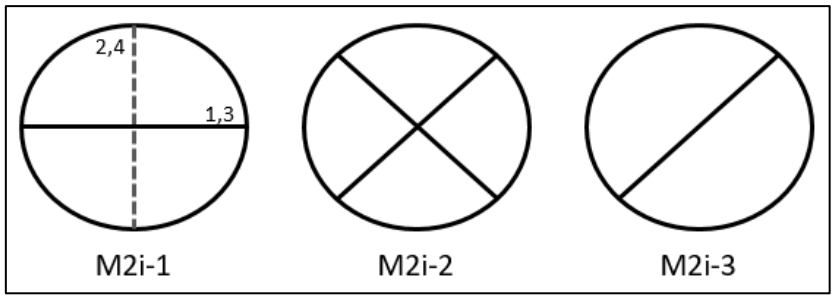

Figure 33 – Fracture orientations during experiments in fractured marble cores. Core M2i-1 was created with four fractured core pieces of equal length, where each core piece was oriented perpendicular to the previous core piece (numbers 1-4 indicate fracture orientation in core pieces 1-4).

8.1 N_2 GAS INJECTION IN FRACTURED MARBLE CORES

Pure N_2 gas injections were performed in each fracture system, in ambient pressure and temperature conditions. The core plugs were initially 100% saturated with brine. At least one pore volume of N_2 gas was injected with injection rate 50 cc/h. Calculated parameters of initial and irreducible water saturations, and maximum increase in pressure gradient during baseline injections are listed in Table 6. The pressure gradient is calculated as differential pressure per length of core plug.

Table 6 – Parameters of initial water saturation, S_{wi}, irreducible water saturation, $S_{wirr,g}$, and maximum increase in pressure gradient, ∇P_g, for pure gas injections with rate 50 cc/h, performed as baseline experiments in fractured marble cores M2i-1, M2i-2 and M2i-3 (two baseline experiments were performed in core M2i-3, denoted (1) and (2)).

Core ID	S_{wi} [%]	$S_{wirr,g}$ [%]	Increased ∇P_g (50cc/h) [mbar/m]
M2i-1	100	54.1	68.7
M2i-2	100	48.2	42.9
M2i-3 (1)	100	61.7	198.7
M2i-3 (2)	100	50.0	177.6

Water production and pressure gradients as functions of injected pore volumes are presented in Figures 34-36. Pressure gradient has been calculated as differential pressure per length of core plugs, and increased pressure gradient indicates higher differential pressure. Uncertainty calculations are based on uncertainties in equipment and are calculated using formulas presented in Appendix B. Matching trends were observed in cores M2i-1 and M2i-2, presented in respectively Figure 34 and Figure 35, with rapid increase in water production and early gas breakthrough. These cores have multi-fracture systems, as described in section 6.3.1, where M2i-1 have several minor fractures and M2i-2 have two perpendicular fractures, resulting in high permeability. N_2 breakthrough occurred after approximately 0.08 pore volumes injected

(PV injected) in core M2i-1, and 0.06 PV injected in core M2i-2. A decrease in the pressure gradient can be observed after breakthrough.

Two baseline injections were performed in core M2i-3, shown in Figure 36. This core plug had one single fracture. During both baseline injections, the water production stopped after approximately 0.18 PV injected in the first injection and 0.09 PV injected in the second injection. The pressure increased to a certain value before the production continued. This may indicate a narrow channel in the fracture which made a capillary barrier, so that a pressure increase was needed to overcome this threshold. The obstruction could be a natural narrowing in the fracture, or debris that has loosened from the rock due to interactions with brine. When the capillary threshold pressure was exceeded, the water production continued rapidly, and N_2 breakthrough followed at approximately 1.24 PV injected in the first baseline experiment and 1.21 PV injected in the second baseline experiment.

There was no further water production from any of the core plugs after gas breakthrough. Brine produced after breakthrough was brine that had stagnated in the outlet tubing due to pressure decrease.

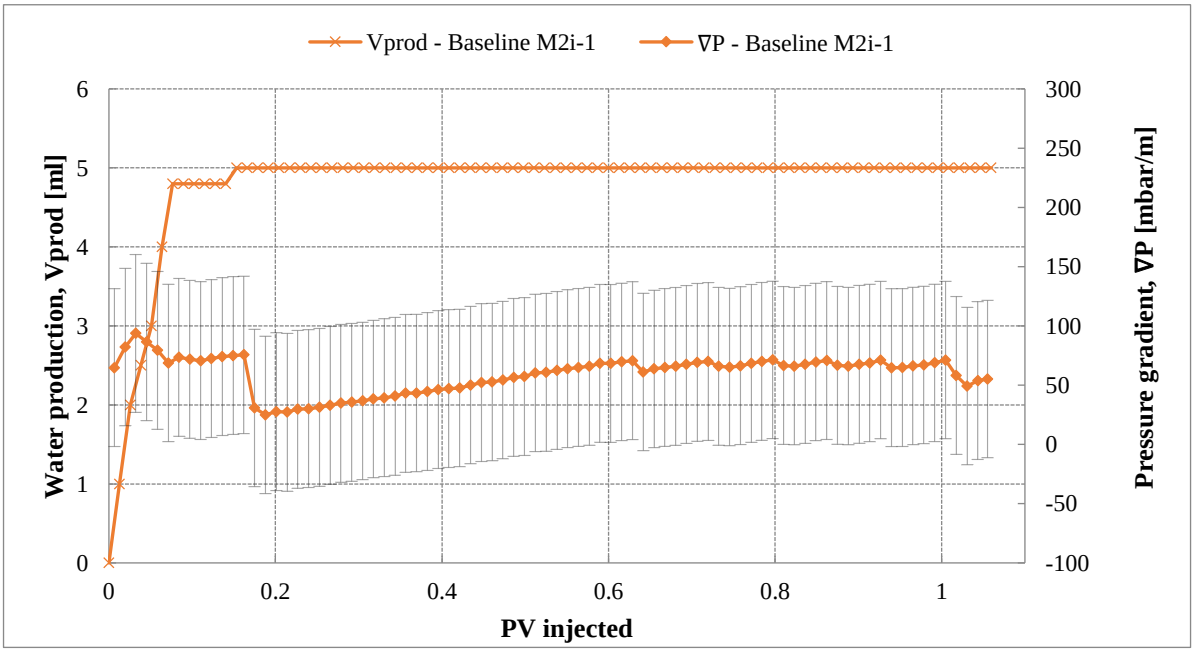

Figure 34 – Water production and pressure gradient during pure N_2 gas injection in fractured marble core M2i-1. The core was initially 100% saturated with brine. Gas was injected with injection rate 50 cc/h. Water production (left axis) was measured during the injection, while pressure gradient (right axis) has been calculated using measured inlet and outlet pressures. Error bars in pressure gradient are calculated based on uncertainty in ESI pressure transducers.

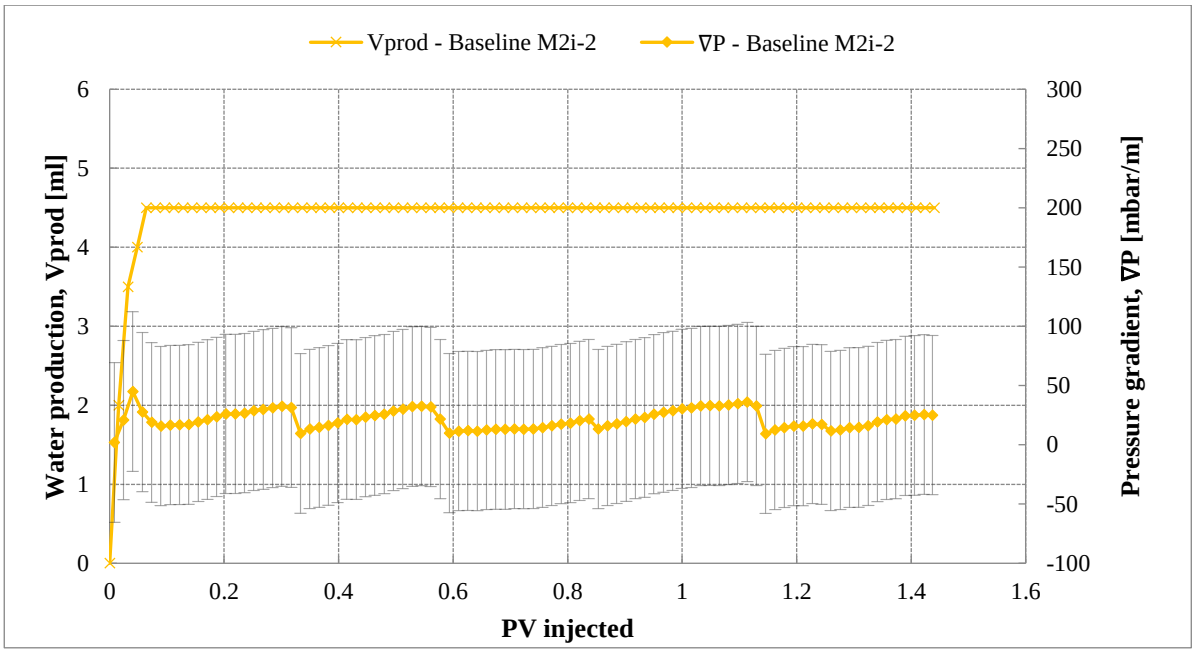

Figure 35 – Water production and pressure gradient during pure N_2 gas injection in fractured marble core M2i-2. The core was initially 100% saturated with brine. Gas was injected with injection rate 50 cc/h. Water production (left axis) was measured during the injection, while pressure gradient (right axis) has been calculated using measured inlet and outlet pressures. Error bars in pressure gradient are calculated based on uncertainty in ESI pressure transducers.

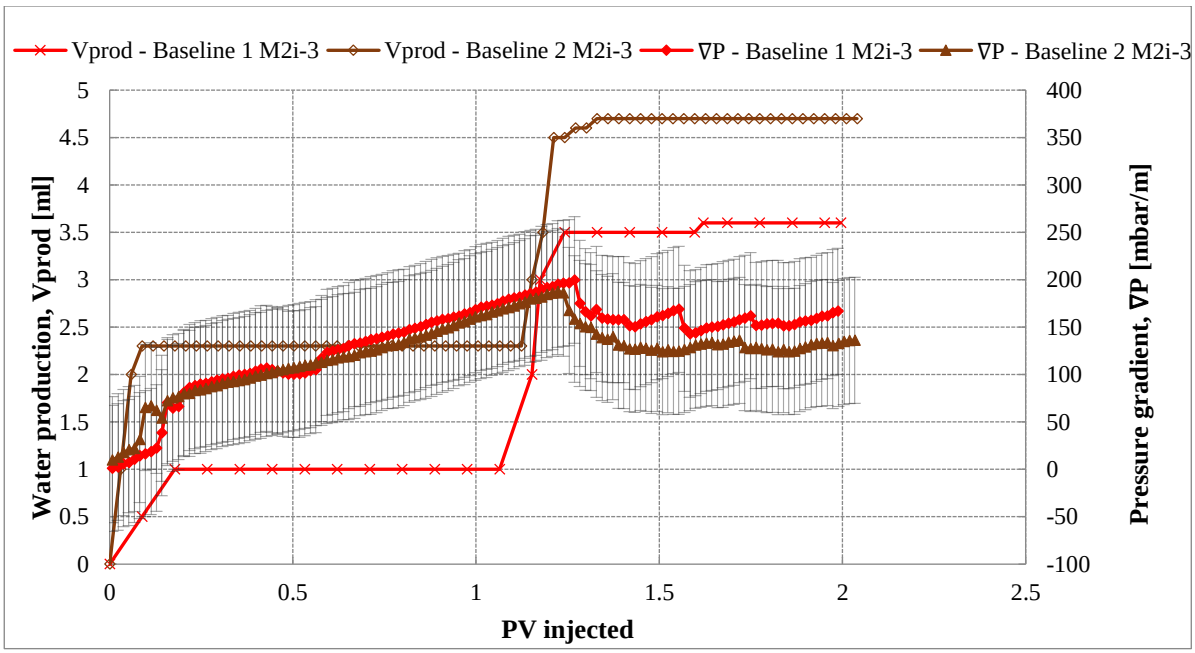

Figure 36 – Water production and pressure gradients during two pure N_2 gas injections in fractured marble core M2i-3. The core was initially 100% saturated with brine before both gas injections. Gas was injected with rate 50 cc/h. Water production (left axis) was measured during the injections, while pressure gradients (right axis) have been calculated using measured inlet and outlet pressures. Error bars in pressure gradients are calculated based on uncertainties in ESI pressure transducers.

8.2 FOAM INJECTIONS IN FRACTURED MARBLE CORES

Two co-injections with N_2 gas and surfactant solution were conducted in each of the fractured marble cores. Foam was pre-generated in a foam generator, placed in front of the core plugs. The co-injections were performed with total injection rate 50 cc/h and fractional gas flow of 0.7. The core plugs were initially 100% saturated with brine before the first co-injection, and 100% saturated with surfactant solution before the second co-injection. Two pore volumes of surfactant solution were injected in each core plug before all co-injections.

The pressure difference between the N_2 pump and the surfactant pump was adjusted to prevent backflow and obtain a stable gas fraction. A N_2 pump pressure of approximately 0.1 bar over system pressure was found to function well, and was applied in all experiments on fractured marble cores. It was observed that the gas flow rate and volume fraction of gas varied in the beginning of the different experiments, but for the most part stabilized after foam entered the core plugs. This was probably an effect of small variations between the N_2 pump pressure and the system pressure.

Inlet and outlet pressures were measured during the foam injections. Originally the calculated differential pressures across the core plugs were negative, even after correcting for offset between the ESI pressure transducers. To correct for this, the start point pressure was set to zero. This lifted the differential pressure to positive values. Negative differential pressure may be a result from errors in the original transducer offset calculations, or small pressure build-up compared to the range of the pressure transducers, which were 0-6.0 bar at the inlet and 0-2.5 bar at the outlet (corresponding to pressure gradients of around 0-62000 mbar/m and 0-25600 mbar/m). Uncertainties in pressure gradients are relatively large, as indicated in Figures 37-42. Uncertainty calculations are based on uncertainties in equipment and are calculated using formulas presented in Appendix B. Another possible cause of unreasonable pressure response is drift in the pressure transducers.

Water production and pressure gradients are plotted as functions of pore volumes injected in Figures 37-42. One pore volume of surfactant injection is included in the plots to emphasize the change in the pressure gradients when foam entered the core plugs. Time foam entered the core plugs (foam start) is calculated based on inlet dead volume in the system, and injection rate. Water production during the entire foam injection is plotted, although that includes surfactant solution from the dead volume in the outlet tubing (3.3 ml) and injected surfactant solution.

8.2.1 Multi-Fracture System in Core M2i-1

Core M2i-1 had a complex fracture system where eight core pieces were puzzled together as explained in section 6.3.1. The permeability of the core was 2.89 D and the pore volume was 10.88 ml. During the first foam injection, shown in Figure 37, foam breakthrough from the core plug was observed at 1.88 PV injected (0.88 PV injected after foam start). It was observed fluid flow from the core plug towards the injection pumps, or backflow, after foam breakthrough, but the flow direction changed at time 2.26 PV injected, and the water production continued. A total production of 6.13 ml was produced from the core plug during the first foam injection.

In the second foam injection, shown in Figure 38, the water production rate was lower, and breakthrough occurred at approximately 2.15 PV injected. 4.85 ml was produced from the core. An increase in the pressure gradient occurred at approximately 1.3 PV injected in each core.

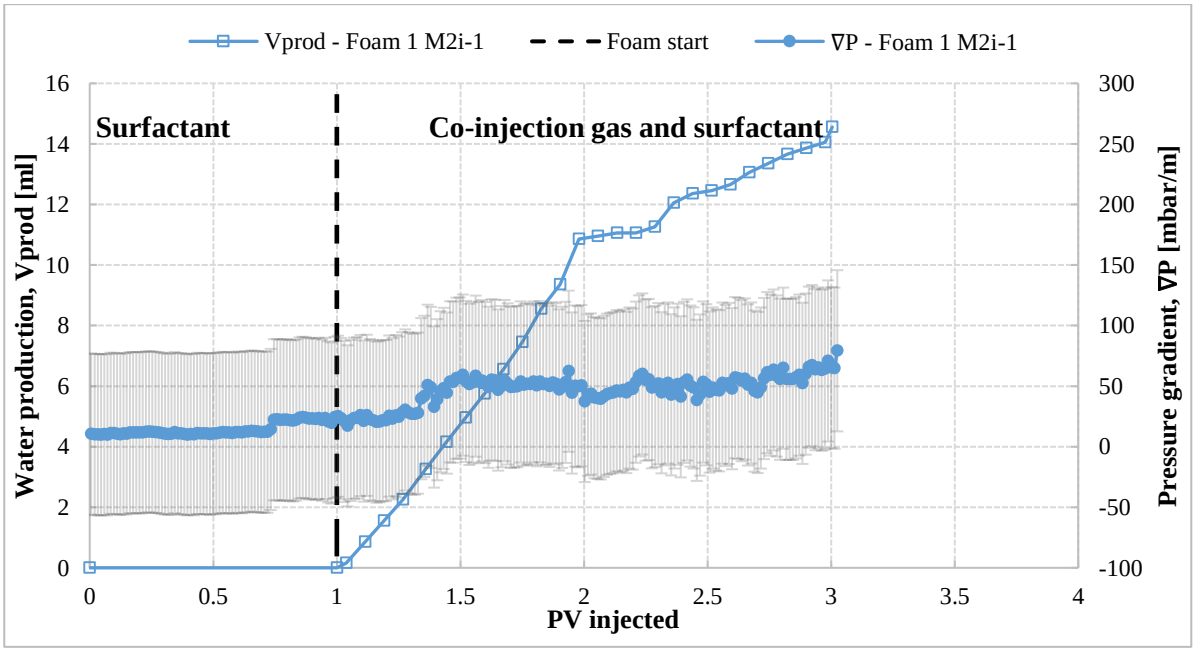

Figure 37 – Water production and pressure gradient during co-injection of N_2 gas and surfactant solution in fractured marble core M2i-1. The core was initially 100% saturated with brine. One pore volume of surfactant solution injection is included in the plot. Two pore volumes were injected during co-injection, with gas fraction 0.7 and total injection rate 50 cc/h. Start of co-injection is indicated with the black, dashed vertical line. Water production (left axis) was measured during the injection. The water production originating from the core plug was estimated to 6.13 ml. The pressure gradient (right axis) has been calculated using measured differential pressures. Error bars in pressure gradients are calculated based on uncertainties in ESI pressure transducers.

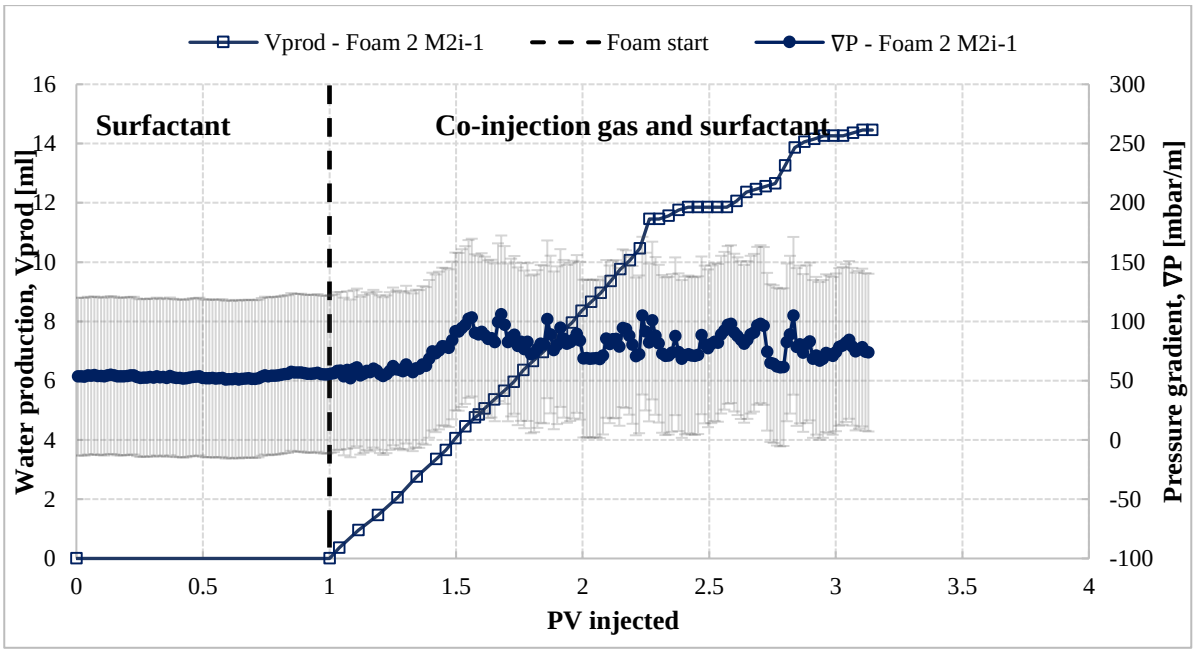

Figure 38 – Water production and pressure gradient during a second co-injection of N_2 gas and surfactant solution in fractured marble core M2i-1. The core was initially 100% saturated with surfactant solution. One pore volume of surfactant solution injection is included in the plot. Two pore volumes were injected during co-injection, with gas fraction 0.7 and total injection rate 50 cc/h. Start of co-injection is indicated with the black, dashed vertical line. Water production (left axis) was measured during the injection. The water production originating from the core plug was estimated to 4.85 ml. The pressure gradient (right axis) has been calculated using measured differential pressures. Error bars in pressure gradients are calculated based on uncertainties in ESI pressure transducers.

8.2.2 Simple Multi-Fracture System in Core M2i-2

Core M2i-2 had two perpendicular fractures across the core length, a pore volume of 8.68 ml and a high permeability of 8.03 D. During the first co-injection, shown in Figure 39, it was observed small gas intervals relative to surfactant in the beginning of the experiment, causing unstable foam and a slow water production rate. The BPR let through fluids at certain intervals, and during these intervals a higher amount of gas relative to surfactant entered the foam generator. A pressure build-up and increased water production rate occurred around 2 PV injected. Breakthrough was observed at 2.38 PV injected, and the total water production from the core was 2.65 ml.

In the second foam injection, a pressure build-up peaked at 1.50 PV injected, which can be seen in Figure 40. Breakthrough occurred after 1.92 injected pore volumes, and the water production rate declined from that point on. A total of 1.88 ml was produced from the core.

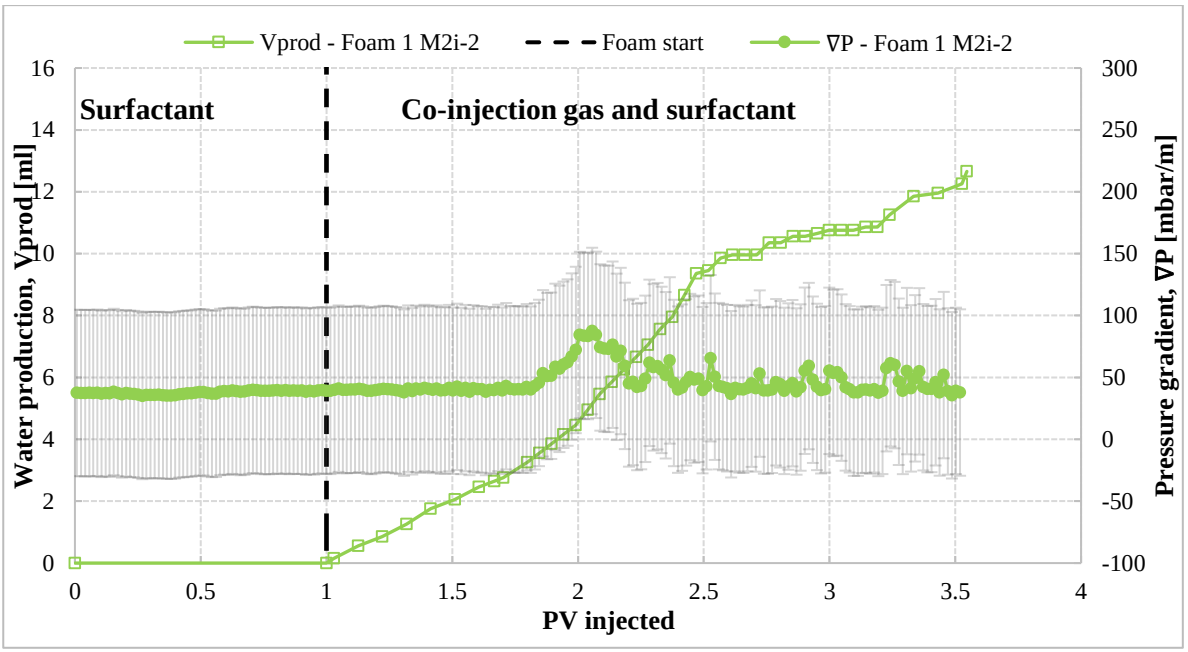

Figure 39 – Water production and pressure gradient during co-injection of N_2 gas and surfactant solution in fractured marble core M2i-2. The core was initially 100% saturated with brine. One pore volume of surfactant solution injection is included in the plot. Two pore volumes were injected during co-injection, with gas fraction 0.7 and total injection rate 50 cc/h. Start of co-injection is indicated with the black, dashed vertical line. Water production (left axis) was measured during the injection. The water production originating from the core plug was estimated to 2.65 ml. The pressure gradient (right axis) has been calculated using measured differential pressures. Error bars in pressure gradients are calculated based on uncertainties in ESI pressure transducers.

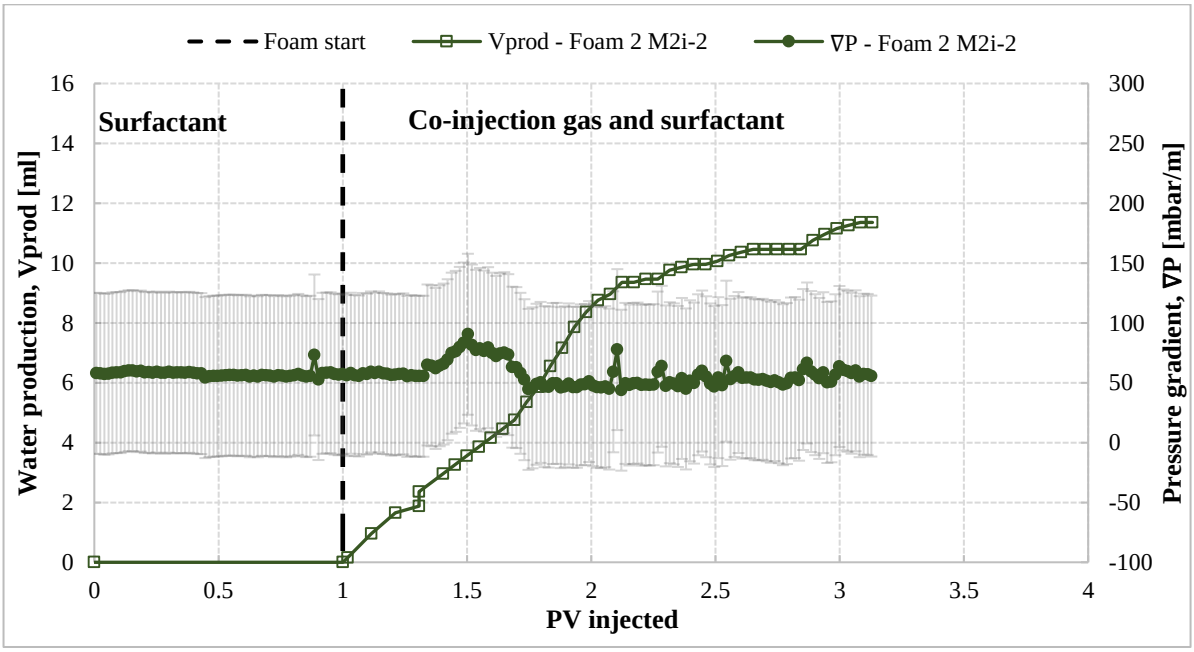

Figure 40 – Water production and pressure gradient during a second co-injection of N_2 gas and surfactant solution in fractured marble core M2i-2. The core was initially 100% saturated with surfactant solution. One pore volume of surfactant solution injection is included in the plot. Two pore volumes were injected during co-injection, with gas fraction 0.7 and total injection rate 50 cc/h. Start of co-injection is indicated with the black, dashed vertical line. Water production (left axis) was measured during the injection. The water production originating from the core plug was estimated to 1.88 ml. The pressure gradient (right axis) has been calculated using measured differential pressures. Error bars in pressure gradients are calculated based on uncertainties in ESI pressure transducers.

8.2.3 Single-Fracture System in Core M2i-3

One single fracture was generated in core M2i-3, and corresponded to a pore volume of 9.40 ml. The core had a permeability of 1.472 D. 4.60 ml was produced from the core in the first co-injection, shown in Figure 41. Breakthrough occurred at 2.64 PV injected. A significant increase in pressure gradient can be observed around 2 PV injected. Before gas entered the foam generator, the relative amount of gas to surfactant solution seemed to be approximately 0.6-0.7.

5.63 ml was produced in the second injection, shown in Figure 42. Observed breakthrough at the core outlet was at 1.58 PV injected. An earlier pressure increase was seen during this injection, increasing already during the surfactant injection, followed by a relatively stable interval. The pressure gradient increased again at 1.15 PV injected, peaking at 1.30 PV injected. The relatively sharp pressure increase can indicate stable foam, and it was also visually observed longer intervals of foam during this injection than in the other foam injections in fractured marble cores.

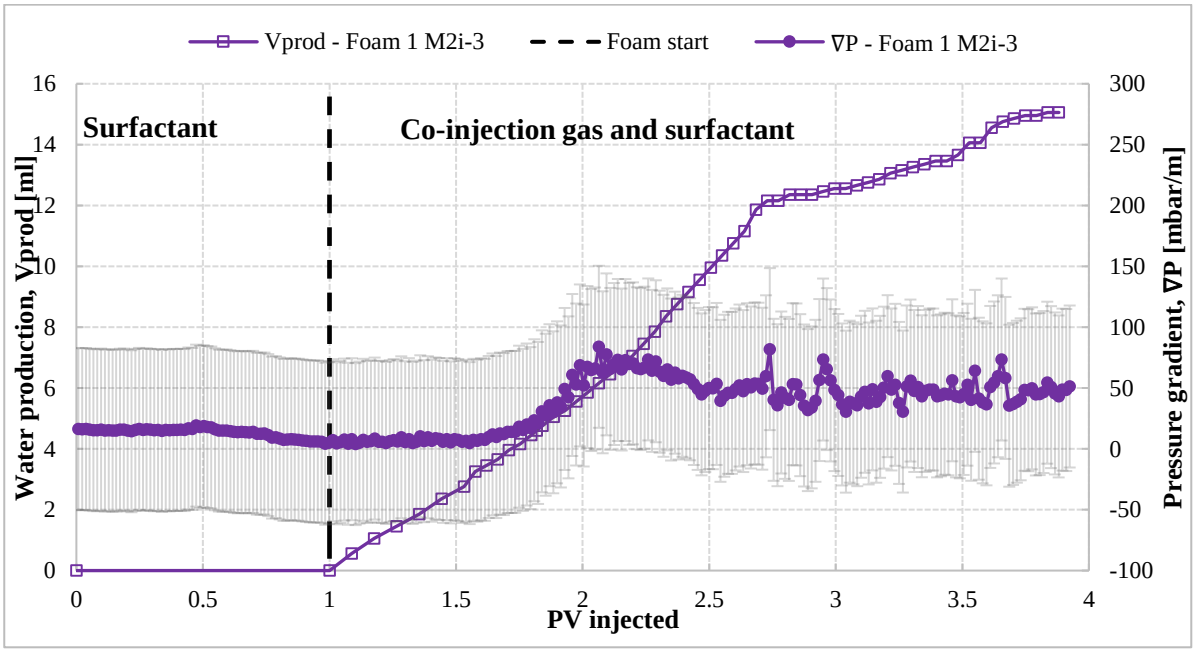

Figure 41 – Water production and pressure gradient during co-injection of N_2 gas and surfactant solution in fractured marble core M2i-3. The core was initially 100% saturated with brine. One pore volume of surfactant solution injection is included in the plot. Two pore volumes were injected during co-injection, with gas fraction 0.7 and total injection rate 50 cc/h. Start of co-injection is indicated with the black, dashed vertical line. Water production (left axis) was measured during the injection. The water production originating from the core plug was estimated to 4.60 ml. The pressure gradient (right axis) has been calculated using measured differential pressures. Error bars in pressure gradients are calculated based on uncertainties in ESI pressure transducers.

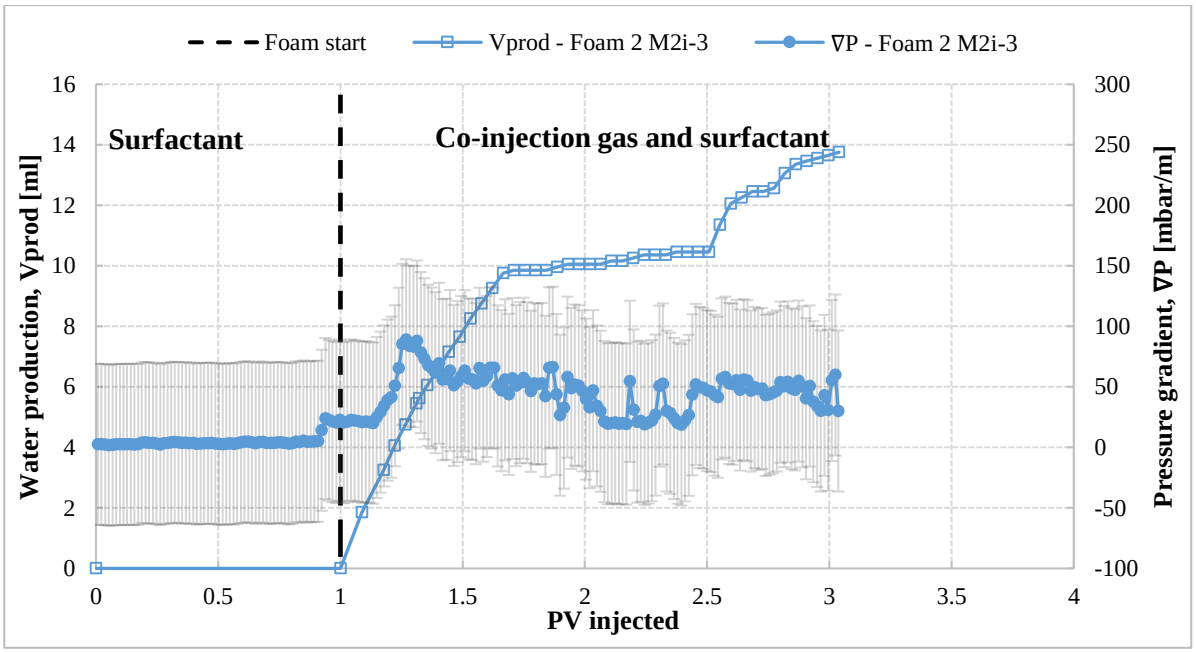

Figure 42 – Water production and pressure gradient during a second co-injection of N_2 gas and surfactant solution in fractured marble core M2i-3. The core was initially 100% saturated with surfactant solution. One pore volume of surfactant solution injection is included in the plot. Two pore volumes were injected during co-injection, with gas fraction 0.7 and total injection rate 50 cc/h. Start of co-injection is indicated with the black, dashed vertical line. Water production (left axis) was measured during the injection. The water production originating from the core plug was estimated to 5.63 ml. The pressure gradient (right axis) has been calculated using measured differential pressures. Error bars in pressure gradients are calculated based on uncertainties in ESI pressure transducers.

8.2.4 The Effect of Foam on Displacement Efficiency in Fractured Marble Cores

Measurements of water production and differential pressure were used to compare endpoint water saturations and mobility reduction in the different fracture systems. Endpoint water saturations, S_{wirr}, were calculated based on the water production originating from the core plugs. Estimated production from the core plugs was based on material balance. The production originating from the core plugs was equal to the total production measured during experiments, subtracting the volume of surfactant solution injected during the measuring interval, and the liquid volume initially present in the inlet and outlet dead volumes. The volume of remaining liquid in the inlet and outlet dead volumes after injection were considered by subtracting it from the injected volume of surfactant solution. The pressure gradients were calculated as the differential pressure per length of core plugs, while the mobility reduction factors were calculated using equation (4). For core M2i-3, an average increase in pressure gradient from the two baseline experiments was used for calculations. Calculated parameters are listed in Table 7.

Table 7 – Parameters of initial water saturation, S_{wi}, irreducible water saturation after foam injection, $S_{wirr,f}$, maximum increase in pressure gradient, ∇P_f, and mobility reduction factor, MRF, for co-injections of gas and surfactant in fractured marble cores M2i-1, M2i-2 and M2i-3 (two co-injections were performed in each core, denoted (1) and (2)).

Core ID	S_{wi}	$S_{wirr,f}$	Increased ∇P_f (50 cc/h)	MRF
	[%]	[%]	[mbar/m]	
M2i-1 (1)	100	43.65	69.49	1.01
M2i-1 (2)	100	55.42	55.09	0.80
M2i-2 (1)	100	69.52	52.52	1.22
M2i-2 (2)	100	78.35	46.74	1.09
M2i-3 (1)	100	51.08	79.97	0.43
M2i-3 (2)	100	40.12	87.22	0.46

Average endpoint water saturation after foam injections in core M2i-1 was 49.54%, an improvement of 4.51% relative to the endpoint water saturation after pure gas injection. Average endpoint water saturation in core M2i-2 did not improve during foam injection, and an average increase of 25.79% compared to pure gas injection was obtained. An improvement of 10.24% was achieved in core M2i-3 after foam injections compared to pure gas injections, but if the first baseline injection is neglected (due to high endpoint water saturation compared to the second baseline injection), the improvement was only 4.38%.

The mobility reduction factors show little or no reduction in gas mobility. The increase in pressure gradient in core M2i-3 was significantly larger in baseline injections than in foam injections. This was most likely caused by loose rock particles in the fracture, that probably were removed during re-saturation or surfactant flooding before foam injections.

The low water recovery indicates poor volumetric sweep, and the low mobility reduction factor does not indicate stable foam. Small improvements in displacement efficiency, and hence storage potential, indicate that there is little effect of foam in core samples with pore volumes of this scale (8.6-10.9 ml), with high permeability.

It seems that the high fracture volume and permeability in core M2i-2, which had two perpendicular fractures, caused flow of foam primarily in certain parts of the fracture network. MRI after pure gas injection indicated this flow behavior during baseline experiments, as seen in Figure 44. Core sample M2i-1 consisted of four single-fracture core pieces, and core M2i-3 had one single fracture across the whole core length, restricting the number of flow paths compared to core M2i-2. This appear to have resulted in a higher volumetric sweep in cores M2i-1 and M2i-3, than in core M2i-2.

Variations in pressure gradient and water production were relatively consistent in each core plug during the two foam injections. Increase in pressure gradient varied with 14.4 mbar/m at the most, in core M2i-1. Endpoint water saturations varied accordingly, where a larger increase in pressure gradient corresponded to a lower endpoint saturation. Significant variations in water production rates between the first and the second foam injections were observed in all core samples. This is most prominent in core M2i-3, where the final foam injection was identified with rapid increase in pressure gradient and early gas breakthrough, compared to a slower pressure buildup and water production rate during the first foam injection. Increased recovery rate can indicate formation of stable foam (Fernø et al., 2015). Variations in displacement characteristics between foam injections in the same core plugs can be an effect of inconsistent fractional flow of gas due to pressure variations, variations in foam stability, hysteresis, or experimental uncertainty factors that are discussed in section 10.

It was observed during foam experiments that the foam quality varied during experiments. It was also observed varying degree of persistent foam between the foam generator and the core plugs. Best foam stability was observed for apparent foam qualities of 0.7 or higher.

8.3 Magnetic Resonance Imaging of Foam Flow in Fractures

8.3.1 MRI of Fractured Marble Cores

MRI was done on fractured marble cores M2i-1, M2i-2 and M2i-3, when the cores were 100% saturated with brine and after N_2 gas injections. Images are shown in Figures 43-45. White parts of the images indicate brine, and it is clear in all core plugs that the water saturation decreased significantly after gas injections. The 3D image of core M2i-2 after gas injection indicate better sweep in the right part of the fracture network, than in the left part of the fracture network, which is probably a consequence of gas favoring the path with least resistance to gas flow.

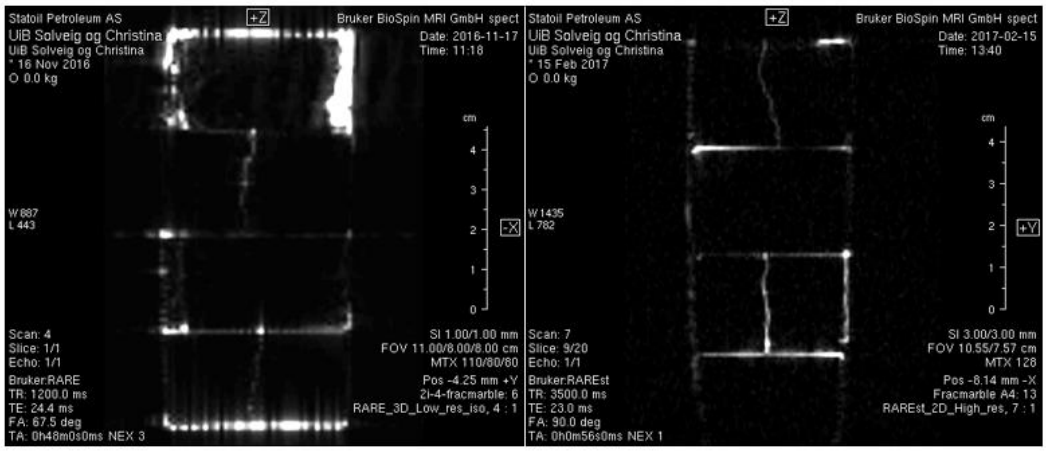

Figure 43 – MRI of core M2i-1, 100% saturated with brine to the left, in 3D, and after N_2 gas injection to the right, in 2D.

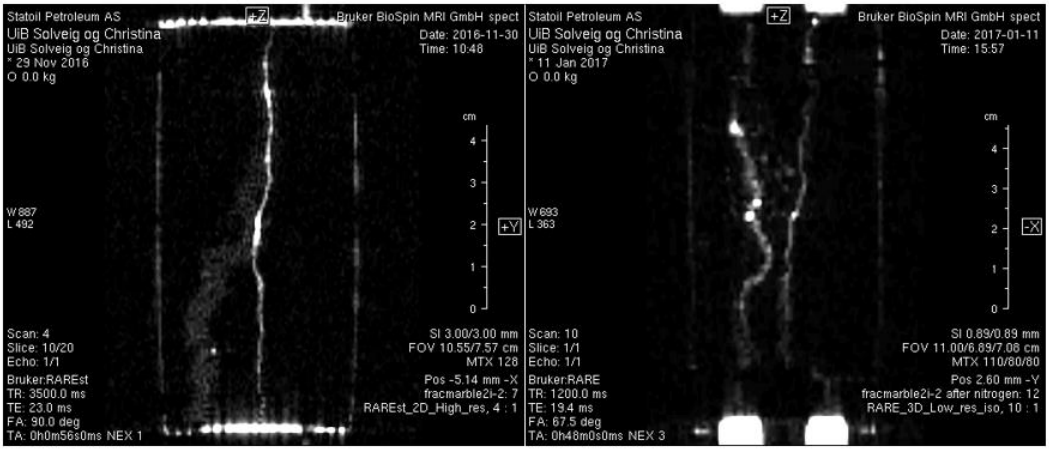

Figure 44 – MRI of core M2i-2, 100% saturated with brine to the left, in 2D, and after N2 gas injection to the right, in 3D.

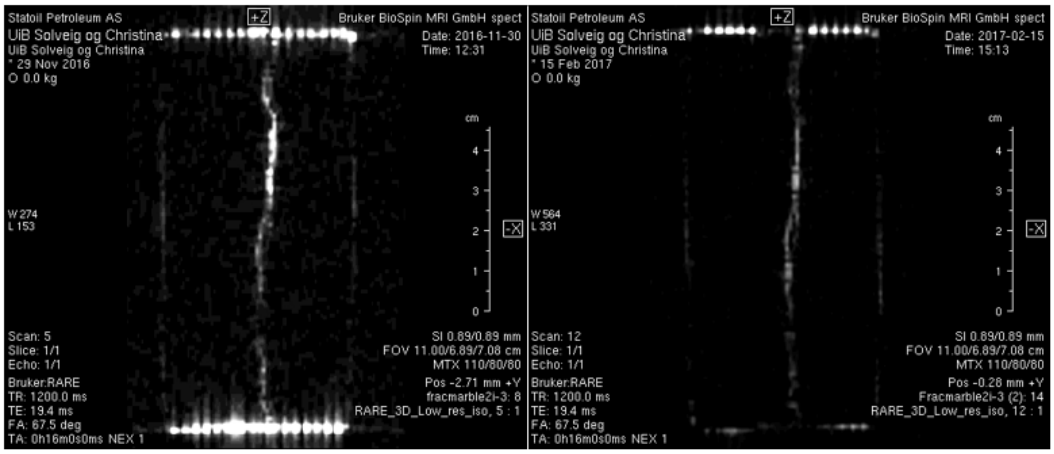

Figure 45 – MRI of core M2i-3, 100% saturated with brine to the left, in 3D, and after N_2 gas injection to the right, in 3D.

8.4 DYNAMIC MRI OF FRACTURED MARBLE CORE M2I-1

A dynamic 2D MRI of foam injection in core M2i-1 was performed by co-injecting gas and surfactant solution with a rate of 50 cc/h, with a backpressure of 2 bar. There was some leakage in the gas pump causing the pressure in the pump to sink below the system pressure, which resulted in backflow. The injection was stopped and the pump pressure was increased to 1 bar over atmospheric pressure again, before the experiment continued. This occurred twice, but after the second time, the injection rate was increased to a rate of 600 cc/h, to maintain a steady flow throughout the experiment. 2D images were taken throughout the entire injection with 1 minute intervals, and a representative sample is shown in Figure 46. Foam was observed to hit the core shortly after restarting the injection after the first backflow, around 11:30. Breakthrough was observed when the injection was restarted after the second backflow, around 11:50. A significant decrease in water saturation can be observed during the foam injection.

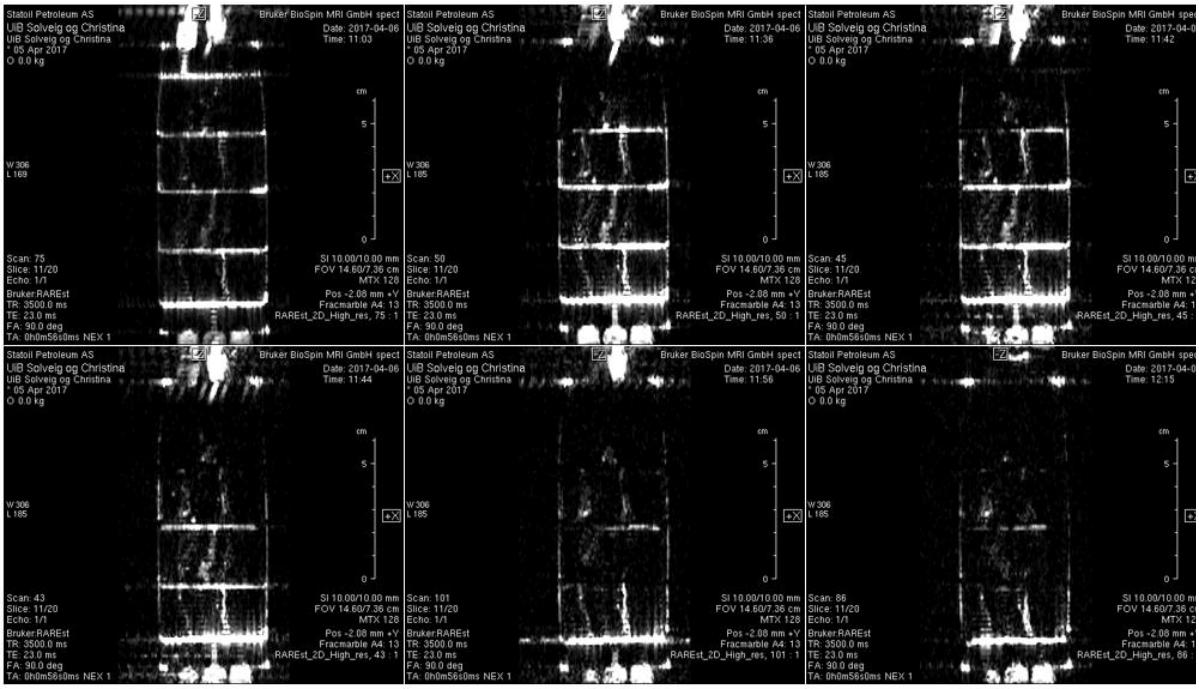

Figure 46 – Dynamic 2D MRI of co-injection of gas and surfactant solution in core M2i-1. The time each image was taken is found in the upper right corner of the image. The white parts of the images represent liquid. The core consists of four, fractured cylindrical pieces, but parts of the core end pieces and Swagelok fittings are also visible in each end of the core. Direction of flow was from top to bottom in the images.

9 BENTHEIMER SANDSTONE CORES

Six Bentheimer sandstone cores denoted S2i-7, S2i-9, S2i-10, S2i-11, S2i-12 and S2i-13 were used for experiments in unfractured porous media. Routine core analysis was conducted to determine the pore volume, porosity and permeability in each core sample, and the calculated parameters are presented in Table 8.

Table 8 – Measured and calculated properties for unfractured sandstone cores. Uncertainties are calculated using uncertainty equations A6, A7 and A8, presented in Appendix B.

Core ID	Length [cm] ± 0.01	Diameter [cm] ± 0.01	Pore Volume [cm^3] ± 0.01	Porosity [%] ± 0.2	Permeability [D]
S2i-7	9.80	5.16	45.38	22.1	3.22 ± 0.02
S2i-8	9.95	5.17	48.02	23.0	2.622 ± 0.005
S2i-9	10.10	5.17	48.21	22.8	1.84 ± 0.02
S2i-10	10.01	5.17	48.61	23.1	1.71 ± 0.01
S2i-11	9.94	5.17	47.45	22.7	2.355 ± 0.002
S2i-12	9.99	5.17	47.55	22.7	1.7606 ± 0.0005
S2i-13	9.96	5.17	47.45	22.7	1.78 ± 0.02

Pure CO_2 gas injections were performed as baseline experiments in two core plugs, while foam was generated by co-injecting CO_2 gas and surfactant solution in four core plugs. Resistivity measurements were conducted during all experiments.

9.1 CO_2 GAS INJECTIONS IN BENTHEIMER SANDSTONE CORES

Pure CO_2 gas was injected for baseline studies in 100% brine saturated sandstone cores. A backpressure of 10 bar was applied. Gas was injected with injection rate 50 cc/h. Measured water production was used to calculate water saturation based on material balance, and measured resistivity was used to calculate water saturation using Archie's second law (equation (8)). Pressure gradients were calculated as differential pressure per length of core plugs. Calculated statistics are presented in Table 9.

Table 9 – Parameters of initial water saturation, S_{wi}, irreducible water saturation after gas injection, $S_{wirr,g,prod}$, minimum water saturation based on resistance, $S_{wmin,g,res}$, and maximum increase in pressure gradient, ∇P_g, for pure gas injections with rate 50 cc/h, performed as baseline experiments in sandstone cores S2i-10 and S2i-11.

Core ID	S_{wi}	$S_{wirr,g,prod}$	$S_{wmin,g,res}$	Increased ∇P_g (50 cc/h)
	[%]	[%]	[%]	[mbar/m]
S2i-10	100	76.17	65.04	1200.80
S2i-11	100	72.21	71.18	1442.76

Water saturations and pressure gradients are plotted as functions of injected pore volumes in Figure 47 and Figure 48. The experimental system was filled with brine before the gas injections, and resulting dead volumes were considered in production analysis and subtracted from the calculated water saturations. Hence, the endpoint saturations in Figure 47 and Figure 48 are accurate, but the variation with time is inaccurate because it was assumed constant water production from the core plugs, and no further water production after gas breakthrough.

Changes in the pressure gradient indicate gas breakthrough in the core plugs after approximately 0.40-0.45 PV injected in both cores S2i-10 and S2i-11. This correlate well with observed gas breakthrough in the approximately 6.2 cm long outlet tubing, which was at 0.58 PV injected in core S2i-10, and 0.55 PV injected in core S2i-11. Following decrease in water saturation based on resistivity, along with spikes in the pressure gradient, indicate further water production from the core plugs after gas breakthrough. Throughout the gas injections, the resistivity decreased at some points, indicating *increase* in water saturation. Since only gas was injected, the water (or liquid) saturation is not likely to increase. This may have been caused by redistribution of liquid in the core plugs, which can affect the connectivity in the water, and thus the electrical conductivity.

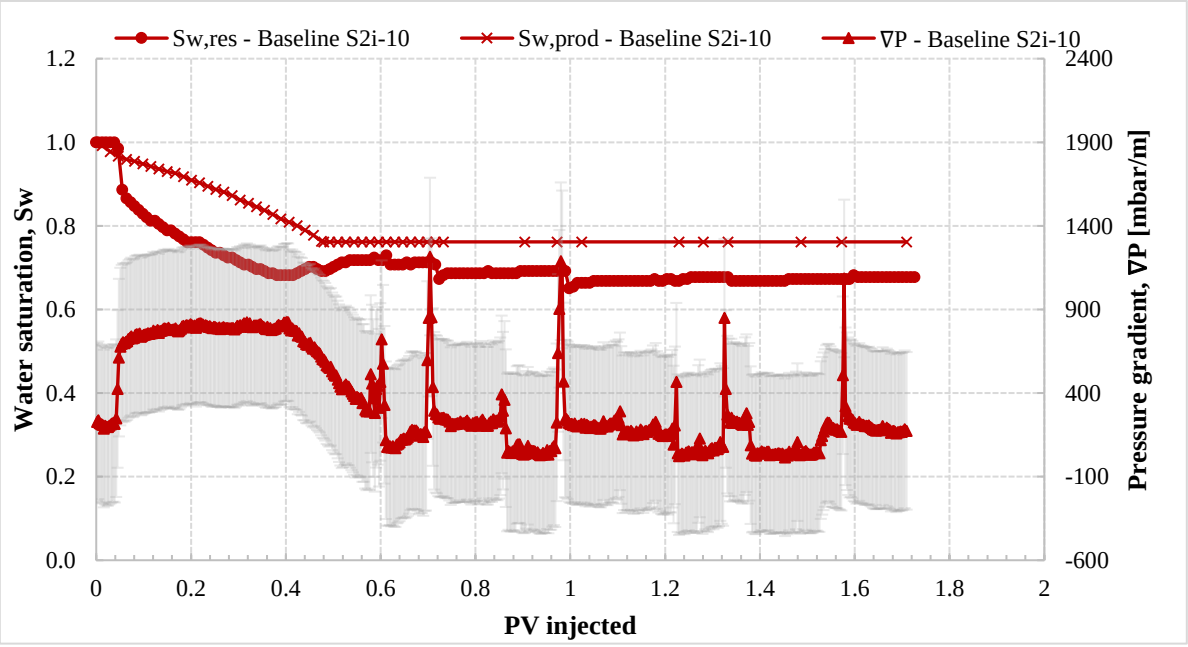

Figure 47 – Water saturation and pressure gradient during pure CO_2 gas injection in sandstone core S2i-10. The core was initially 100% saturated with brine. Gas was injected with injection rate 50 cc/h. Water saturations (left axis) were based on resistivity measurements and water production during the injection, while the pressure gradient (right axis) has been calculated using measured differential pressure. Error bars in the pressure gradient are calculated based on uncertainty in ESI pressure transducers.

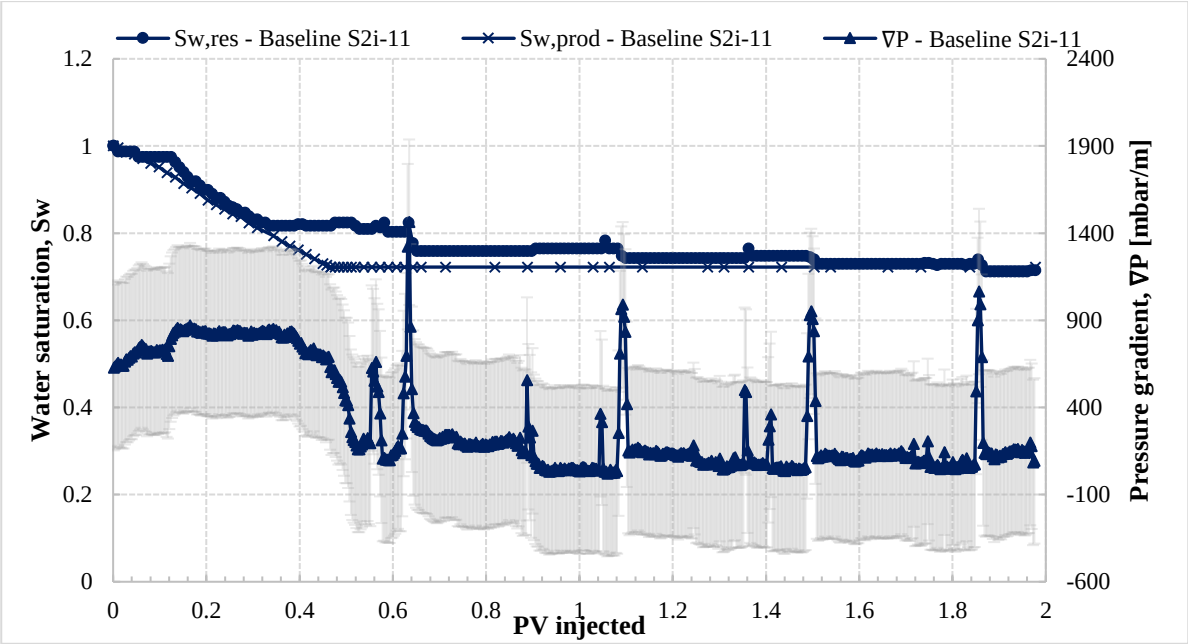

Figure 48 – Water saturation and pressure gradient during pure CO_2 gas injection in sandstone core S2i-11. The core was initially 100% saturated with brine. Gas was injected with injection rate 50 cc/h. Water saturations (left axis) were based on resistivity measurements and water production during the injection, while the pressure gradient (right axis) has been calculated using measured differential pressure. Error bars in the pressure gradient are calculated based on uncertainty in ESI pressure transducers.

9.2 Foam Flow Behavior in Bentheimer Sandstone Cores

Foam injections in sandstone cores were performed by co-injecting CO_2 gas and surfactant solution with a total injection rate of 50 cc/h. The core plugs were initially 100% saturated with brine, but two pore volumes of surfactant solution were injected prior to the co-injection. Foam was pre-generated in a foam generator located close to the core holder inlet. Measurements of water production, electrical resistance and inlet and outlet pressures during the co-injections have been evaluated.

Results from four foam injections are presented in Figures 49-52. One pore volume of surfactant solution injection is shown before the foam injection, to emphasize the variation in pressure gradient between pure gas injection and foam injection. Time foam entered the core plugs (foam start) was calculated based on inlet dead volume in the system, and injection rate. Water saturations calculated by water production measurements are not accurate relative to time, because the dead volume in the outlet tubing and the injected volume of surfactant solution have been subtracted from the total water production, assuming constant water production from the core plugs, and no further water production after gas breakthrough.

Uncertainties in the pressure gradients are calculated based on the uncertainties in the ESI pressure transducers, using formulas presented in Appendix B. A sharp and relatively large increase in pressure gradient, followed by fluctuations around a certain interval, is observed at the start of foam injection in core S2i-12, shown in Figure 51. The sudden increase in pressure gradient can indicate stable foam (Kam and Rossen, 2003). A smaller pressure increase is also observed in cores S2i-7, Figure 49, and S2i-9, Figure 50, before stabilizing around a certain interval. In core S2i-13, Figure 52, the pressure gradient increased more steadily during the entire foam injection, before it ceased at approximately 3.2 PV injected, when the resistivity stops decreasing. This indicates a slow displacement with late breakthrough.

It was not possible to define a time of foam breakthrough in the outlet tubing, since pure surfactant solution would be produced if either foam was not generated, or if the foam was broken down before reaching the end of the tubing. However, foam was observed as production at some point in all the experiments.

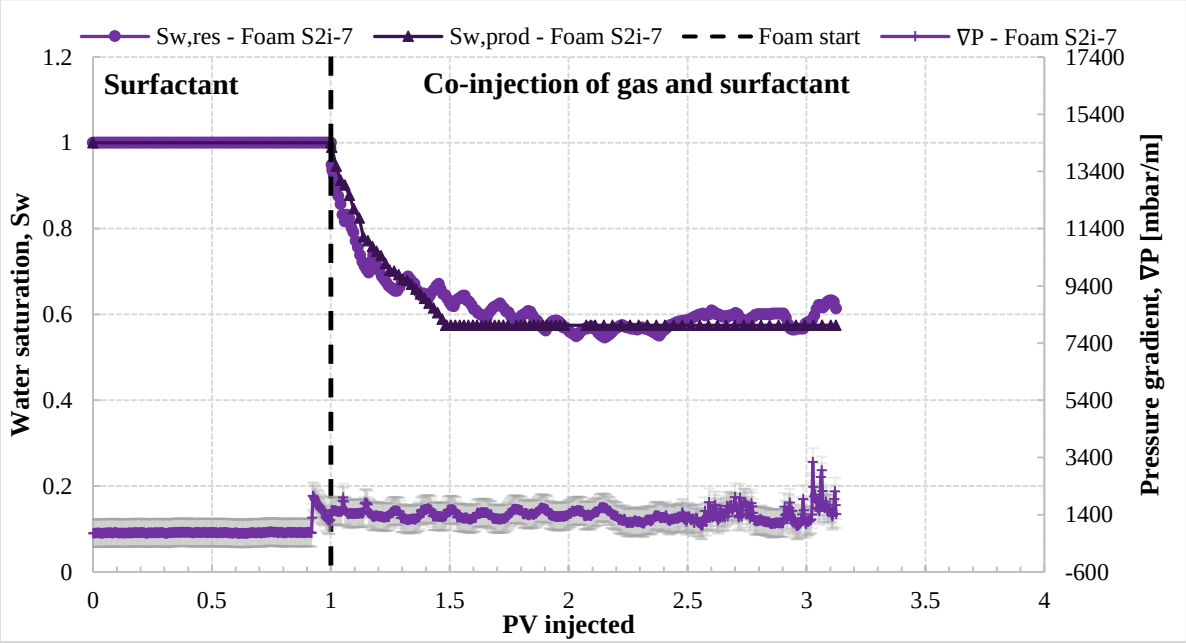

Figure 49 – Water saturation and pressure gradient during co-injection of CO_2 gas and surfactant solution in sandstone core S2i-7. The core was initially 100% saturated with brine, but was flushed with two pore volumes of surfactant solution before foam injection. One pore volume of surfactant solution injection is included in the plot. Two pore volumes were injected during co-injection, with gas fraction 0.7 and injection rate 50 cc/h. Start of co-injection is indicated with the black, dashed vertical line. Water saturations (left axis) were calculated using resistivity and Archie's second law, and water production measurements conducted during the injection, while pressure gradient (right axis) is based on measured differential pressures. Error bars in pressure gradients are calculated based on uncertainties in ESI pressure transducers.

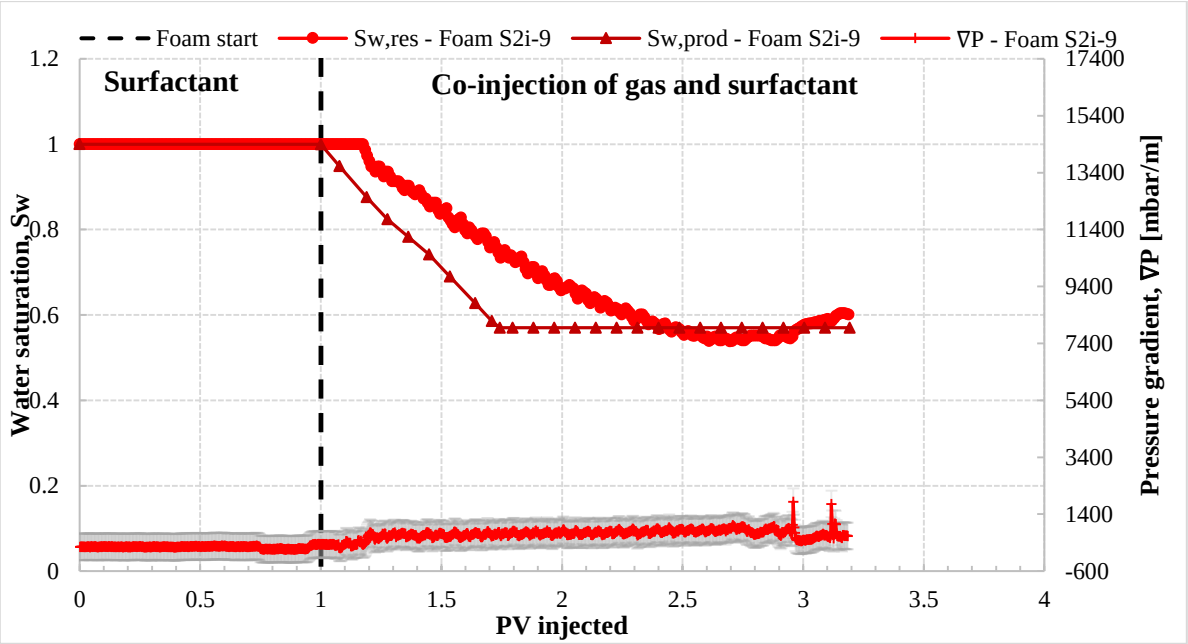

Figure 50 – Water saturation and pressure gradient during co-injection of CO_2 gas and surfactant solution in sandstone core S2i-9. The core was initially 100% saturated with brine, but was flushed with two pore volumes of surfactant solution before foam injection. One pore volume of surfactant solution injection is included in the plot. Two pore volumes were injected during co-injection, with gas fraction 0.7 and injection rate 50 cc/h. Start of co-injection is indicated with the black, dashed vertical line. Water saturations (left axis) were calculated using resistivity and Archie's second law, and water production measurements conducted during the injection, while pressure gradient (right axis) is based on measured differential pressures. Error bars in pressure gradients are calculated based on uncertainties in ESI pressure transducers.

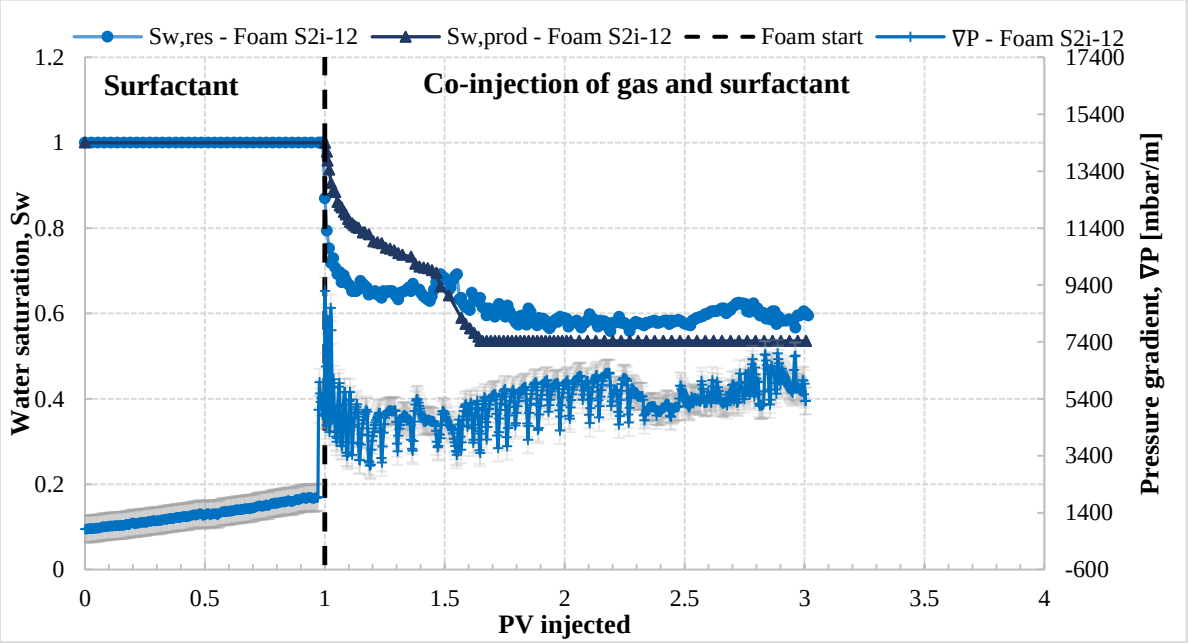

Figure 51 – Water saturation and pressure gradient during co-injection of CO_2 gas and surfactant solution in sandstone core S2i-12. The core was initially 100% saturated with brine, but was flushed with two pore volumes of surfactant solution before foam injection. One pore volume of surfactant solution injection is included in the plot. Two pore volumes were injected during co-injection, with gas fraction 0.7 and injection rate 50 cc/h. Start of co-injection is indicated with the black, dashed vertical line. Water saturations (left axis) were calculated using resistivity and Archie's second law, and water production measurements conducted during the injection, while pressure gradient (right axis) is based on measured differential pressures. Error bars in pressure gradients are calculated based on uncertainties in ESI pressure transducers.

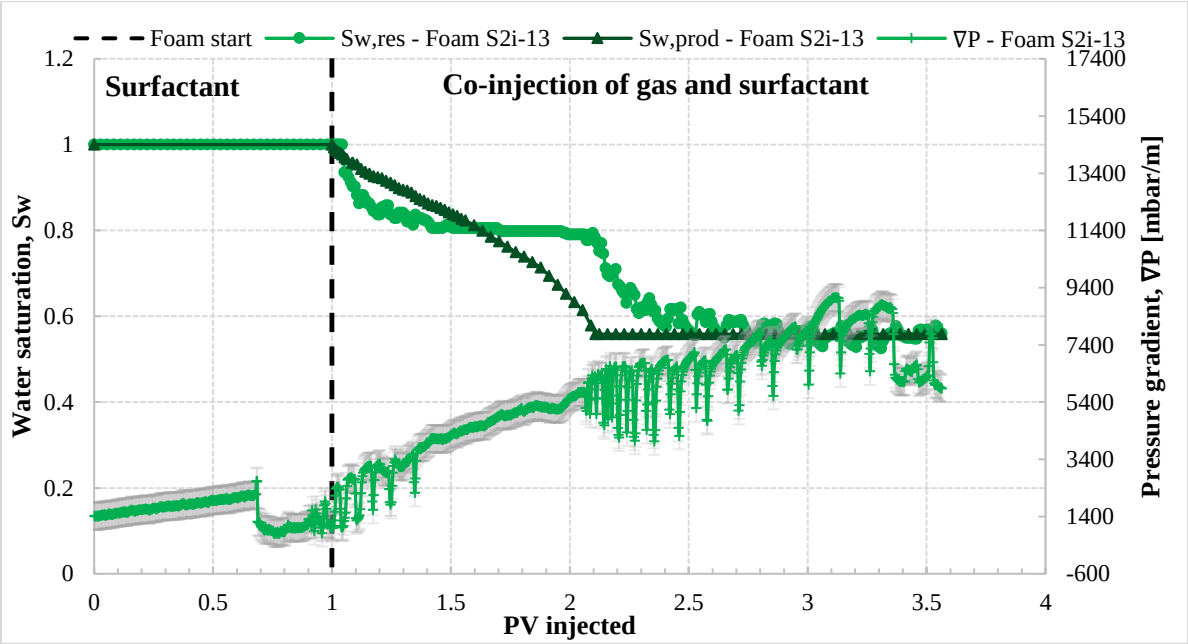

Figure 52 – Water saturation and pressure gradient during co-injection of CO_2 gas and surfactant solution in sandstone core S2i-13. The core was initially 100% saturated with brine, but was flushed with two pore volumes of surfactant solution before foam injection. One pore volume of surfactant solution injection is included in the plot. Two pore volumes were injected during co-injection, with gas fraction 0.7 and injection rate 50 cc/h. Start of co-injection is indicated with the black, dashed vertical line. Water saturations (left axis) were calculated using resistivity and Archie's second law, and water production measurements conducted during the injection, while pressure gradient (right axis) is based on measured differential pressures. Error bars in pressure gradients are calculated based on uncertainties in ESI pressure transducers.

9.3 The Effect of Foam on Mobility Reduction

Parameters of initial and irreducible water saturations, increase in pressure gradient and mobility reduction factors for CO_2 are presented in Table 10. Irreducible water saturations are calculated from the water production originating from the core plugs, which was estimated based on the total production measured during experiments, the volume of surfactant solution injected during the foam injection, the liquid volume initially present in the dead volumes, and the remaining liquid in dead volumes after injection. The mobility reduction factors were calculated using equation (4), and the average increase in pressure gradient from the baseline experiments.

Table 10 – Parameters of initial water saturation, S_{wi}, irreducible water saturation based on material balance, $S_{wirr,f,prod}$, minimum water saturation based on resistance, $S_{wmin,f,res}$, maximum increase in pressure gradient, ∇P_f, and mobility reduction factor, MRF, during co-injection of CO_2 gas and surfactant solution in Bentheimer sandstone cores.

Core ID	S_{wi}	$S_{wirr,f,prod}$	$S_{wmin,f,res}$	Increased ∇P_f (50 cc/h)	MRF
	[%]	[%]	[%]	[mbar/m]	
S2i-7	100	57.49	54.55	2505.16	1.90
S2i-9	100	56.98	53.78	1677.93	1.27
S2i-12	100	53.58	55.85	8363.44	6.33
S2i-13	100	55.83	52.50	8259.16	6.25

Mobility of gas was reduced with an average factor of 3.94. Increase in pressure gradient was most noticeable in core S2i-12 and S2i-13, where the gas mobility was more than 6 times lower than in pure gas injections. This may indicate that the most stable foam displacements took place in these cores (Kam and Rossen, 2003).

Variations in pressure gradient and mobility reduction factor between the core plugs can be a result of variations of foam stability and rock heterogeneity, in addition to uncertainties in the estimations of the time foam entered the core plugs. The CO_2 pump was pressurized to a pressure of approximately 0.6 bar over the system pressure to prevent backflow. Small variations between pump pressure and system pressure can have caused a pressure difference between the CO_2 pump and the system large enough to increase or decrease the gas flow rate in the start of the experiment. If this occurred, it would result in errors in calculation of the time foam entered the core, as the higher gas flow rate would cause an earlier time of foam entrance. The early increase in pressure gradient in core S2i-7, seen in Figure 49, may indicate this. Smaller increase in pressure gradient before foam presumably enters the core plugs can be observed in the other cores as well. A pressure *decrease* before foam enters the core is observed in core S2i-13, which corresponds to the time when injection rate of surfactant solution was changed from 50 cc/h to 15 cc/h.

9.4 Validity of Archie's Law in Foam-Water Systems

Changes in water saturation based on water production evolved differently in the various core samples. In core S2i-7 the water saturation decreased relatively rapidly and reached the assumed endpoint saturation at approximately 1.48 PV injected. A steady decrease was observed in core S2i-9, where the calculated endpoint saturation was reached at 1.74 PV injected. The rate of decrease in water saturation in core S2i-12 slowed down until approximately 1.45 PV injected. A slight increase in pressure was followed by an increase in water production rate, and endpoint

saturation was reached around 1.65 PV injected. Water saturation in core S2i-13 decreased slowly in the beginning of the injection, and did not reach the endpoint value until approximately 2.11 PV injected. Endpoint saturations based on material balance varied from a minimum of 53.58% in core S2i-12 to a maximum of 57.49% in core S2i-7.

Endpoint saturations based on water production differed less than 3.4% from the minimum water saturations calculated with Archie's law. The trends of decrease in water saturations calculated by the two methods were relatively similar for core S2i-7, but varied more for the other cores. The resistivity depends on the connectivity of the water, and may not mirror the total amount of water in the core plugs if the water is not connected. Water saturation based on resistivity fluctuates in a similar manner as the pressure gradient, and it was observed during injections that after some time the inlet pressure began to fluctuate between a pressure below and above the backpressure. This can explain simultaneous change in the water saturation. Studies of Rossen (1988) showed a correlation between gas compressibility and pressure fluctuations, and found that increased flow resistance causing compression of gas, was accompanied by an increase in the differential pressure. Gas compression probably increases the connectivity of the liquid phase in foam, thereby decreasing the resistivity, resulting in higher calculated water saturations.

As seen in Table 11, the maximum deviation in water saturation based on material balance and Archie's law ranged from 16.55% to 35.17%. Endpoint saturations during foam injections deviated between 2.27% and 3.33%. Archie's law is originally developed for oil-water systems, with only one phase conducting electricity, and a modification is needed in systems with two or more conducting phases (Glover et al., 2000). The original form of Archie's second law, which has been used in this thesis, does not consider the conductivity of lamellae in foam. The liquid phase in foam is conducting electricity, but is influenced by bubble size, which varies through the experiments (Datye and Lemlich, 1983).

Archie's law has proven valid in CO_2 gas-water systems in previous investigations (Nakatsuka et al., 2010), but too few pure gas injections have been performed in this thesis to support these findings.

Table 11 - Comparison of water saturation calculated based on material balance and Archie's second law in CO_2 gas/water systems and CO_2 foam/water systems in sandstone cores. Maximum deviation, average deviation and difference in minimum water saturation are listed.

Core ID	Type of experiment	Max. deviation S_w [%]	Avg. deviation S_w [%]	Deviation S_{wirr} [%]
S2i-10	Baseline	17.51	11.18	11.13
S2i-11	Baseline	15.08	6.27	1.03
S2i-7	Foam	16.55	3.94	2.94
S2i-9	Foam	35.17	10.96	3.20
S2i-12	Foam	20.91	10.96	2.27
S2i-13	Foam	33.50	6.99	3.33

10 EXPERIMENTAL UNCERTAINTIES

Experimental uncertainties include systematic errors and random errors that were present during experiments, and possibly influenced the measuring data. Experimental uncertainties observed in this thesis are listed in the following:

- An estimate of uncertainty in water saturations based on material balance gives an uncertainty of 0.01%, based on uncertainty in the imbibition cell, which was 0.05 ml. The uncertainty is likely to be higher, as the water saturations are calculated from injected surfactant volume and surfactant volume in the system dead volumes, and uncertainties in these values should be considered.
- Instrumental uncertainty in the LCR-meter used for resistivity measurements were 0.2-0.3%, which results in an estimated uncertainty of 0.2% in water saturations based on Archie's second law, using equation A8 in Appendix B. Since Archie's law originally is developed for oil-water systems, the real uncertainty in water saturations is much higher.
- Offset between the injection pumps was found before all foam injections, and was noted at atmospheric pressure. The offset varied, but was typically between 0.3-0.4 bar, with a higher pressure in the gas pump than in the surfactant pump. Offset was corrected for by pressurizing the gas pump after the system pressure was stabilized at the backpressure. Pressurization of the pumps may have affected the offset, as in several experiments a deviation from the desired gas fraction of 0.7 was observed. This was probably caused by a lower or higher pressure in the gas pump relative to the system, which affected the gas flow rate.
- Offset in ESI pressure transducers possess large uncertainties. This is discussed in Appendix E.
- During foam injection, it was difficult to determine the production in the inverted imbibition cell after foam breakthrough, as foam was produced. Final readings of total production were done after the foam was broken down, to achieve a measure of only the liquid phase. Production from the core plugs was calculated based on measured production, dead volumes and injected volume of surfactant solution, which all poses uncertainties.
- The system pressure was maintained by a backpressure regulator (BPR) during experiments in non-atmospheric conditions. The BPR had an opening and closing

mechanism that let fluids through when the system pressure was higher than the backpressure, but closed when the system pressure fell below the backpressure. Pressure fluctuations were observed in several experiments, and were probably caused by this mechanism combined with compressibility of gas.

- During increase of system pressure to 2 bar for co-injections in fractured marble cores some core properties might have been altered, as the core pieces and end pieces sled apart. This is explained in section 7.2.2. It was attempted to restore the original state of each core plug, and weight measurements indicated little or no alteration, but porosity or permeability measurements to verify this was not done.
- Interactions between chemicals in fluids and solids may have occurred. NaCl brine was used in all experiments, but may have interacted with rock minerals in the marble cores. This is discussed in more detail in Appendix C.
- Pressure tests were performed before all experiments to detect any leakage in the experimental system. During foam injections in core S2i-12 and S2i-13 a source of leakage was not detected, but there seemed to be an average leakage rate of 0.015 ± 0.010 ml/min, based on pressure decrease in the surfactant pump.
- Variations in temperature may have influenced the fluid properties during experiments. All experiments were performed in ambient conditions, at an assumed temperature of 21°C, but small temperature variations may have occurred. The effect of temperature variations would probably not be significant, but may have affected the resistivity measurements.

Part IV – Conclusions and Future Work

11 CONCLUSIONS

Foam injections in brine saturated fractured marble cores and unfractured Bentheimer sandstone cores of 2" diameter and 10 cm length were investigated. Foam was pre-generated in a foam generator upon entering the core samples, by co-injecting gas and surfactant solution. Pressure gradients and endpoint water saturations obtained in foam injections were compared with pure gas injections. Resistivity was measured during experiments in sandstone cores. The following conclusions are drawn:

- Co-injection of N_2 gas and surfactant solution in fractured marble cores did not improve sweep efficiency as expected. Investigated core samples were small, with pore volume ranging from 8.6-10.9 ml, and gravity effects during pure gas injection appeared to be negligible.
- Foam injection in the fracture system of highest permeability resulted in the highest endpoint water saturation. MRI confirmed better sweep in certain parts of the fracture network during pure gas injection.
- MRI of fractured marble cores was successful in presenting qualitative analyses of water saturations and displacement efficiency after pure gas injections and during a co-injection of gas and surfactant solution.
- Co-injections of CO_2 gas and surfactant solution in unfractured Bentheimer sandstone cores reduced gas mobility relative to pure CO_2 gas injections with an average mobility reduction factor of 3.94, ranging from 1.27-6.33. This resulted in water recovery improvement, by reducing the endpoint water saturations by an average of 18.22%.
- Water saturations based on resistivity measurements were calculated with Archie's second law. An average deviation between water saturations based on Archie's law and water saturations based on material balance during all foam experiments was 7.46%, with a maximum deviation of 35.17%. Archie's law is developed for a system containing only one conducting phase, and a modification is needed for calculations in a foam-water system, where the liquid phase in the foam dispersion conducts electricity.

12 FUTURE WORK

Suggestions for future work based on obtained results in this thesis are:

- Investigations of foam flow in fractured porous media, to compare with foam flow in unfractured porous media and fractured media with initially zero porosity.
- Studies of foam behavior in fractured and unfractured media at reservoir conditions, where the CO_2 exists in a supercritical phase.
- MRI of foam injections in fractured and unfractured core samples with quantitative evaluations of water saturations.
- More resistivity experiments are needed to add statistics for a better understanding of resistivity behavior in foam displacements.
- Investigations of the use of foam for oil displacement in similar core samples as in this thesis, to investigate the potential for EOR.

NOMENCLATURE

A	Cross-sectional area
a	Parameter describing tortuosity and pore size distribution
b	Parameter describing tortuosity
B_o	Static magnetic field
B_1	Dynamic magnetic field
γ	Gyromagnetic ratio
ΔP	Differential pressure
ΔP_f	Differential pressure during foam injection
ΔP_g	Differential pressure during gas injection
D	Diameter
E	Storage efficiency
E_D	Microscopical displacement efficiency
E_R	Recovery factor
E_S	Storage efficiency
E_{vol}	Volumetric displacement efficiency
θ	Wetting angle
F	Formation factor
I	Resistivity index
K	Permeability
K_e	Effective permeability
k_r	Relative permeability
λ	Mobility
λ_{CO2}	Mobility of CO_2
λ_x	Mobility of the displaced fluid
L	Length
l	Length
μ	Viscosity
M	Mobility ratio
m	Cementation exponent
M_o	Total magnetization
ν	Darcy velocity
N	Fluid velocity
n	Saturation exponent
N_{vc}	Capillary number
P	Pressure
P_c	Capillary pressure
P_{nw}	Pressure of nonwetting fluid phase
P_w	Pressure of wetting fluid phase
∇P	Pressure gradient
Q	Flow rate
ρ	Density
R	Resistivity
r	Electrical resistance
r_c	Capillary radius
R_o	Resistivity of a formation 100% saturated with formation water
R_t	True resistivity of a formation
R_w	Resistivity of formation water

σ	Interfacial tension
S_w	Water saturation
S_{wi}	Initial water saturation
S_{wirr}	Irreducible water saturation
T	Temperature
T_1	Spin-lattice relaxation time
T_2	Spin-spin relaxation time
V_b	Bulk volume
V_{CO2}	Volume of CO_2
V_p	Pore volume
V_w	Volume of water
$V_{w,prod}$	Volume of produced water
φ	Porosity
ω_o	Larmor frequency

ABBREVIATIONS

BPR	Backpressure regulator
CCS	Carbon capture and sequestration
EOR	Enhanced oil recovery
IFT	Department of Physics and Technology
MR	Magnetic resonance
MRF	Mobility reduction factor
MRI	Magnetic resonance imaging
NCS	Norwegian Continental Shelf
NMRI	Nuclear magnetic resonance imaging
POM	Polyoxymethylene
PV	Pore volume
UoB	University of Bergen
WAG	Water alternating gas

APPENDIX A – FUNDAMENTAL PROPERTIES IN RESERVOIR ENGINEERING

PERMEABILITY

Permeability is the measure of a rock's ability to transmit fluids. Absolute permeability, K [D], is the permeability if only one fluid phase is present in the rock, while effective permeability, K_e [D], is the permeability to each fluid phase if several fluid phases are present. Permeability is defined through Darcy's law, which for linear, horizontal flow of one incompressible fluid phase at constant flow rate through a core plug is defined as (Skarestad and Skauge, 2013):

$$Q = \frac{KA\Delta P}{\mu L} \tag{A1}$$

where Q [cm^3/s] is the flow rate, A [cm^2] is the cross-sectional area of the core, ΔP [atm] is the differential pressure over the core, μ [cP] is the viscosity of the fluid, and L [cm] is the length of the core plug.

RELATIVE PERMEABILITY

If several phases are present in a rock, each fluid phase has a relative permeability, k_r. Relative permeability is defined as the ratio between the effective permeability for a fluid and the absolute permeability of a rock (Skarestad and Skauge, 2013):

$$k_r = \frac{K_e}{K} \tag{A2}$$

k_r depends on fluid saturations.

WETTABILITY

Wettability is the tendency of one fluid to adhere to a solid surface when several immiscible fluids are present (Ahmed, 2006). One method of defining the wetting characteristics of a fluid for a rock is to measure the contact angle at the liquid-rock surface, through the liquid. A contact angle of 0° would indicate complete wettability, while a contact angle of 180° indicate complete nonwetting preferences of that liquid. The wettability in a porous media influences the fluid distribution in the media. The wetting phase spreads on the rock surface and normally occupy the smaller pores, while the nonwetting phase occupies the larger pores.

INTERFACIAL TENSION

Interfacial tension, or surface tension, refers to the tension at the surface between two immiscible fluids. The tension is caused by intermolecular and intramolecular forces in the fluid phases.

CAPILLARY PRESSURE

Capillary pressure, P_c [Pa], is the pressure difference across the interface between to immiscible fluid phases (Ahmed, 2006). It is caused by the interfacial tension between the fluids, and is expressed as:

$$P_c = P_{nw} - P_w \tag{A3}$$

where P_{nw} [Pa] is the pressure of the nonwetting fluid phase, and P_w [Pa] is the pressure of the wetting fluid phase. In a capillary tube or a pore, the capillary pressure can be expressed through Laplace's equation (Skarestad and Skauge, 2013):

$$P_c = \frac{2\sigma cos\theta}{r_c} \tag{A4}$$

where σ [N/m] is the interfacial tension between the non-wetting phase and the wetting phase, θ is the contact angle describing wettability, and r_c is the capillary or pore radius [m].

CAPILLARY NUMBER

A capillary number, N_{vc}, characterizes the ratio between viscous and capillary forces in a fluid displacement, and can be expressed by the following equation (Skarestad and Skauge, 2013):

$$N_{vc} = \frac{Viscous\ forces}{Capillary\ forces} = \frac{v\mu}{\sigma_{nw/w}} \tag{A5}$$

where v [m/s] is the Darcy velocity, and μ [Pa·s] is the viscosity of the displacing fluid.

APPENDIX B – UNCERTAINTY ESTIMATIONS

There are several uncertainty factors present during experimental work and calculations, and these are important to be aware of. Uncertainties are related to accuracy of equipment, experimental setup and procedures. Factors influencing experimental uncertainties are presented in section 10.

UNCERTAINTY CALCULATIONS

Estimations of uncertainties in this study are based on equations presented in the following.

Standard deviation:

Standard deviation was used to calculate uncertainty in absolute permeability and dead volumes in the experimental systems, where mean values were calculated based on a set of measured values. The uncertainty, $S_{\bar{x}}$, for the calculated mean value, $\bar{x}$, is:

$$S_{\bar{x}} = \sqrt{\frac{\sum_{i=1}^{N}(x_i - \bar{x})^2}{N}} \tag{A6}$$

where $x_{i...N}$ is the measured values, and N represents the total number of measurements.

Addition and subtraction:

For a parameter, *R*, that has been calculated by adding or subtracting several independent values *x*, *y*, *z*, …, *i*, with different uncertainties S_x, S_y, S_z, …, S_i, the uncertainty, S_R, can be calculated by the following formula:

$$S_R = \sqrt{(S_x)^2 + (S_y)^2 + (S_z)^2 + \cdots + (S_i)^2} \tag{A7}$$

Multiplication and division:

For a parameter, *R*, that has been calculated by multiplying or dividing several independent values *x*, *y*, *z*, …, *i*, with different uncertainties S_x, S_y, S_z, …, S_i, the uncertainty, S_R, can be calculated by the following formula:

$$\frac{S_R}{R} = \sqrt{(\frac{S_x}{x})^2 + (\frac{S_y}{y})^2 + (\frac{S_z}{z})^2 + \cdots + (\frac{S_i}{i})^2} \tag{A8}$$

INSTRUMENTAL UNCERTAINTIES

Instrumental uncertainties are related to the precision of the instruments used in experiments. An overview of uncertainties in equipment used in this thesis is presented in Table A1. Uncertainties in instruments have been used to calculate uncertainties in core properties, pressure, dead volumes, production and water saturations.

Table A1 - Instrumental uncertainties of instruments used for the experimental work in this thesis.

Instrument	**Parameter**	**Uncertainty**	**Unit**
Weight	Mass	± 0.01	G
Vernier Caliper	Diameter, length	± 0.005	Cm
Stigma ST-pump	Pressure, rate, volume	± 0.1%	bar, ml/min, ml
ESI Pressure Transducers	Pressure	± 0.1% FS*	Bar
Imbibition cell	Volume	± 0.05	ml
LCR-meter	Electrical resistance	± 0.2-0.3%	Ω
*FS = full scale			

APPENDIX C – THE EFFECT OF NACL BRINE ON MARBLE ROCKS

NaCl brine is normally used in experiments performed on sandstone, and is called sandstone brine, but in this thesis 1 wt% NaCl brine was also used for marble cores. Marble is mainly composed of the calcite mineral, and a $CaCl_2$ brine would be more suitable, but former studies performed by Haugen et al. (2012) have shown that certain surfactant types interact with Calcium ions, which results in surfactant precipitation. However, fellow master student Andreas G. Polden also used NaCl brine in fractured marble cores, and found indications of interaction between the brine and rock minerals. During injection of brine for permeability measurements, it was observed that the pressure gradient continued to increase over a longer time, at constant injection rate. Several pore volumes of brine were injected, and the development in pressure gradient can be seen in Figure A1. The increasing pressure gradient may indicate interactions between the NaCl brine and the marble rock, causing dissolving of the rock. Loose rock particles that form, function as an obstacle to flow, which again increases the pressure gradient. Polden investigated the use of $CaCl_2$ together with the Surfonic® L24-22 surfactant used for experiments in this thesis, and did not observe surfactant precipitation. Further work is needed to confirm this.

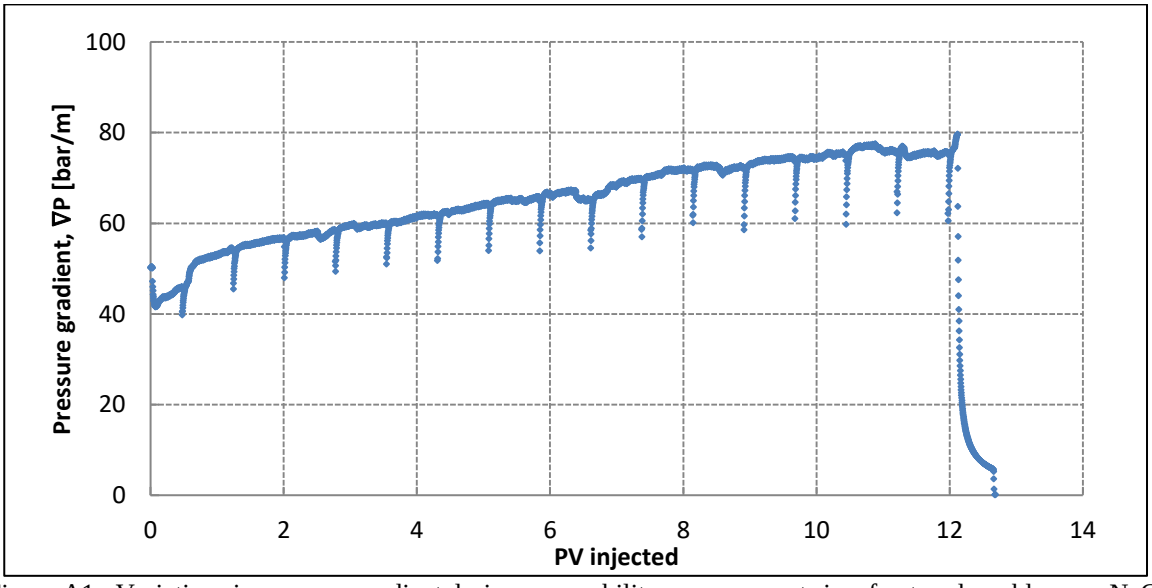

Figure A1 - Variations in pressure gradient during permeability measurements in a fractured marble core. NaCl brine was injected with a constant rate of 60 ml/h. (Polden, A. G. - Fellow master student at Reservoir Physics at the University of Bergen, 2017)

APPENDIX D – ESTIMATION OF DEAD VOLUMES

Dead volumes in end pieces attached to the marble cores:

End pieces connected to the fractured marble cores constituted a significant void volume that was considered when calculating the fracture volume of the core plugs. Each end piece contained three holes available for fluid flow, as seen in Figure A2.

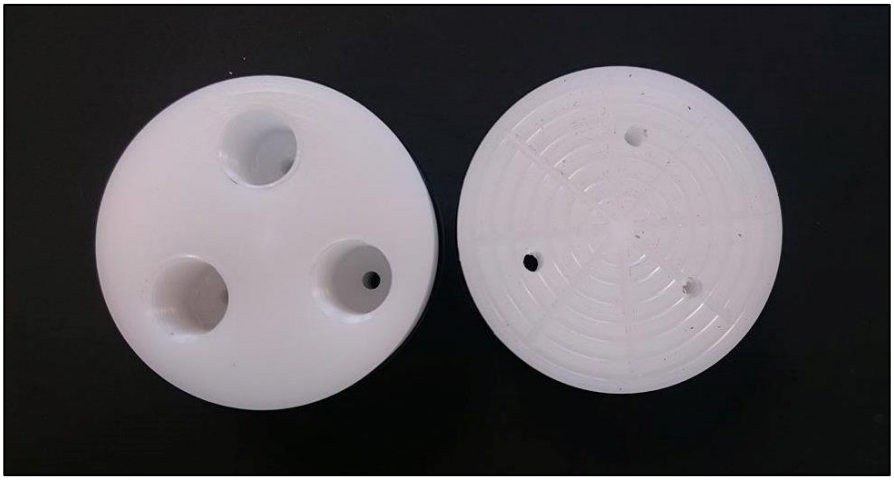

Figure A2 – End pieces attached to fractured marble cores during experiments in this thesis, shown from both sides. The side with the smaller holes was connected to the core plug, while the side with the large holes was attached to Swagelok fittings. All end pieces were similar.

Swagelok fittings, shown in Figure A3, were attached to the holes in the end pieces. The volume of the smallest holes in the Swagelok fittings was neglected, as it would have little or no effect on the total volume when tubing or caps were attached. Both the end pieces and the Swagelok fittings provided available volume for fluids.

Figure A3 – Swagelok fittings were connected to each hole in the end pieces.

Volumes were calculated using lengths and diameters of the holes in the end pieces and the holes in the Swagelok fittings, that were measure with a Vernier caliper. Measurements and

calculations of dead volumes are presented in Table A2. Uncertainties in volumes are calculated with uncertainty equations presented in Appendix B.

Table A2 – Calculated dead volumes in fractured marble cores, constituting void space in end pieces and Swagelok fittings.

Dead volumes for each fractured marble core	Volume [ml]	Uncertainty [ml]
Swagelok fittings	3.000	± 0.062
End pieces	3.302	± 0.026
Total dead volume	6.302	± 0.067

Dead volumes in experimental setups:

Dead volumes in experimental setups constitute the volume available for fluids in inlet and outlet tubing, the foam generator, and in core holder end pieces for sandstone cores. In experiments performed at non-atmospheric pressure, the inlet and outlet tubing, and core holder end pieces were filled with brine or surfactant solution prior to the injections. The volumes were produced during experiments, but were subtracted from the total production to find the production originating from the core plugs. Inlet dead volumes were also used to calculate the time foam entered the core plugs during co-injections.

Measurements of dead volumes in experimental systems were obtained by injecting brine with a Stigma ST pump. Injected volumes were monitored with the computer program for the pump. One student paid attention to the experimental system and the time of breakthrough, while one student monitored the injection with the computer program. No liquid was present in the system before brine injections. Dead volumes were measured several times for the same system, and average values were calculated. Uncertainties are based on standard deviation during four different measurements of the dead volume in the experimental setup used for foam injections in sandstone cores S2i-7 and S2i-9.

During baseline injections in fractured marble cores the system was not filled with brine before injections, and all liquid production originated from the core plugs. Nylon tubing made it possible to observe times of breakthrough in the core plugs and in the outlet tubing. Dead volumes did not affect production, and were not necessary to measure. Before baseline injections in sandstone cores, the system had been pressurized by injecting brine. Hence, the system was filled with brine, and the dead volume included tubing volume from the point where gas entered the system to the inlet end piece, and from the outlet end piece to the end of the outlet tubing. Before foam injections, the systems were filled with surfactant solution, and the

dead volumes included tubing volume between the T-tubing connector between gas and surfactant solution to the inlet of the core including void volume in the foam generator, and from the outlet of the core to the end of the outlet tubing. Dead volumes are listed in Table A3. The experimental system for sandstone cores was altered before foam injection in core S2i-12 and S2i-13, by replacing parts of the tubing.

Table A3 – Dead volumes in experimental systems during baseline experiments and foam experiments.

Parameter	**Foam FM**	**Baseline BS**	**Foam BS[1]**	**Foam BS[2]**
Inlet dead volume ± 0.5 [ml]	2.6	6.9	8.5	11.0
Outlet dead volume ± 0.5 [ml]	3.3	6.2	7.8	6.2

FM = fractured marble
BS = Bentheimer sandstone
[1]Core S2i-7 and S2i-9
[2]Core S2i-12 and S2i-13

APPENDIX E – CALCULATIONS OF OFFSET BETWEEN ESI PRESSURE TRANSDUCERS

ESI pressure transducers were used to measure pressures at core inlet and core outlet during all experiments. Prior to injections, when there was no fluid flow through the core plugs, the ESI pressure transducers should ideally measure the same pressure. Difference between pressure at inlet and outlet at these conditions were considered as offset between the pressure transducers. A correction factor was calculated to account for offset during experiments. Before each injection, the inlet and outlet pressures were measured until stabilized, at the same pressure conditions as the following experiment. The correction factor was calculated as an average of the differential pressures calculated after the pressures had stabilized, before injections. The correction factor was subtracted from the differential pressures calculated during the experiment.

During foam injections in fractured marble cores most of the calculated differential pressures were negative, even after correcting for offset. A negative differential pressure during fluid displacement from core inlet to core outlet is unlikely, and a new correction factor was used to adjust for this. The start point differential pressure was used as the new correction factor. This elevated all the differential pressures to positive values, but maintained the trend during experiments.

Negative differential pressures can indicate errors in correction factor, but it may also be a cause of drift in the ESI pressure transducers due to long usage or calibration in different pressure and temperature conditions. The fractured marble cores had high permeabilities, and the differential pressures were expected to be small. The range of the pressure transducers were 0-6.0 bar at the inlet and 0-2.5 bar at the outlet, and there were relatively large uncertainties in the measured pressures.

APPENDIX F – AN OVERVIEW OF EXPERIMENTS

A complete overview of experiments performed with sandstone cores is presented in Table A4. Most experiments were conducted together with fellow master student Solveig Carlsen. Several experiments were performed to test different pressure conditions.

Table A4 – A complete overview of experiments conducted with Bentheimer sandstone cores.

Core ID	Experiment	Date	T/P conditions	Collaboration partner
S2i-1	CO_2 injection (baseline)	02.12.2016	21 °C / 70 bar	Solveig Carlsen
S2i-1	CO_2 foam injection	18.01.2017	21 °C / 70 bar	Solveig Carlsen
S2i-2	CO_2 injection (baseline)	07.12.2016	21 °C / 70 bar	Solveig Carlsen
S2i-2	CO_2 foam injection	19.01.2017	21 °C / 70 bar	Solveig Carlsen
S2i-3	CO_2 foam injection	31.01.2017	21 °C / 1 bar	Solveig Carlsen
S2i-4	CO_2 foam injection	31.01.2017	21 °C / 1 bar	Solveig Carlsen
S2i-6	CO_2 foam injection	09.03.2017	21 °C / 10 bar	Solveig Carlsen
S2i-7	CO_2 foam injection	13.03.2017	21 °C / 10 bar	Solveig Carlsen
S2i-8	CO_2 foam injection	14.03.2017	21 °C / 10 bar	Solveig Carlsen
S2i-9	CO_2 foam injection	15.03.2017	21 °C / 10 bar	Solveig Carlsen
S2i-10	CO_2 injection (baseline)	23.04.2017	21 °C / 10 bar	Solveig Carlsen (alone)
S2i-11	CO_2 injection (baseline)	24.04.2017	21 °C / 10 bar	Solveig Carlsen
S2i-12	CO_2 foam injection	24.04.2017	21 °C / 10 bar	Solveig Carlsen
S2i-13	CO_2 foam injection	25.04.2017	21 °C / 10 bar	Solveig Carlsen

Table A5 presents a complete overview of experiments performed with fractured marble cores. Most experiments were conducted in collaboration with fellow master student Solveig Carlsen. Several baseline injections were performed where the differential pressure was measured with a Validyne pressure transducer. This did not give reasonable pressure response and new baseline injections were performed using ESI pressure transducers instead.

Table A5 – A complete overview of experiments performed with fractured marble cores.

Core ID	Experiment	Date	T/P conditions	Collaboration partner
OMS_1	N_2 injection (baseline)	08.09.2016	21 °C / 1 bar	Solveig Carlsen
OMS_1	N_2 injection (baseline)	14.09.2016	21 °C / 1 bar	Solveig Carlsen
OMS_1	N_2 injection (baseline)	19.09.2016	21 °C / 1 bar	Solveig Carlsen
M2i-1	N_2 injection (baseline)	24.10.2016	21 °C / 1 bar	Solveig Carlsen
M2i-1	N_2 injection (baseline)	02.11.2016	21 °C / 1 bar	Solveig Carlsen
M2i-1	N_2 injection (baseline)	04.11.2016	21 °C / 1 bar	Solveig Carlsen
M2i-1	N_2 injection (baseline)	05.11.2016	21 °C / 1 bar	Solveig Carlsen
M2i-1	N_2 injection (baseline)	23.11.2016	21 °C / 1 bar	Solveig Carlsen
M2i-1	N_2 injection (baseline)	11.01.2017	21 °C / 1 bar	Solveig Carlsen
M2i-1	N_2 injection (baseline)	20.03.2017	21 °C / 1 bar	Solveig Carlsen
M2i-1	N_2 injection (baseline)	21.03.2017	21 °C / 1 bar	Solveig Carlsen
M2i-1	N_2 injection (baseline)	21.03.2017	21 °C / 1 bar	Solveig Carlsen
M2i-1	N_2 foam injection	22.03.2017	21 °C / 2 bar	Solveig Carlsen
M2i-1	N_2 foam injection	22.03.2017	21 °C / 2 bar	Solveig Carlsen
M2i-1	N_2 foam injection	24.03.2017	21 °C / 2 bar	Solveig Carlsen
M2i-1	N_2 foam injection	27.03.2017	21 °C / 2 bar	
M2i-1	MRI of N_2 foam injection	06.04.2017	21 °C / 2 bar	Solveig Carlsen
M2i-2	N_2 injection (baseline)	12.12.2016	21 °C / 1 bar	Solveig Carlsen
M2i-2	N_2 injection (baseline)	13.12.2016	21 °C / 1 bar	Solveig Carlsen
M2i-2	N_2 injection (baseline)	10.01.2017	21 °C / 1 bar	Solveig Carlsen
M2i-2	N_2 injection (baseline)	20.03.2017	21 °C / 1 bar	Solveig Carlsen
M2i-2	N_2 injection (baseline)	21.03.2017	21 °C / 1 bar	Solveig Carlsen
M2i-2	N_2 injection (baseline)	21.03.2017	21 °C / 1 bar	Solveig Carlsen
M2i-2	N_2 foam injection	24.03.2017	21 °C / 2 bar	Solveig Carlsen
M2i-2	N_2 foam injection	24.03.2017	21 °C / 2 bar	Solveig Carlsen
M2i-2	N_2 foam injection	27.03.2017	21 °C / 2 bar	
M2i-3	N_2 injection (baseline)	12.12.2016	21 °C / 1 bar	Solveig Carlsen
M2i-3	N_2 injection (baseline)	13.12.2016	21 °C / 1 bar	Solveig Carlsen
M2i-3	N_2 injection (baseline)	10.01.2017	21 °C / 1 bar	Solveig Carlsen
M2i-3	N_2 injection (baseline)	21.03.2017	21 °C / 1 bar	Solveig Carlsen
M2i-3	N_2 injection (baseline)	21.03.2017	21 °C / 1 bar	Solveig Carlsen
M2i-3	N_2 foam injection	27.03.2017	21 °C / 2 bar	
M2i-3	N_2 foam injection	27.03.2017	21 °C / 2 bar	

REFERENCES

AHMED, T. 2006. *Reservoir engineering handbook*, Gulf Professional Publishing.

AL-MAQBALI, A., AGADA, S., HAUGEN, A., FERNØ, M. A. & GEIGER, S. 2015. Modelling Foam Displacement in Fractured Carbonate Reservoirs. *Abu Dhabi International Petroleum Exhibition and Conference.* Abu Dhabi, UAE, 9-12 November: Society of Petroleum Engineers.

ALLAN, J. & SUN, S. Q. 2003. Controls on Recovery Factor in Fractured Reservoirs: Lessons Learned from 100 Fractured Fields. *SPE Annual Technical Conference and Exhibition.* Denver, Colorado, USA, 5-8 October: Society of Petroleum Engineers.

ARCHIE, G. E. 1942. The Electrical Resistivity Log as an Aid in Determining Some Reservoir Characteristics. *Transactions of the AIME,* 146**,** 54-62.

BACHU, S. 2015. Review of CO 2 storage efficiency in deep saline aquifers. *International Journal of Greenhouse Gas Control,* 40**,** 188-202.

BACHU, S., GUNTER, W. D. & PERKINS, E. H. 1994. Aquifer disposal of CO2: Hydrodynamic and mineral trapping. *Energy Conversion and Management,* 35**,** 269-279.

BATÔT, G., FLEURY, M. & NABZAR, L. 2016. Study of CO2 foam performance in a CCS context. *The 30th International Symposium of the Society of Core Analysts.* Snowmass, Colorado, USA, 21-26 August.

BENSON, S. M. & COLE, D. R. 2008. CO₂ Sequestration in Deep Sedimentary Formations. *Elements,* 4**,** 325-331.

BENTHAM, M. & KIRBY, M. 2005. CO2 storage in saline aquifers. *Oil & gas science and technology,* 60**,** 559-567.

BERKOWITZ, B. 2002. Characterizing flow and transport in fractured geological media: A review. *Advances in Water Resources,* 25**,** 861-884.

BLAKER, T., CELIUS, H., LIE, T., MARTINSEN, H., RASMUSSEN, L. & VASSENDEN, F. 1999. Foam for gas mobility control in the Snorre field: the FAWAG project. *SPE Annual Technical Conference and Exhibition.* Houston, Texas, USA, 3-6 October: Society of Petroleum Engineers.

BUCHGRABER, M., CASTANIER, L. M. & KOVSCEK, A. R. 2012. Microvisual Investigation of Foam Flow in Ideal Fractures: Role of Fracture Aperture and Surface Roughness. *SPE Annual Technical Conference and Exhibition.* San Antonio, Texas, USA, 8-10 October: Society of Petroleum Engineers.

DAMEN, K., FAAIJ, A. & TURKENBURG, W. 2006. Health, safety and environmental risks of underground CO 2 storage–overview of mechanisms and current knowledge. *Climatic Change,* 74**,** 289-318.

DATYE, A. K. & LEMLICH, R. 1983. Liquid distribution and electrical conductivity in foam. *International Journal of Multiphase Flow,* 9**,** 627-636.

EIKEN, O., RINGROSE, P., HERMANRUD, C., NAZARIAN, B., TORP, T. A. & HØIER, L. 2011. Lessons learned from 14 years of CCS operations: Sleipner, In Salah and Snøhvit. *Energy Procedia,* 4**,** 5541-5548.

ELMAOĞLU, M. & ÇELIK, A. 2011. *MRI Handbook: MR Physics, Patient Positioning, and Protocols*, Springer Science and Business Media.

ENICK, R. M., OLSEN, D. K., AMMER, J. R. & SCHULLER, W. 2012. Mobility and Conformance Control for CO2 EOR via Thickeners, Foams, and Gels -- A Literature Review of 40 Years of Research and Pilot Tests. *SPE Improved Oil Recovery Symposium.* Tulsa, Oklahoma, USA, 14-18 April: Society of Petroleum Engineers.

ESPINOZA, D. A., CALDELAS, F. M., JOHNSTON, K. P., BRYANT, S. L. & HUH, C. 2010. Nanoparticle-Stabilized Supercritical CO2 Foams for Potential Mobility Control Applications. *SPE Improved Oil Recovery Symposium.* Tulsa, Oklahoma, USA, 24-28 April: Society of Petroleum Engineers.

FERNØ, M. A. 2015. Does foam work in fractured systems? *Complex Fluids in Porous Media.* Bordeaux, France, 12-14 October.

FERNØ, M. A., EIDE, Ø., STEINSBØ, M., LANGLO, S. A. W., CHRISTOPHERSEN, A., SKIBENES, A., YDSTEBØ, T. & GRAUE, A. 2015. Mobility control during CO2 EOR in fractured carbonates using foam:

Laboratory evaluation and numerical simulations. *Journal of Petroleum Science and Engineering,* 135**,** 442-451.

FERNØ, M. A., GAUTEPLASS, J., PANCHAROEN, M., HAUGEN, A., GRAUE, A., KOVSCEK, A. R. & HIRASAKI, G. 2016. Experimental Study of Foam Generation, Sweep Efficiency, and Flow in a Fracture Network. *SPE Journal,* 21**,** 1140-1150.

FIGUEROA, J. D., FOUT, T., PLASYNSKI, S., MCILVRIED, H. & SRIVASTAVA, R. D. 2008. Advances in CO2 capture technology—The U.S. Department of Energy's Carbon Sequestration Program. *International Journal of Greenhouse Gas Control,* 2**,** 9-20.

GLOBAL CCS INSTITUTE 2016. The Global Status of CCS: 2016. Summary Report. Australia: Global CCS Institute.

GLOVER, P. W. J., HOLE, M. J. & POUS, J. 2000. A modified Archie's law for two conducting phases. *Earth and Planetary Science Letters,* 180**,** 369-383.

HAN, W. S., LEE, S.-Y., LU, C. & MCPHERSON, B. J. 2010. Effects of permeability on CO2 trapping mechanisms and buoyancy-driven CO2 migration in saline formations. *Water Resources Research,* 46**,** n/a-n/a.

HAUGEN, Å., FERNØ, M. A., GRAUE, A. & BERTIN, H. J. 2012. Experimental study of foam flow in fractured oil-wet limestone for enhanced oil recovery. *SPE Reservoir Evaluation & Engineering,* 15**,** 218-228.

HAUGEN, Å., MANI, N., SVENNINGSEN, S., BRATTEKÅS, B., GRAUE, A., ERSLAND, G. & FERNØ, M. A. 2014. Miscible and Immiscible Foam Injection for Mobility Control and EOR in Fractured Oil-Wet Carbonate Rocks. *Transport in Porous Media,* 104**,** 109-131.

HUAMAN, R. N. E. & JUN, T. X. 2014. Energy related CO2 emissions and the progress on CCS projects: A review. *Renewable and Sustainable Energy Reviews,* 31**,** 368-385.

HÅGENVIK, C. 2013. *CO2 Injection in Hydrate Bearing Sandstone with Excess Water.* Master's thesis, The University of Bergen.

IDING, M. & RINGROSE, P. 2010. Evaluating the impact of fractures on the performance of the In Salah CO2 storage site. *International Journal of Greenhouse Gas Control,* 4**,** 242-248.

IPCC 2005. Special Report on Carbon Dioxide Capture and Storage. Cambridge University Press, New York, NY (United States); Intergovernmental Panel on Climate Change, Geneva (Switzerland). Working Group III.

IPCC 2014. Climate Change 2014: Synthesis Report. Contribution of Working Groups I, II and III to the Fifth Assessment Report of the Intergovernmental Panel on Climate Change [Core Writing Team, R.K. Pachauri and L.A. Meyer (eds.)]. IPCC, Geneva, Switzerland, 151 pp.

JOHANSEN, S. A. 2016. *An Experimental Study of Foam Flow in Fractured Systems of Increasing Size.* Master's thesis, University of Bergen.

KAM, S. I. & ROSSEN, W. R. 2003. A Model for Foam Generation in Homogeneous Media. *SPE Journal,* 8**,** 417-425.

KHESHGI, H., CAPPELEN, F., LEE, A., CROOKSHANK, S., HEILBRUNN, A., MIKUS, T., ROBSON, W., SENIOR, W. J., STILEMAN, T. J. & WARREN, L. 2006. Carbon Dioxide Capture and Geological Storage: Contributing to Climate Change Solutions. *SPE International Health, Safety & Environment Conference.* Abu Dhabi, UAE, 25-29 September: Society of Petroleum Engineers.

KOVSCEK, A., PATZEK, T. & RADKE, C. Simulation of foam transport in porous media. SPE Annual Technical Conference and Exhibition, 1993 Houston, Texas, USA, 3-6 October. Society of Petroleum Engineers.

KOVSCEK, A. R. & RADKE, C. J. 1993. Fundamentals of foam transport in porous media. *Advances in Chemistry.* USA: ACS Publications.

KOVSCEK, A. R., TRETHEWAY, D. C., PERSOFF, P. & RADKE, C. J. 1995. Foam flow through a transparent rough-walled rock fracture. *Journal of Petroleum Science and Engineering,* 13**,** 75-86.

LAWSON, J. B. & REISBERG, J. 1980. Alternate slugs of gas and dilute surfactant for mobility control during chemical flooding. *SPE/DOE Enhanced Oil Recovery Symposium.* Tulsa, Oklahoma, USA, 20-23 April: Society of Petroleum Engineers.

LEE, H. O., HELLER, J. P. & HOEFER, A. M. W. 1991. Change in Apparent Viscosity of CO2 Foam With Rock Permeability. *SPE Reservoir Engineering,* 6**,** 421-428.

LI, R. F., YAN, W., LIU, S., HIRASAKI, G. & MILLER, C. A. 2010. Foam Mobility Control for Surfactant Enhanced Oil Recovery. *SPE Journal,* 15**,** 934-948.

LIEN, J. R. 2004. *PTEK 211 Grunnleggende Reservoarfysikk (Kjerneanalyse og logging),* Bergen, Norway, Department of Physics and Technology, University of Bergen.

LINDEBERG, E., VUILLAUME, J.-F. & GHADERI, A. 2009. Determination of the CO2 storage capacity of the Utsira formation. *Energy Procedia,* 1**,** 2777-2784.

MAZZOLDI, A., PICARD, D., SRIRAM, P. & OLDENBURG, C. 2013. Erratum to 'Simulation-based estimates of safety distances for pipeline transportation of carbon dioxide'. *Greenhouse Gases: Science and Technology,* 3**,** 309-310.

NA, H. B., SONG, I. C. & HYEON, T. 2009. Inorganic nanoparticles for MRI contrast agents. *Advanced materials,* 21**,** 2133-2148.

NAKATSUKA, Y., XUE, Z., GARCIA, H. & MATSUOKA, T. 2010. Experimental study on CO 2 monitoring and quantification of stored CO 2 in saline formations using resistivity measurements. *International Journal of Greenhouse Gas Control,* 4**,** 209-216.

NELSON, R. A. 2001. *Geological Analysis of Naturally Fractured Reservoirs,* USA, Gulf Professional Publishing.

NGUYEN, Q. P., ALEXANDROV, A. V., ZITHA, P. L. & CURRIE, P. K. 2000. Experimental and Modeling Studies on Foam in Porous Media: A Review. *SPE International Symposium on Formation Damage Control.* Lafayette, Louisiana, USA, 23-24 February: Society of Petroleum Engineers.

OLDENBURG, C. M. 2007. Migration mechanisms and potential impacts of CO2 leakage and seepage. *Carbon Capture and Sequestration Integrating Technology, Monitoring, and Regulation***,** 127-146.

OLDENBURG, C. M., PRUESS, K. & BENSON, S. M. 2001. Process Modeling of CO2 Injection into Natural Gas Reservoirs for Carbon Sequestration and Enhanced Gas Recovery. *Energy & Fuels,* 15**,** 293-298.

RANSOHOFF, T. C. & RADKE, C. J. 1988. Mechanisms of Foam Generation in Glass-Bead Packs. *SPE Reservoir Engineering,* 3**,** 573-585.

RINGROSE, P. S., MATHIESON, A. S., WRIGHT, I. W., SELAMA, F., HANSEN, O., BISSELL, R., SAOULA, N. & MIDGLEY, J. 2013. The In Salah CO2 Storage Project: Lessons Learned and Knowledge Transfer. *Energy Procedia,* 37**,** 6226-6236.

ROSSEN, W. R. 1988. Theories of Foam Mobilization Pressure Gradient. *SPE Enhanced Oil Recovery Symposium.* Tulsa, Oklahoma, USA, 16-21 April: Society of Petroleum Engineers.

SCHRAMM, L. L. 2006. *Emulsions, Foams, and Suspensions: Fundamentals and Applications*, Wiley.

SEEVAM, P. N., DOWNIE, M. J. & RACE, J. M. 2007. Transport of CO2 for Carbon Capture and Storage in the UK. *Offshore Europe.* Aberdeen, Scotland, UK, 4-7 September: Society of Petroleum Engineers.

SHENG, J. J. 2013. Chapter 11 - Foams and Their Applications in Enhancing Oil Recovery. *Enhanced Oil Recovery Field Case Studies.* Boston, Massachusetts, USA: Gulf Professional Publishing.

SKARESTAD, M. & SKAUGE, A. 2013. *PTEK213 Reservoarteknikk II,* Bergen, Norway, University of Bergen.

SKAUGE, A., AARRA, M., SURGUCHEV, L., MARTINSEN, H. & RASMUSSEN, L. 2002. Foam-assisted WAG: experience from the Snorre Field. *SPE/DOE Improved Oil Recovery Symposium.* Tulsa, Oklahoma, USA, 13-17 April: Society of Petroleum Engineers.

TORP, T. A. & GALE, J. 2004. Demonstrating storage of CO2 in geological reservoirs: The Sleipner and SACS projects. *Energy,* 29**,** 1361-1369.

UK CCS RESEARCH CENTRE. 2012. *What is CCS: CO2 storage* [Online]. UK. Available: http://www.ukccsc.co.uk/what-is-ccs/storage.html [Accessed 19th of May 2017].

VAN GOLF-RACHT, T. D. 1982. *Fundamentals of Fractured Reservoir Engineering,* The Netherlands, Elsevier Science.

VASSHUS, S. S. 2016. *Experimental Study of Foam Generation and Flow in Carbonate Fracture Systems.* Master's thesis, University of Bergen.

WALSTRA, P. 1989. Principles of foam formation and stability. *In:* WILSON, A. J. (ed.) *Foams: Physics, chemistry and structure.* London, UK: Springer.

WASSMUTH, F., GREEN, K. & RANDALL, L. 2001. Details of in-situ foam propagation exposed with magnetic resonance imaging. *SPE Reservoir Evaluation & Engineering,* 4**,** 135-145.

YANG, H., XU, Z., FAN, M., GUPTA, R., SLIMANE, R. B., BLAND, A. E. & WRIGHT, I. 2008. Progress in carbon dioxide separation and capture: A review. *Journal of Environmental Sciences,* 20**,** 14-27.

ZHANG, D. & SONG, J. 2014. Mechanisms for Geological Carbon Sequestration. *Procedia IUTAM,* 10**,** 319-327.